https://www.sciencedirect.com/science/article/abs/pii/S0094114X14002614

https://doi.org/10.1016/j.mechmachtheory.2014.10.012

A Novel Hardware-in-the-Loop Device for Floating Offshore Wind Turbines and Sailing Boats

Hermes Giberti[a,*], Davide Ferrari[a]

[a]*Politecnico di Milano, Dipartimento di Meccanica, Campus Bovisa Sud, Via La Masa 1, 20156, Milano, Italy.*

Abstract

In recent years, the development of CFD simulations has increased the knowledge in fluid-structure interaction problems. This trend has been particularly important for Floating Offshore Wind Turbines (FOWTs) and sailing boats. However, especially for these sectors, in which two different fluids are involved, the reliability of CFD prediction tools requires further experimental validations. To this end, as a complementary approach with respect to ocean wave basins, there is the need for wind tunnel aero-elastic dynamic tests.

This paper presents the customization of a 6-Degrees-of-Freedom (DoF) motion-simulator device for Hardware-in-the-Loop (HIL) wind tunnel tests on floating scale models. Each step of the machine design-loop is motivated and described: the kinetostatic synthesis is obtained through a multi-objective optimization using a genetic algorithm, the inverse dynamic properties are mapped on the workspace, and finally the drive system is mechanically sized using the so called α-β theory. The emphasis is placed on the mechatronic design methodology, so that different mechanisms and requirements may be considered.

Keywords: Mechatronic design-loop, Kinetostatic synthesis, Multi-objective optimization, Genetic algorithms, PKMs, Hexaglide, HexaFloat.

1. INTRODUCTION

For the experimental simulation of the dynamic working conditions of hydro-aero-elastic structures, a new testing capability was developed at the Politecnico di Milano wind tunnel (CIRIVE) for its 14m×4m low-speed test section, represented in Fig. 1, where the airflow reproduces civil-environmental conditions. To this end, a 6-DoF robotic device with parallel kinematics, called HexaFloat, was proposed as successor to the older 2-DoF system, presented by Bayati *et al.* in [1]. In particular, there is the need to emulate the sea water under scale models of Floating Offshore Wind Turbines (FOWTs) and sailing boats, during hardware-in-the-loop (HIL) dynamic tests. To do this, the force and moment components, exchanged between the models and the positioning device, will be measured through a 6-axis balance. Then, with this measure, the hydrodynamic problem is solved in real-time to provide the reference motion for the actuators.

The application context for FOWTs and the sector motivations are presented by Bayati *et al.* in [2]. In this field, there is the need to deeply investigate the control issues in connection

*Corresponding author. tel.:+39-02-2399-8452; fax:+39-02-2399-8492
Email addresses: hermes.giberti@polimi.it (Hermes Giberti)

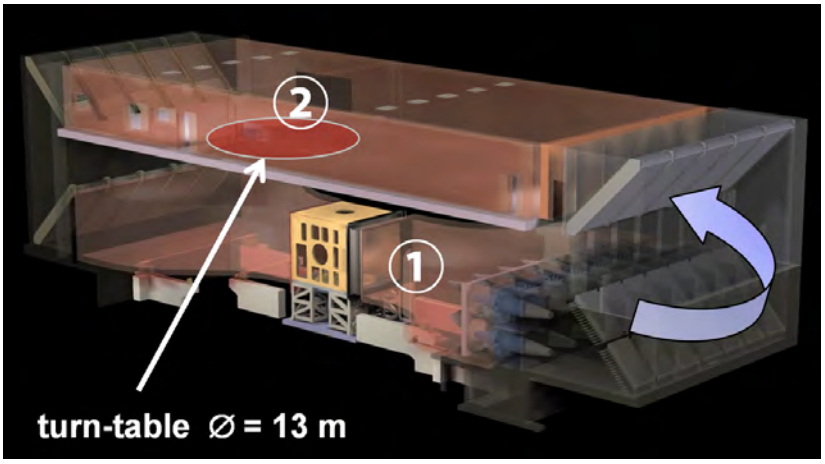

Fig. 1: Politecnico di Milano low-speed wind tunnel (CIRIVE): (1) aeronautical test section, speed = 55 m/s - dimensions = 4m×4m; (2) civil-environmental test section, speed = 14 m/s - dimensions = 14m×4m.

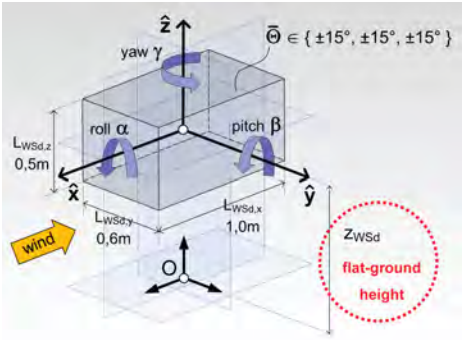

Fig. 2: Desired workspace (WSd).

Max. zero-peak amplitudes and max. frequencies

	Wind turbine	Sail-boat	Bridge
f max [Hz]	0.7	1.5	3.0
A_x [m] - // wind	0.50	-	0.01
A_y [m] - ⊥ wind	0.30	-	0.01
A_z [m] - vertical	0.25	-	0.01
A_α [deg] - roll	15°	5°	3°
A_β [deg] - pitch	15°	10°	3°
A_γ [deg] - yaw	15°	10°	3°

Tab. 1: Desired sinusoidal movements.

with different mooring systems, to get significant improvements in the efficiency of the energy production. Only in this way, the bigger costs necessary to install and manage floating deep-water wind farms in the large-offshore can be justified with respect to not-floating and near-to-the-coast plants: shorter payback times are fundamentals. Solving this issues in the next years will transform the promising sector of FOWTs in one important reality of the energy production world.

The design process of a machine starts always from a given set of requirements and iteratively returns to them until the matching between the desired performances and the actual ones is considered satisfactory. When this process is conducted with a mechatronic approach it means that mechanics and electronics issues are considered at same time in a multidisciplinary and integrated way, as described by Giberti *et al.* in [3] using as a test case the mechatronic design of a 2-DoF-5R PKM.

The preliminary specifications for the HexaFloat are showed in Tab. 1: the robot is required

to position its tool center point (TCP) and to orient its end-effector within the six-dimensional desired workspace (WSd) showed in Fig. 2. Also maximum motion frequencies are given. In addition, it is necessary to stay low with the TCP in the vertical direction because it is not possible to place the robot outside of the wind tunnel test section, which has a limited height of 4 m: the more the workspace is low, the more the usable height of the test section is wide, allowing a convenient geometric scaling of the aerodynamic models. The usable zone extends from the so-called flat-ground, under which all the instrumentation and also the robot will be hidden, to an height close to the ceiling, but far enough away from it, to not encounter the ceiling boundary layer. Finally, it is worth noting that HIL dynamic tests on FOWTs and sailing boats represents a new field of research, without a consolidated literature. This means that the previously described requirements may significantly change, especially after a first experimental phase. Therefore the design process and the machine itself had to be flexible and reconfigurable, to possibly achieve a different desired workspace.

All this requirements led us toward the field of parallel kinematic machines (PKMs), because of their potential advantageous features. PKMs often occupy a complementary position with respect to serial robots, in the sense of higher loading capabilities, achievable velocities and accelerations, positioning accuracy and components modularity. However, these kind of robots have been always devoted to specific tasks, such as flight and driving motion simulators, micro positioners and pointing systems, without a widespread diffusion, especially in the industrial sector. This is due to a more complicated and less well-established design phase in connection with some critical aspects, which can be summarized as follow: the workspace is little with respect to the overall size of the machine; big end-effector linear displacements are often in contrast with big end-effector rotations (e.g. linear delta vs. parallel wrists); the usable workspace is limited by singular poses and interference problems, especially the link-to-link risk of collision; the anisotropic behaviour determines low overall dexterity; the passive joints are key elements in determining the boundary of the workspace because of their limited mobility ranges. All these disadvantageous features makes PKMs poorly flexible to task modifications, so that they are rarely available on the market as standard ready-to-use solutions and require a deep customization phase (e.g. PKMs as machine tools [4]). Therefore, there is the need for design methodologies that can overcome long times, uncertain results and high development costs.

This paper presents the steps of the HexaFloat design-loop, whose flow diagram representation is showed in Fig. 3. The 6-PUS architecture is chosen and deeply investigated. Doing this, we traced a possible way to make effective the PKMs' advantages, while overcoming their disadvantages, with the aim to best meet the given requirements. The next Sections are organized as follow. Section 2 deals with the Hexaglide kinematic architecture: the motivations of its choice, the solution of the inverse kinematic problem, the workspace computation, and the geometric parametrization. Section 3 presents the kinematic and kinetostatic synthesis: a multi-objective optimization approach is adopted to determine the value of the geometric dimensions, two cost functions are defined with a novel strategy [5], making use of thresholds, and their optimality is sought in the sense of Pareto, using a genetic algorithm provided by Matlab. Then, the cones of mobility of the joints are centered on the actual poses. Section 4 presents the inverse dynamic analysis: the condition of heavier usage of the robot are defined in terms of masses and task-space movements, the forces to realize the given motion laws are obtained with a Simulink model. Finally, in Section 5 these forces allow to compare different Pareto-optimal solutions and to mechanically size the drive system [6].

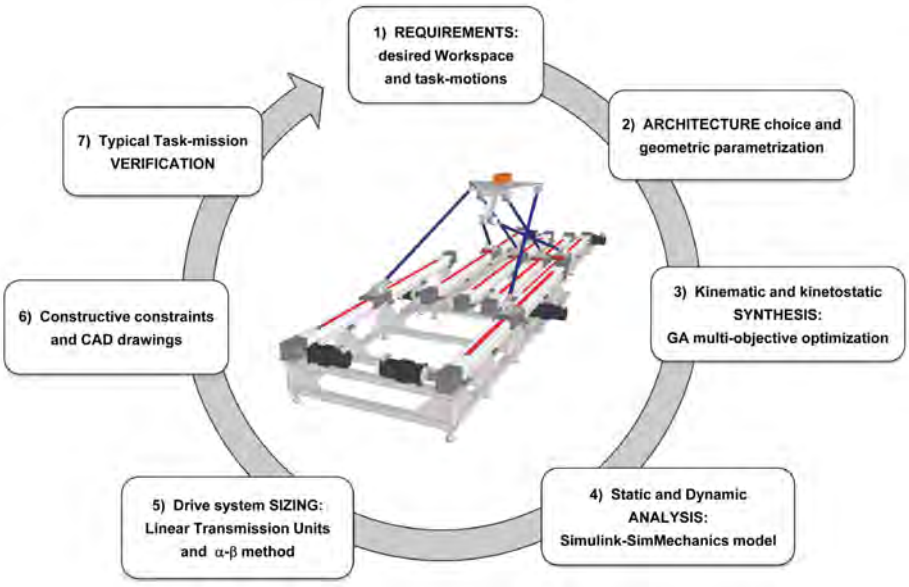

Fig. 3: Steps of the machine design-loop.

2. ARCHITECTURE

Because of their non-linear transmission of movements and forces from joint- to task-space, the performances achieved by parallel machines are difficult to standardize, so that, pretending to do universal design choices that uniquely relates the given requirements to a specific kinematic topology is currently hazardous. In fact, the same kinematic topology could provide very good or very bad performances, depending on its geometric dimensions. Therefore, a definitive comparison between different architectures, without a deeply investigation of each of them, it is at least difficult if not impossible. This is clearly highlighted by Merlet in [7, chap. 11] or by Weck and Staimer in [4], where they stated that a parallel machine with a poor topology but optimally designed with respect to its geometric dimensions may perform better than a parallel machine with appropriate topology but poorly designed. They report the example of a classical Gough-Stewart platform: changing the radius of the platform by 10% may modify the worst-case stiffness by 700%.

Among the PKMs that can provide 6-DoF, the focus has been placed on the Hexaglide, which is also reported as 6-PUS kinematic architecture with parallel linear guideways. Its linkages consist of six closed-loop kinematic chains which connect the fixed base to the mobile platform with the same sequence of joints: actuated Prism (P), Universal (U) and Spherical (S). The links have fixed length, while the actuation takes place through the linear guideways, which are not necessarily coplanar but lie on parallel planes.

This kinematic solution was developed in the mid '90s at ETH of Zürich to built a high-speed milling machine tool [8, 9, 10]. Later, other researchers studied the Hexaglide: Bonev in [11, 12] presents a geometric method to compute the workspace (vertex-space). Finally, an important application of the Hexaglide architecture is the Model Positioning Mechanism (MPM), which has been used since 2005 to simulate air-planes manoeuvres in the NWB wind tunnel located in

Braunshweig (Germany) [13, 14].

2.1. Topology choice motivations

Looking at the requirements, the Hexaglide kinematic topology has been chosen because:

1. its workspace center can be very close to its fixed base. This is not true for other hexapod robots such as the well-known Gough-Stewart platform, whose TCP is not able to occupy positions so much close to the base with a workspace of the same extension. Furthermore, also the parking position can be very low in the vertical direction, so that the robot can be completely hidden under the flat-ground when not used;
2. its workspace has a predominant direction. This direction is the same of the guideways and can coincide with the direction of the wind, which is the most demanding one in terms of the required TCP motion amplitudes;
3. its actuation is completely left to the ground. This allows a favourable ratio between the mobile mass of the robot and the payload mass, so that high velocities and accelerations can be achieved. Furthermore, interference problems between the links are reduced because of the minimum size of their cross-sections, contrary to the Gough-Stewart platform, in which the links are the actuators.

2.2. Inverse kinematics

Solving the inverse kinematics means to determine the relation between a given pose of the robot in the task-space and the actuated variables in the joint-space. In our case, by one hand we have the set of the TCP position $\mathbf{p}_{\text{TCP}} = \{x, y, z\}_{\text{TCP}}$ and platform orientation $\mathbf{\Theta} = \{\alpha, \beta, \gamma\}$, on the other hand, we have the displacements q_i of the sliders along their rails, which are collected in $\mathbf{q} = \{q_1, ...q_6\}$. This relation can be obtained writing one vector loop equation for each of the six independent kinematic chains. Using the reference frames and the quantities shown in Fig. 4, without involving the passive joint variables, the inverse kinematic solution can be expressed as:

$$q_i = d_{i,x} + h_i \sqrt{l_i^2 - d_{i,y}^2 - d_{i,z}^2} \tag{1}$$

where $\mathbf{d}_i = \mathbf{p}_{\text{TCP}} + [R(\mathbf{\Theta})]\mathbf{b}'_i - \mathbf{s}_i$, and $h_i = +1$ or $h_i = -1$, depending on the assembly. $[R(\mathbf{\Theta})]$ is the rotation matrix that leads from the mobile reference frame TCP-x′y′z′ to the fixed one O-xyz. After fixing the assembly vector $\mathbf{h} = \{h_1, ...h_6\}$ and the robot dimensions l_i, $\mathbf{s}_i$, and $\mathbf{b}'_i$, the solution of the inverse kinematics is unique. Therefore, a given pose $\mathbf{X} = \{\mathbf{p}_{\text{TCP}}; \mathbf{\Theta}\}$ is related to only one specific set of displacements $\mathbf{q}$. It is noticed that the mobile platform orientation $\mathbf{\Theta}$ is defined using the nautical angles of roll α, pitch β, and yaw γ, in the XYZ Euler sequence, to allow the best transposition of the given requirements.

2.3. Velocity analysis and kinetostatics

The velocities are mapped from task-space into the joint-space using the Inverse Jacobian matrix as follows: $\dot{\mathbf{q}} = [J]^{-1}\mathbf{W}$, where $\mathbf{W} = \{\dot{\mathbf{p}}_{\text{TCP}}; \boldsymbol{\omega}\}$ collects the linear and angular velocities of the mobile platform. The analytical expression of $[J]^{-1}$ is easily obtained by the time derivative of the kinematic vector loop equations and can be written as:

$$[J]^{-1} = [J_q]^{-1}[J_{GS}]^{-1} = \text{diag}(1/n_{i,x}) \begin{bmatrix} \hat{\mathbf{n}}_i^T & (\mathbf{b}_i \times \hat{\mathbf{n}}_i)^T \end{bmatrix} \tag{2}$$

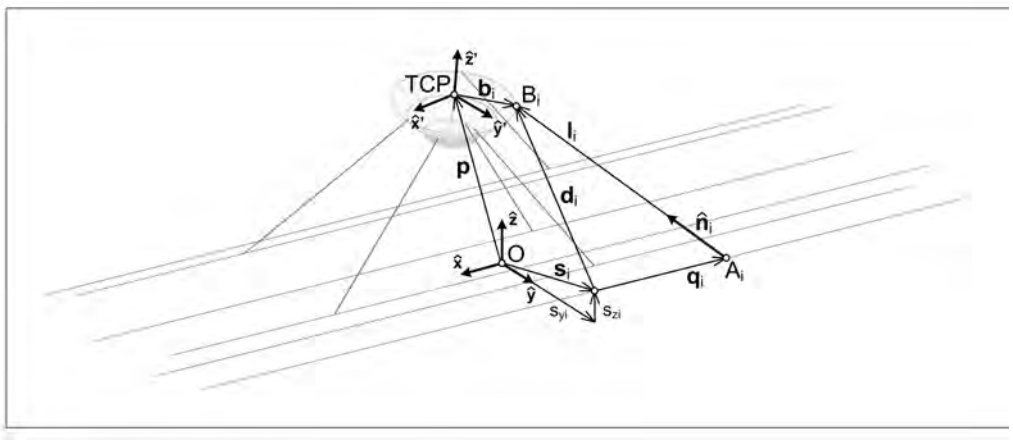

Fig. 4: Diagram of the i-th closed-loop kinematic chain.

in which $\hat{\mathbf{n}}_i = \{n_{i,x}, n_{i,y}, n_{i,z}\}$ is the unit vector which represents the direction of the i-th link and two contributions can be recognized: $[J_q]^{-1}$, which collects the cosine of the angles formed by each link with its respective rail, and $[J_{GS}]^{-1}$, which has the same expression of the Gough-Stewart platform Inverse Jacobian.

Then, to solve the kinetostatic problem, the (Direct) Jacobian matrix $[J]$ is computed by numerical inversion of $[J]^{-1}$. The force and moment components exerted on the mobile platform are mapped into the thrust actuation forces on the rails as follows: $\boldsymbol{\tau}_{rails} = [J]^T \mathbf{f}_{\text{TCP}}$. Also in this case, two contributions can be recognized:

$$\boldsymbol{\tau}_{rails} = [J_q]^T [J_{GS}]^T \mathbf{f}_{\text{TCP}} = [J_q]^T \boldsymbol{\tau}_{links} = \text{diag}(n_{i,x}) \boldsymbol{\tau}_{links} \tag{3}$$

Therefore, $[J_{GS}]^T$ and $[J_q]^T$ assume the meaning of generalized transmission ratios, leading from the TCP to the links, and then, from the links to the rails. As shown in Fig. 5, every link is connected to the rest of the robot with a spherical and a universal joint. The link direction passes through the centers U_i and S_i of the joints. The spherical joint can't transmit moments but only a force and this force, instant by instant, can be decomposed into three orthogonal components with respect to the reference frame of the universal joint U_i-$\text{x}_{U_i}\text{y}_{U_i}\text{z}_{U_i}$. The u-joint can't transmit moments along the axes of its cross, so that the following equations can be written:

$$\begin{cases} M_{x,U_i} = F_{z,U_i} \Delta y_{U_i} - F_{y,U_i} \Delta z_{U_i} = 0 \\ M_{y,U_i} = F_{x,U_i} \Delta z_{U_i} - F_{z,U_i} \Delta x_{U_i} = 0 \end{cases} \tag{4}$$

which lead to the following relation between the force components:

$$\frac{F_{x,U_i}}{\Delta x_{U_i}} = \frac{F_{y,U_i}}{\Delta y_U} = \frac{F_{z,U_i}}{\Delta z_{U_i}} \tag{5}$$

stating that the static forces supported by the links are always axially directed. Consequently, no torque is transmitted by the u-joints: $M_{z,U_i} = 0$. This is really true if the weight of the links can be neglected, as in the case of the Hexaglide. Moreover, the forces along the links are always

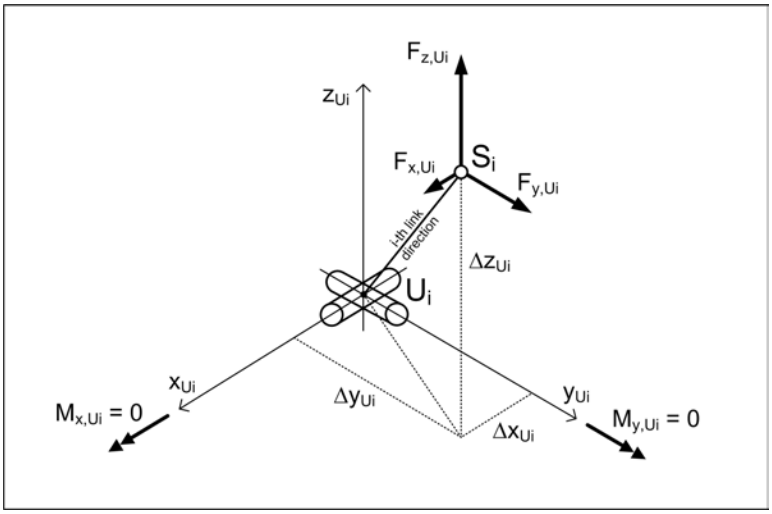

Fig. 5: Universal-Spherical i-th joined link.

larger than the forces along the rails. In fact, they are related by the direction cosine $n_{i,x}$, that is always smaller than the unit.

2.4. Workspace

The workspace of interest is the total orientation workspace (total oWS), which is defined as the set of all the possible locations of the TCP which can be reached with any platform orientation within a given range $R_{\boldsymbol{\Theta}} = [\boldsymbol{\Theta}_{\min}, \boldsymbol{\Theta}_{\max}]$. To evaluate the total oWS, $R_{\boldsymbol{\Theta}}$ is discretized in a grid of N orientations $\alpha\beta\gamma$-grid and the boundary of a constant orientation workspace (constant oWS) is determined for each node of the grid. Finally, the N workspaces are intersected by each other.

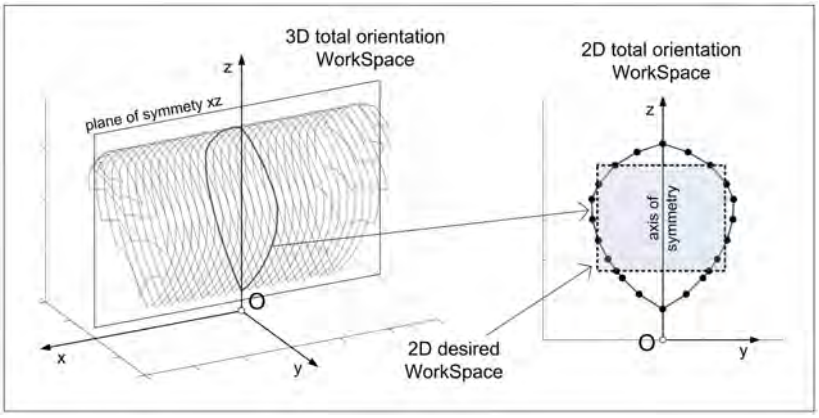

Fig. 6: Symmetry of the total orientation workspace (total oWS): 3D vs. 2D.

Because of the rails arrangement on parallel planes, the x-motion of the TCP is decoupled from the others, resulting in six equal displacements q_i. Considering this and the uniqueness of

the inverse kinematic solution, it follows that the external boundary of the workspace and all the kinetostatic and dynamic properties can be evaluated over a single yz-plane, as shown in Fig. 6. By this way, the 3D workspace is simply obtained translating its two-dimensional evaluation along the rails direction, until one of the sliders reaches the respective rail limit.

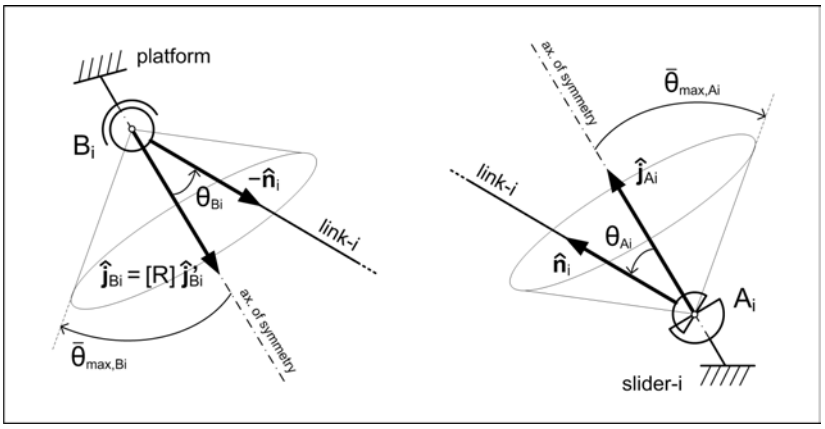

Fig. 7: Conical mobility ranges of the joints.

To determine the boundary of each constant oWS, the yz-plane is probed with a discretization approach, exploring the (y, z) points through a polar coordinate system and checking the following constraints for each i-th kinematic chain:

- $\Delta_i = l_i^2 - d_{i,y}^2 - d_{i,z}^2 > 0$. If Δ_i is negative the length of the i-th link is not enough to reach the required point. When $\Delta_i = 0$ the link is perpendicular to its rail, determining a first-type singularity as defined in [7]: there are directions along which the mobile platform looses its mobility and the robot can ideally support near-to-infinity forces, thanks to the reactions given by the guideways;

- $\theta_{A_i} \leq \bar{\theta}_{tilt,A_i}$ and $\theta_{B_i} \leq \bar{\theta}_{tilt,B_i}$. The angle θ_{S_i} between the actual direction of the link $\hat{\mathbf{n}}_i$ and the joint axis $\hat{\mathbf{j}}_{S_i}$ must be less than the joint tilt angle $\bar{\theta}_{tilt,S_i}$. All the mobility ranges of the joints are modelled as cones. They are fixed to the sliders or to the platform, as shown in Fig. 7. The vertexes of the cones, their axes of symmetry and half-apertures are respectively the joint centers, their axes of symmetry and their tilt angles. This is not really true for the universal joints, but the pyramidal shape of their mobility ranges can be well-approximated with the inscribed cone;

- $\bar{q}_{i,\min} \leq q_i \leq \bar{q}_{i,\max}$. The sliders displacements have to respect the rails limits. However, this constraint is not considered in the synthesis phase since one of the objectives is to obtain the minimum longitudinal size of the robot, so that the rail limits are not known a priori.

2.5. Parametrization

To parametrize a machine means to choose a set of independent parameters whose values identify uniquely its geometry. In this phase, structural geometric constraints can be formerly considered, as for example dimensions equalities. Furthermore, to identify the same geometry,

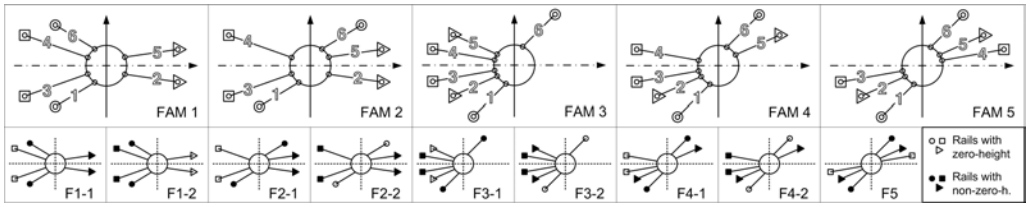

Fig. 8: Architectures classified by symmetry and height of rails (top view).

different sets of parameters could be chosen, but some choices are more appropriate than others to assimilate the given requirements.

In our case, the aim of the parametrization is to ensure a symmetrical total oWS with respect to the longitudinal-vertical xz-plane, in the 3D case, or simply to the z-axis, with the 2D simplification. To do this, the machine must have a symmetric structure. In particular, when the TCP belongs to the centerline plane ($y_{\text{TCP}} = 0$) and the platform has null orientation, the links and their respective joints have to obey in pairs to one of the two following constraints: (type 1) symmetry with respect to the xz-plane, or (type 2) central symmetry with respect to z-axis. As shown in the first row of Fig. 8 and summarized in Tab. 2, the parametrization leads to five distinct families associated with a different assembly vector $\mathbf{h}$. Since the joints are modelled with conical ranges

Family	Symmetry type 1	Symmetry type 2	Assembly vector
	xz-plane	z-axis	$\mathbf{h} = \{h_1, h_2, h_3, h_4, h_5, h_6\}$
Fam. 1	3 pairs L/J	-	$\{-1, +1, -1, -1, +1, -1\}$
Fam. 2	2 pairs L/J (opposite sides)	1 pair L/J	$\{-1, +1, -1, -1, +1, +1\}$
Fam. 3	2 pairs L/J (same side)	1 pair L/J	$\{-1, -1, -1, -1, -1, +1\}$
Fam. 4	1 pairs L/J	2 pairs L/J	$\{-1, -1, -1, -1, +1, +1\}$
Fam. 5	-	3 pairs L/J	$\{-1, -1, -1, +1, +1, +1\}$

L = link, J = joints

Tab. 2: Architectural families determined by type of symmetry.

of fixed apertures, they are completely determined by their centers and axes of symmetry. Two types of parametrization are used to describe their position S_i and their orientation $\hat{\mathbf{j}}_{S_i}$. They differ in the existence or not of the so-called joints home pose (JHP), which is defined as the pose of the robot in which the axes directions of all the joints coincide with the directions of the links. Considering the platform in null orientation and the TCP in $(x, y, z) = (0, 0, z_{\text{JHP}})$, the JHP is completely determined by its height z_{JHP}, which is not forced to coincide with the height z_{WSd} of the desired workspace center. z_{WSd} is itself an additional parameter whose range is limited around the desired height of the flat-ground. Together with z_{JHP} and z_{WSd}, the parameters shown in Fig. 9 constitute the set of 19 parameters to be synthesized in the case of families with the JHP. Without the JHP, for each pair of symmetrical joints it is necessary to describe the direction of one of their axes with two angular parameters, so that, since the pairs of joints are six, the total number of parameters is given by: $19 - 1(z_{\text{JHP}}) + 2 \times 6 = 30$. To limit the computation time, these families are not used in the synthesis phase, but to integrate the joint centering and the constructive modifications into the kinematic model.

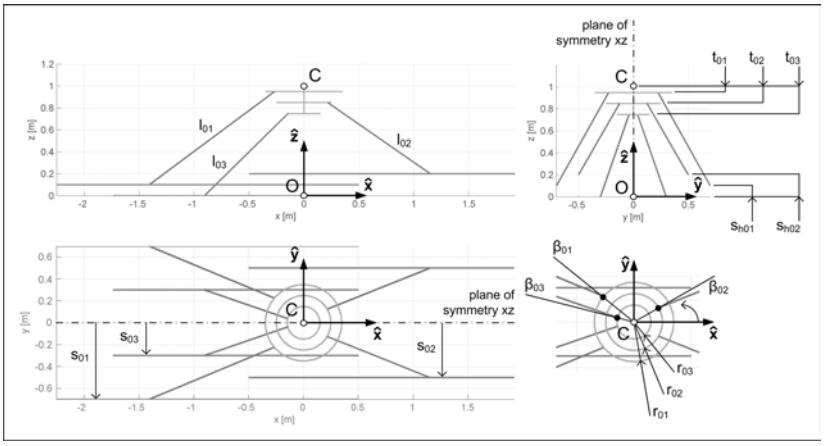

Fig. 9: Geometric parameters common to both parametrization types, with or without JHP.

Finally, it is worth nothing that the non-coplanarity arrangement of the rails helps to decrease the longitudinal size of the robot. This option costs two parameters, namely the heights of two pairs of rails, while the height of the third pair of rails is set to zero. Keeping the parameters independency, it is considered more convenient to optimize z_{WSd}, but this choice has determined an additional division of the five families previously introduced, bringing them to a total of nine, different from each other not only for their symmetry type, but also for the pair of rails with zero height. They are shown in the second row of Fig. 8.

3. SYNTHESIS

Performing the synthesis of a machine means determining its dimensions (geometric parameters) to achieve the best matching with the requirements. Very often, in particular for a robot, the task is not predetermined and defining a fixed operating cycle is not possible. Therefore, only objectives of kinematic and kinetostatic nature can be considered because of their independence from inertias and motions. As described by Merlet in [7], there are different approaches to the synthesis problem. In particular, he supports the use of interval analysis to check imperative constrain relations with a true-false approach on increasingly smaller subsets in which the space of the parameters is progressively divided, obtaining in this way the certified satisfaction of all the requirements. This method was coined appropriate design [15, 16]. However, interval algebra properties and operations are not easy to manage and very often it's not possible to decide a priori the performance levels which must be imperatively satisfied. For these reasons we preferred to use a multi-objective optimal design approach, in which the closeness to an ideal optimum machine, capable to realize perfectly all the requirements, is measured using appropriate cost functions. This method has been already used in other cases, but with different performance indexes and optimization strategies. For example, in [17] Koteswara Rao *et al.* present the multi-objective optimal dimensional design of a 6-PUS machine with not parallel rails, generally called Hexaslide. They consider two objectives, averaged on the workspace: the workspace volume index and the global dexterity index. As motivated in the followings, we preferred to use objectives not averaged on the workspace and aggregated together, using appropriate thresholds, to limit their number.

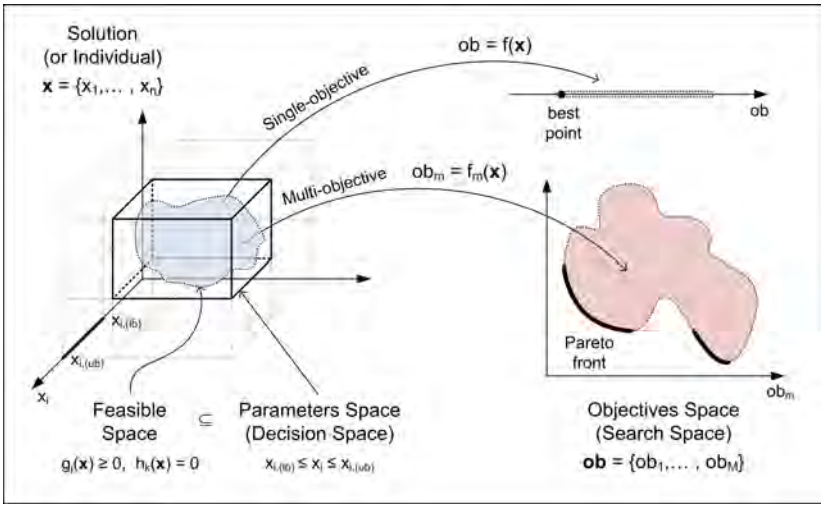

Fig. 10: Cost functions: from the decision- to the objectives-space.

The multi-objective optimization problems can be written in the following general form:

$$\left.\begin{array}{lll} \text{Min. or max.} & f_m(\mathbf{x}), & m = 1, 2, ..., M; \\ \text{subjected to} & g_j(\mathbf{x}) \geq 0, & j = 1, 2, ..., J; \\ & h_k(\mathbf{x}) = 0, & k = 1, 2, ..., K; \\ & x_{i,(lb)} \leq x_i \leq x_{i,(ub)}, & i = 1, 2, ..., n. \end{array}\right\} \tag{6}$$

where f_m is one of the M cost functions which map the parameters space (or decision space) into the objectives space (or search space) as shown in Fig. 10, $\mathbf{x} = \{x_1, ...x_n\}$ is the generic solution point which collects the n parameters to be optimized, g_j and h_k are the constrain relations given on the parameters, $x_{i,(lb)}$ and $x_{i,(ub)}$ are the lower and the upper bounds of variability for the i-th parameter x_i. The satisfaction of all the constraints determines the boundary of the feasible decision space within the parameters space.

With the optimum of all the objectives in the versus of the minimum values, it is said that the solution $\mathbf{x}^{(1)}$ dominates $\mathbf{x}^{(2)}$ if:

1. $f_m(\mathbf{x}^{(1)}) \leq f_m(\mathbf{x}^{(2)}) \ \forall m = 1, 2, ..., M$;
2. $\exists\, \bar{m}$ such that $f_{\bar{m}}(\mathbf{x}^{(1)}) < f_{\bar{m}}(\mathbf{x}^{(2)})$;

which means that the solution $\mathbf{x}^{(1)}$ is no worse than $\mathbf{x}^{(2)}$ in all the objectives and is strictly better than $\mathbf{x}^{(2)}$ in at least one objective. If $\mathbf{x}^{(1)}$ doesn't dominate $\mathbf{x}^{(2)}$ and $\mathbf{x}^{(2)}$ doesn't dominate $\mathbf{x}^{(1)}$, they are mutually non-dominant. In multi-objective optimization problems there isn't only one optimal solution but a set of optimal points $\mathbf{x}^{(i)}$ which are mutually non-dominant and whose optimality with respect to the M objectives is in the sense of Pareto. These optimal points form the so-called Pareto front (or optimal Pareto set), which lie in the left-bottom corner of the objective space, if the optimality of all the objectives has to be searched in the versus of their minimum values. For a given finite set of feasible solutions, $\mathbf{x}^{(i)}$ belongs to the local Pareto front if it is not dominated by any other solution. When the set of solutions coincide with the entire feasible search space, we can find the global Pareto front.

3.1. Objectives definitions

The objectives taken into account in the synthesis phase are: (1) the coverage of the desired workspace, (2) the kinetostatic multiplication of the forces from the TCP to links, (3) the longitudinal size determined by the operating stroke of the sliders, (4) the link-to-link interference, and (5) the link-to-rail interference.

Coverage of the desired workspace

Because the optimality is searched in the direction of the minimum values, what is actually considered in the cost function is the not-covered area A_{nc}, which is the area of the WSd not-covered by the actual constant oWS. The covered area outside the WSd is not taken into account. This evaluation is performed on the generic yz-plane without any constrain on the extension of the rails, being itself an objective of the optimization.

After fixing the orientation $\mathbf{\Theta}$, the edge of the constant oWS is determined. Then, A_{nc} is computed with the following boolean operation:

$$A_{nc}(\mathbf{\Theta}) = \mathrm{WSd} - [\mathrm{WSd} \cap \mathrm{oWS}(\mathbf{\Theta})] \tag{7}$$

which can be implemented in Matlab using *polybool.m* and *polyarea.m*. $A_{nc}(\mathbf{\Theta})$ is determined for each orientation of the $\alpha\beta\gamma$-grid.

Static forces multiplication

To evaluate the kinetostatic properties we consider a grid of equally spaced points yz-grid. After fixing the orientation $\mathbf{\Theta}$, the points P_{in} of the yz-grid which lie within the region WSd $\cap$ oWS($\mathbf{\Theta}$) are identified. This boolean operation can be performed in Matlab with *inpolygon.m*.

For each of these points P_{in}, the maximum multiplication of the static forces is computed by applying on the TCP all the possible combinations of unit forces and torques, in all directions, and evaluating the forces along the links, to limit not only the actuation forces, but also the reactions supported by the rails. We don't consider relative weights between the different force and torque components, because no information is available about typical loading modalities that may justify such a choice.

For a specific pose of the robot $\mathbf{X} = \{P_{in}; \bar{\Theta}\}$, the maximum forces multiplication for all the links corresponds to the infinity norm of the Transpose Jacobian matrix $[J_{GS}]^T$ evaluated in that pose, that is the generalized transmission ratio between the TCP and the links:

$$\tau_{\max}(P_{in}, \mathbf{\Theta}) = \left\| [J_{GS}]^T_{P_{in}, \mathbf{\Theta}} \right\|_\infty \tag{8}$$

whose maximal value, among all the explored poses, must be lower than an acceptable threshold:

$$\tau_{\mathrm{MAX}} = \max_{P_{in}, \mathbf{\Theta}} (\tau_{\max}) \leq \bar{\tau}_{\mathrm{MAX}} \tag{9}$$

The condition in Eq. 9 has led to a new definition of non-covered working area:

$$A'_{nc}(\mathbf{\Theta}) = A_{nc}(\mathbf{\Theta}) + \sum_{P_{in}} \Delta A \cdot k_{force} \tag{10}$$

$$\begin{cases} k_{force} = 0, & \text{if} \quad \tau_{\max}(P_{in}, \mathbf{\Theta}) \leq \bar{\tau}_{\mathrm{MAX}} \\ k_{force} = 1, & \text{otherwise} \end{cases} \tag{11}$$

where ΔA is the area which pertains to the point P_{in}. Computing the force multiplication in this way corresponds to use a constant characteristic length L_c equal to 1 m. The meaning of L_c and one of its possible definitions are discussed by Legnani *et al.* in [18, 19, 20]. The characteristic length can be used to normalize the Jacobian matrix. In fact, when linear degrees of freedom are mixed together with rotational degrees of freedom, the Jacobian matrix terms are not homogeneous with respect to their units of measurement. We have discarded the idea to build an average index of static forces because a good average could hide unwanted peaks associated with near-to-singularity poses.

Finally, it is worth noting that kinetostatic indices, used for PKMs' synthesis, commonly map the joint space into the task space. However, we considered more effective to do the kinetostatic mapping in the opposite direction, because we want to limit the actuation and reaction forces on the guideways. This also allows to consider in the synthesis phase the distance of the actual poses from the so-called second type singular configurations, as defined by Merlet in [7]. In these poses the mobile platform gains lability and the robot can't support loads along some particular directions even with near-to-infinity actuation forces. It is important to consider this aspect for the Hexaglide, because its capacity to stay low with the TCP is paid in terms of bigger actuation forces. Contrary to the case of second type singularities, the location of the first type singular configurations is known a priori. They are the poses in which the mobile platform loses its mobility in some directions and they are located on the border of the workspace, when at least one of the links becomes perpendicular to its rail. However, very often it is firstly achieved the limitation on the tilt angle of the joints.

Links and rails interference

We have interference between the links, that are assumed to be rectilinear, when at least two of them are too close. Attention must be paid to the links crossover because it could even happen moving the platform between two poses without interference problems when observed individually. To decrease the risks of collision, the link-to-link and the link-to-rail axial distances must always be above fixed thresholds: $\bar{d}$ and $\bar{r}$.

To take account of interference, the definition of the not-covered working area is further integrated:

$$A''_{nc}(\boldsymbol{\Theta}) = A_{nc}(\boldsymbol{\Theta}) + \sum_{P_{in}} \Delta A \cdot k \tag{12}$$

$$\begin{cases} k = 0, & \text{if} \quad k_{force} = 0 \ \text{ and } \ k_{crash} = 0 \\ k = 1, & \text{otherwise} \end{cases} \tag{13}$$

$$\begin{cases} k_{crash} = 0, & \text{if} \quad d_{ij} \geq \bar{d} \ \text{ and } \ r_{ij} \geq \bar{r} \quad \forall\, i, j \ \text{ with } \ i \neq j \\ k_{crash} = 1, & \text{otherwise} \end{cases} \tag{14}$$

so that, to be considered as belonging to the working area, the point of the yz-grid must be achieved, not only with a static forces multiplication below $\bar{\tau}_{\text{MAX}}$, but also with a configuration that allow a minimum link-to-link and minimum link-to-rail axial distances respectively bigger than $\bar{d}$ and $\bar{r}$, both determined a priori as acceptable.

In order to not complicate the construction phase and to not modify the axial loading mode, the links shape is kept rectilinear. Therefore, the distance between a couple of links is calculated as the minimum distance between two segments in the space, for a sufficiently dense yz-grid to not lose crossings.

Longitudinal size

The longitudinal size of the robot is defined as the sum of the maximum positive and maximum negative sliders excursions necessary to reach every pose of the total oWS. It is calculated on the generic *yz*-plane as:

$$\text{size}_x = \max_{(P_{in},\boldsymbol{\Theta}),i}(q_i) - \min_{(P_{in},\boldsymbol{\Theta}),i}(q_i) \tag{15}$$

It is noticed that size_x is independent from the x-dimension of the WSd: because of the parallelism of the rails, the total longitudinal size is simply obtained by adding $L_{x,\text{WSd}}$.

3.2. Optimization method

To find the machine that best meets the requirements, a multi-objective optimization is carried out for each architectural family, in their version with the JHP. The multi-objective optimality is in the sense of Pareto, and therefore it is conceptually different from a (single-objective) minimization. In fact, each point on the so-called Pareto front gives a different trade-off between the objectives, allowing the designers to choose the best compromise solution using also other criteria (i.e. dynamical performances, constructive constraints) not-already considered in the synthesis phase, to not make it too complex.

Two cost functions are used:

- objective 1: not-covered area (extended definition)

$$\text{ob1} = \sqrt{\sum_{\boldsymbol{\Theta}} A''_{nc}(\boldsymbol{\Theta})^2} \tag{16}$$

- objective 2: longitudinal size

$$\text{ob2} = \text{size}_x \tag{17}$$

In the first one, three objectives are aggregated: (1) the working area not covered because of kinematic constrains; (2) the respect of the threshold for the maximum force multiplication; (3) the respect of the minimum link-to-link and link-to-rail distances. This aggregation approach using thresholds, it is necessary to limit the computation time.

The cost functions map the space of the 19 parameters to be optimized, also called the decision space, into the space of the objectives, which is a two dimensional space. The boundary of the decision space is fixed by setting the lower bound (lb) and the upper bound (ub) for each parameter. Within the objectives space, at each step, the local Pareto front is identified with respect to the concept of dominance between feasible solutions. The global Pareto front can be determined using the genetic algorithm implemented in the Matlab function *gamultiobj.m*. In general, the genetic algorithms are adequate for the solution of multi-objective optimal problems because their approach is based on a population of individuals [21]. Moreover, another advantage of the genetic algorithms is the possibility to solve non-smooth problems, when the cost functions, as in our case, don't have derivability properties, and so gradient-based methods are not suitable.

The genetic algorithms are based on a selection process that mimics biological evolution. In general, they work by running the following steps:

1. creation of a population with a fixed number of individuals which covers the entire decision space in a statistically significant way. Each individual represents an evaluation of the set of parameters to be optimized and the assigned values are the so-called genes of the individual;

2. cost functions evaluation to give a score to each individual. If the individual is not feasible, with respect to constraint relations, its score is assigned by a penalty function, that is the maximum fitness function evaluation among the feasible individuals of the population, plus a term that measure the constraint violations. This provides the necessary ranking among individuals for the production of the new generation;
3. computation of the average spread of the individuals over the local Pareto front. The algorithm stops at this point if the weighted average of this index computed on the so-called N_s stall generations is less than the tolerance;
4. selection of a fixed number of best individuals (*elite*) which pass unchanged to the next generation;
5. selection of the parents individuals and production of the children individuals according to two modality, in addition to the elitist one: (1) *crossover*, the child is produced by random combination of the genes of two parents individuals, whose values remain unchanged; (2) *mutation*, the child is produced by random mutation of the genes of a single parent individual. The algorithm resumes with a new iteration from step 2.

As described in the third step, the stopping criterion is based on a tolerance threshold and takes into account N_s stall generations prior to the current one, whose number is chosen by the user. Also different stopping criteria can be considered, such as the achievement of a maximum number of generations or a maximum time limit. The algorithm stops as soon as one of these conditions is met.

A key feature of genetic algorithms is the preservation of so-called *diversity* between parameters in the production of children. It represents the average distance among individuals of a population, both in the decision- and objective spaces. The maintenance of diversity among individuals, from generation to generation, is essential because allows the algorithm to search for the optimum in the wider region as possible.

Another general feature of genetic algorithms is to quickly reach a near-to-optimum solution but to converge very slowly. Naturally, to gain an advantage from the use of genetic algorithm, its computation time have to be much less than the time necessary to try systematically all the possible combinations of (densely discretized) parameters values.

3.3. Joints centering

After the optimization, it is evaluated the gain to overcome the JHP with a centering procedure of the joints mobility ranges on the poses achieved by the robot moving its mobile platform in the WSd. To do this, we used the families with 30 parameters.

As shown in Fig. 11, if the mobility range is not uniformly saturated, the joint centering leads to a decrease in the tilt angle necessary to explore all the desired poses. Before we have $\bar{\theta}_{\max,S_i}$, which is saturated in the optimization phase as the maximum tilt angle given by the joint, then we obtain $\bar{\theta}_{c,S_i} < \bar{\theta}_{\max,S_i}$. After the joint centering, if the gain in the tilt angle is significant, we have three options: (1) achieve the same WSd using joints with lower mobility ranges, more easily available on the market; (2) increase the extension of the total oWS with the same joints as before; (3) consider a bigger margin before the collision between the joint parts.

The centering algorithm determines the unit vectors $\hat{\mathbf{j}}_{c,S_i}$ which substitute that ones given by the joint home pose definition $\hat{\mathbf{j}}_{S_i}$. This algorithm is based on [22], where Barequet and Elbert solve the problem to find the cone of minimum aperture which includes a set of given 3D unit vectors. Firstly, exploring all the desired poses, it is determined the set of points achieved by $\hat{\mathbf{n}}_i$ on the sphere of unit radius which has its center in the i-th joint center. Their coordinates

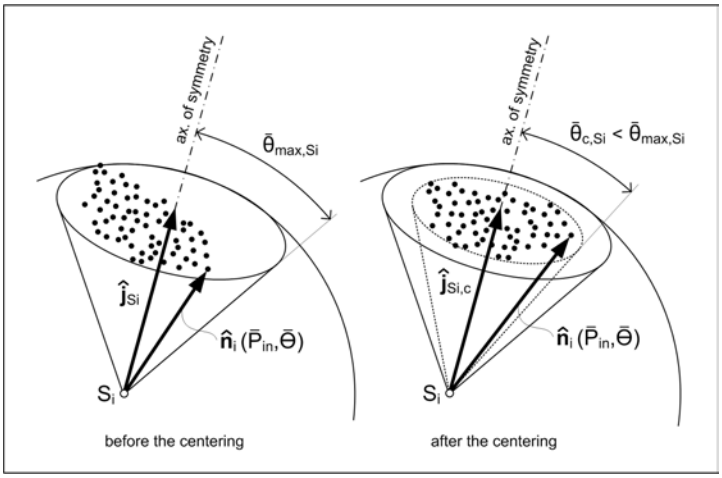

Fig. 11: Before and after the joints centering.

are read in the fixed reference frame with respect to the base, for the A_i centered joints, or with respect to the mobile platform, for B_i centered joints. The algorithm computes the spherical cap of minimum radius which include all the points. The axis of symmetry of this cap is $\hat{\mathbf{j}}_{c,S_i}$.

4. INVERSE DYNAMICS

The dynamic performances of the machine must be taken into account to prove the effectiveness of the synthesis phase, which is based only on kinetostatics, but also to compare Pareto-optimal solutions from different families and to mechanically size the drive system, which is the final aim of this work. In particular, it is of interest to solve the inverse dynamics of the robot, which means to compute the forces and torques required to produce a desired motion of the mobile platform. To this end, a multi-body model with rigid bodies is built in Simulink, using the blocks of the SimMechanics library. Unlike the kinetostatic case, the dynamic behaviour of the robot depends not only on the machine geometry, but also on its inertial properties and on the platform movements. Thus, with the aim to size the drive system, payloads and movements, which could well represent the most severe operating conditions of the robot for the wind tunnel applications, are established. Mathematical formulations of the Hexaglide dynamic problem can be found in [7, 23, 24].

4.1. Simulink model

The Simulink model is shown in Fig. 12. It is easy to recognize the base of the robot, which is weld-joined to the ground of the model, the six limbs, which connect the base to mobile platform, and the payload, which is fixed over the platform. The model is parametric, so that it's possible to easily simulate different Pareto-optimal geometric solutions coming from the optimization phase. The following steps are performed: (1) generation of the platform displacements and rotations, (2) conversion of the platform movements into the six sliders displacements through a function block, which solves the inverse kinematics of the robot, (3) imposition of the prismatic joints

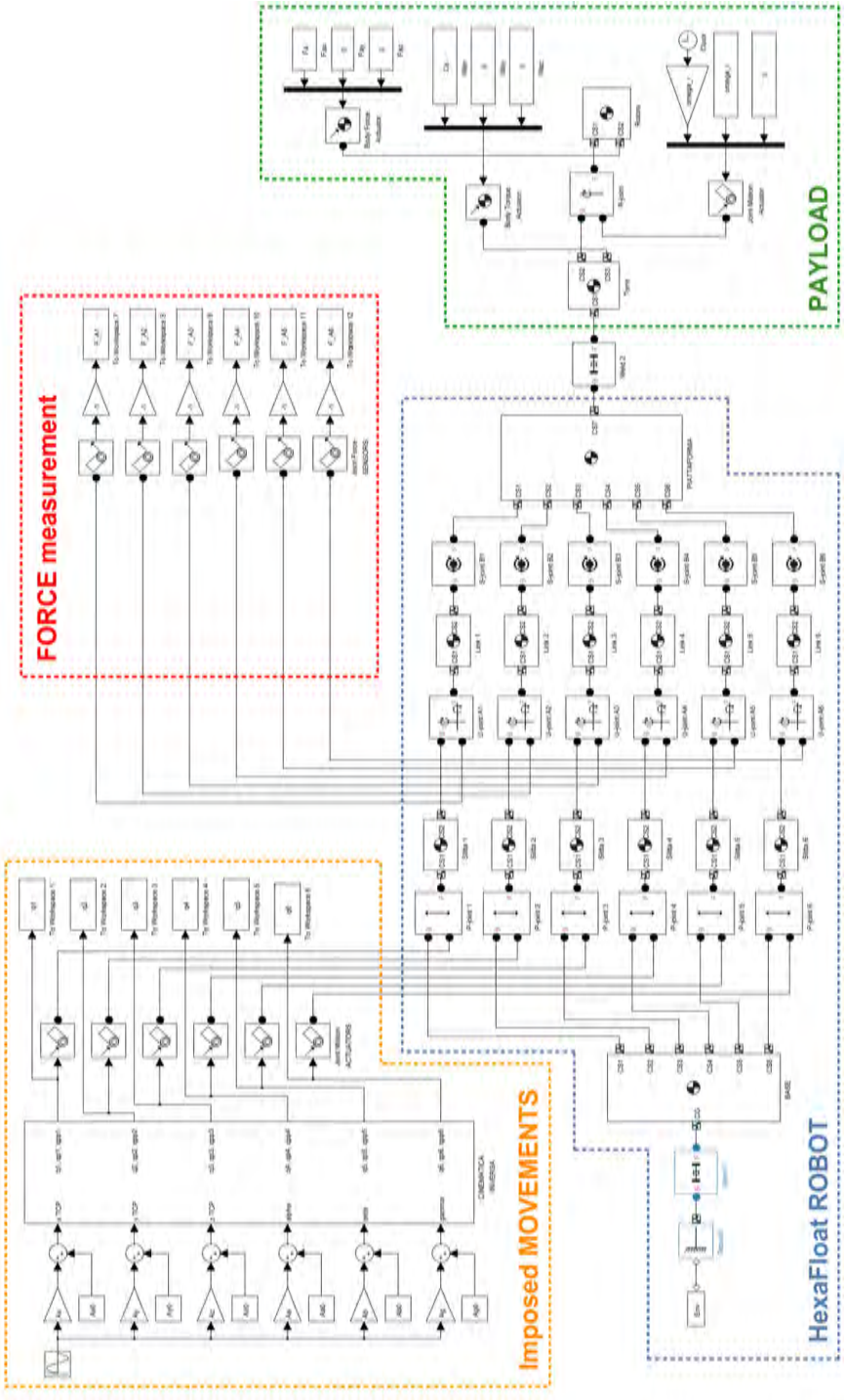

Fig. 12: Simulink model divided into functional macro-groups (payload: wind turbine model).

linear motions, (4) measurement of the force and moment components in every center A_i of the universal joints which connect the links to the sliders.

It is noted that for PKMs, because of their closed-loop chains, Simulink requires to select the *kinematics analysis mode* by setting the machine environment block. Moreover, it is important to observe that Simulink applies the actuation forces on the joints whose motion is imposed.

4.2. Forces evaluation

Through the ball joints centers B_i arranged on the platform, only axial forces and no moments can be discharged along the links. Measuring the force components in the opposite side of the links, that are the centers A_i of the universal joints, and comparing them with the components of the link unit vector $\hat{\mathbf{n}}_i$, it is possible to check that the force vector $\mathbf{F}_{A_i}$, with a good approximation, has always the link direction. The misalignment is negligible because it is caused only by the contribution of the link proper inertia and weight. For the same reason, the three moment components are negligible. Thanks to this approximation and to the rectilinear form of the links, the links loading mode is assumed of pure and uniform tension or compression, so that the force value is computed using the three components measured in A_i as:

$$|\mathbf{F}_{A_i}| = \sqrt{F_{A_i,x}^2 + F_{A_i,y}^2 + F_{A_i,z}^2} \tag{18}$$

The sign of the measured forces depends on the base(B)-follower(F) sequence set in the Simulink block diagram. In order to determine how to interpret this sign, a simple static test is performed and it is observed whether the sum $\sum_i F_{A_i,z}$ balances the total weight of the robot or coincides with it. By placing a sign change before the measurement, $F_{A_i,x}$ is the driving force transmitted to the robot through the i-th universal joint, while $F_{A_i,y}$ and $F_{A_i,z}$ are the reaction forces given by the i-th rail. Thus, when the force vector has the same versus of $\hat{\mathbf{n}}_i$, the link is under compression (−), while, when they have opposite versus, the link is under tension (+). Therefore, the axial force along the link can be written as:

$$N_{\text{link},i} = -\text{sign}(F_{A_i,x} \cdot n_{i,x}) \cdot |\mathbf{F}_{A_i}| \tag{19}$$

Finally, we observe that, since the motion of the system is rigidly imposed through the prismatic joints without other elements that connect the links to the rails, except the universal joints, the forces measured in A_i are independent of the drive system inertial properties. They depend only on the load inertia (links, mobile platform, payload). This observation is helpful because the contribution of different transmission units, including the mass of the sliders, and of different motor-reducer groups can be added later, without increasing the number of simulations.

4.3. Load inertial properties

The load inertial properties in this phase are simulated in a simplified manner as shown in Fig. 13, while the parameters values are reported in Tab. 3. With respect to the payload, four cases are taken into account: (1) wind turbine, (2) sail-boat, (3) bridge, and (4) high static load. The links are simulated as rods with length l_i, while the platform is the parallelepiped of minimum size containing the TCP and all the centers B_i of platform joints.

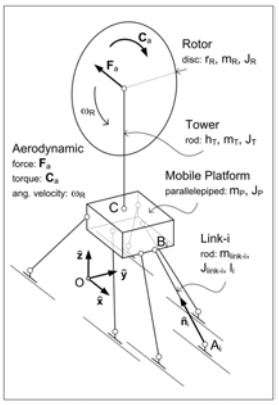

(a) Turbine

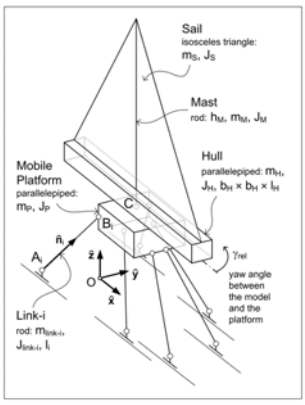

(b) Sail-boat

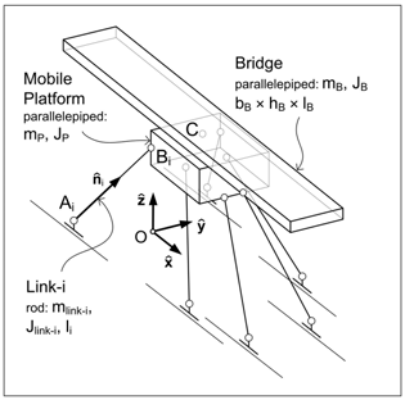

(c) Bridge

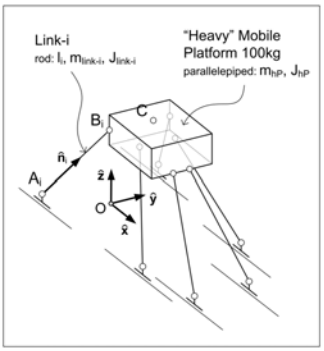

(d) Statics

Fig. 13: Inertias schematisation.

Symbol	Units	Values	Symbol	Units	Values
m_P	[kg]	35	m_{hP}	[kg]	100
m_{link-i}	[kg]	1.5	m_T	[kg]	7.0
h_T	[m]	1.7	m_R	[kg]	3.0
r_R	[m]	1.0	$\mathbf{F}_a$	[N]	0
$\mathbf{C}_a$	[Nm]	0	ω_R	[rad/s]	0
m_H	[kg]	4.0	b_H	[m]	0.15
l_H	[m]	1.5	m_M	[kg]	3.0
h_M	[m]	1.9	m_S	[kg]	3.0
γ_{rel}	[deg]	0	m_B	[kg]	20
b_B	[m]	0.3	h_B	[m]	0.1
l_B	[m]	2.0			

Tab. 3: Inertia parameters values.

4.4. Imposed movements

To probe the dynamic behaviour of the robot in a systematic and significant way, the desired workspace is divided into a grid of poses $\mathbf{X}_0$ (TCP position: $\{x_0, y_0, z_0\}$ and platform orientation: $\{\alpha_0, \beta_0, \gamma_0\}$). About each of them, a large amplitude sinusoidal movement is independently imposed on every of the six coordinates X_i of the mobile platform:

$$X_i(t) = X_{i,0} + A_{X_i} \sin(2\pi \bar{f} \cdot t) \tag{20}$$

with all the others coordinates set to $\mathbf{X}_0$. The frequencies and the amplitudes are the maximum prescribed by the requirements (see Tab. 1).

5. DRIVE SYSTEM

Different systems may be adopted to move the sliders. In this work two possible solutions are taken into account and compared to each other: (1) toothed belt and (2) ball screw. Complete units that implement these two types of solution are commercially available in various sizes. They are called *belt-driven units* and *ball-screw-driven units*. The main advantages of their adoption stand in their high precision and standardized quality.

5.1. LTU performance check

During the simulations, the three forces components in every joint center A_i are measured and the maximum values are saved. These values, together with the known sliders motions, allow the size selection the of i-th linear transmission unit (LTU), whose performances have to satisfy with an adequate margin: the maximum slider stroke $\max(q_i(t)) - \min(q_i(t)) + L_{\mathrm{WSd},x}$; the maximum slider velocity $\max|\dot{q}_i(t)|$ and acceleration $\max|\ddot{q}_i(t)|$; the maximum thrust force $\max|F_{A_i,x}|$; the maximum reaction forces $\max|F_{A_i,y}|$ and $\max|F_{A_i,z}|$; the maximum reaction moments $\max|M_{A_i,x}|$, $\max|M_{A_i,y}|$, and $\max|M_{A_i,z}|$. These moments depend on the arms b_x, b_y and b_z, of the forces applied in A_i with respect to the guideway center of the i-th transmission unit. They will be evaluated after the construction drawing:

$$\begin{aligned} M_{A_i,x} &= b_y \cdot F_{A_i,z} - b_z \cdot F_{A_i,y} \\ M_{A_i,y} &= b_z \cdot F_{A_i,x} - b_x \cdot F_{A_i,z} \\ M_{A_i,z} &= b_x \cdot F_{A_i,y} - b_y \cdot F_{A_i,x} \end{aligned} \tag{21}$$

5.2. Resistant torque

After selecting the candidate units to transmit the motion from the motors to the sliders, the total resistant torque is computed on each shaft of connection with the motor-reducer unit. Four different contributions can be recognize:

- the resistant torque due to the force discharged by the robot along the rail (balanced by the thrust force $F_{A_i,x}$) and to the force for accelerating the slider mass and possibly the belt: $T_{r,i_{\mathrm{thrust}}} = -G_{\mathrm{LTU}} \cdot [F_{A_i,x} + (m_{\mathrm{slider}} + m_{sb} \cdot k_{\mathrm{unit}}) \cdot \ddot{q}_i]$;
- the resistant idle torque due to the friction within the LTU, which is always opposite to the slider velocity: $T_{r,i_0} = -T_{r,0}(|n_i|) \cdot \mathrm{sign}(\dot{q}_i)$, where n_i is the number of revolutions per minute of the rotating element and $T_{r,0}(|n_i|)$ is a given function;
- the resistant torque due to friction between the slider and the respective rail because of the vertical force. It is always opposite to the slider velocity: $T_{r,i_\mu} = -G_{\mathrm{LTU}} \cdot \mu\,|F_{A_i,z} + (m_{\mathrm{slider}} + m_{sb})g| \cdot \mathrm{sign}(\dot{q}_i)$, where μ is the coefficient of friction;
- the resistant torque due to the inertia of the rotating masses of the LTU: $T_{r,i_{\mathrm{rot}}} = J_{rot} \cdot \frac{\ddot{q}_i}{G_{\mathrm{LTU}}}$.

G_{LTU} is the LTU gear ratio. In the case of ball-screw-driven unit: $G_{\mathrm{LTU}} = p_h/2\pi$, $m_{sb} = m_{\mathrm{screw}}$, $k_{\mathrm{unit}} = 0$, and $J_{rot} = J_{\mathrm{screw}}$. p_h is the pitch of the screw thread and m_{screw} is the mass of the screw. In the case of belt-driven unit: $G_{\mathrm{LTU}} = d_{\mathrm{pul}}/2$, $m_{sb} = m_{\mathrm{belt}}$, $k_{\mathrm{unit}} = 1$, $J_{rot} = J_{\mathrm{pulleys}}$. d_{pul} is the pulley diameter and m_{belt} is the mass of the belt.

The total resistant torque is obtained as the sum of the four contributions:

$$T^*_{r,i}(t) = T_{r,i_{\mathrm{thrust}}} + T_{r,i_0} + T_{r,i_\mu} + T_{r,i_{\mathrm{rot}}} \tag{22}$$

The shaft on which the torque is computed is the screw itself or the output shaft of one of two pulleys. With the asterisk in superscript, it is common to indicate that the resistant torque already includes the inertial contributions. In the following, the subscript i, which distinguishes between the various actuation axes, is omitted.

5.3. Motor-reducer choice

Calling T_m the motor torque, the electric motor selection is based on the following checks:

1. the maximum instantaneous torque: $\max |T_m(t)| < T_{m,\max}$;
2. the mean square torque (thermal check): $T_{m,\text{rms}} < T_{m,\text{nom}}$;
3. the maximum instantaneous angular velocity: $\max |\omega_r(t)|/G < \omega_{m,\max}$.

where $G = \omega_r/\omega_m$ is the gear ratio provided by the reducer, which is assumed to be ideal, without inertia and with efficiency equal to 1.

To perform the first two checks it is necessary to express the motor torque in terms of the resistant one, by writing the power balance referred to the output motor shaft $T_m = -G\,T_r^* + J_m\omega_r/G$, where J_m is the moment of inertia of the motor.

The thermal check, based on the root mean square value of the motor torque, can be written as:

$$\alpha > \beta + \left[T^*_{r,\text{rms}} \left(\frac{G}{\sqrt{J_m}} \right) - \dot{\omega}_{r,\text{rms}} \left(\frac{\sqrt{J_m}}{G} \right) \right]^2 \tag{23}$$

where the quantities α and β are introduced, following the theory in [25, 26, 27]. $\alpha = T_n^2/J_m$ is the so-called *accelerating factor*. It depends only on the motor and so it characterizes the provided performances. $\beta = 2\left[\dot{\omega}_{r,\text{rms}}\,T^*_{r,\text{rms}} + \left(\dot{\omega}_r(t)\,T_r^*(t)\right)_{\text{average}}\right]$ is the so-called *load factor*. It depends only by the load and so it characterizes the required performances. Then, the term added to β in the second member of the Eq. 23 is a mixed term, in which appears the transmission ratio G. As can be seen, it is always positive and always increases β, so that the required α is surely higher than β. It is called optimum transmission ratio the value of G for which this mixed term is deleted: $G_{\text{opt}} = \sqrt{J_m\dot{\omega}_{r,\text{rms}}/T^*_{r,\text{rms}}}$, while, in general, the transmission ratio can vary between a minimum value and a maximum one:

$$G_{\min}, G_{\max} = \sqrt{J_m}\,\frac{\sqrt{\alpha - \beta + 4\,\dot{\omega}_{r,\text{rms}}\,T^*_{r,\text{rms}}} \pm \sqrt{\alpha - \beta}}{2\,T^*_{r,\text{rms}}} \tag{24}$$

The third check for selecting the motor concerns with the maximum instantaneous speed required and can be read in this way: there is an inferior limit for the transmission ratio, under which the motor is no longer able to generate the required velocity of the load: $G > G_{\min,\omega} = \max |\omega_r(t)|/\omega_{m,\max}$. The maximum angular velocity of the motor $\omega_{m,\max}$ is often given by the supply voltage, even before by a mechanical constrain $\omega_{m,mech}$.

Taken into account some catalogues of motors and reducers, after computing β_{MAX} of the robot on all the movements imposed during the simulations, the sizing method of the motor-reducer unit prescribes the following steps:

1. computation of α for all the motors available in the catalogue: all those for whom $\alpha < \beta_{\text{MAX}}$ are discarded;
2. computation of $G_{\min}$, $G_{\max}$, $G_{\min,\omega}$: all the motors for whom $G_{\min,\omega} > G_{\max}$ are discarded;
3. a particular choice is considered feasible if $\max\left(G_{\min,\omega}, G_{\min}\right) < \bar{G} < G_{\max}$, where $\bar{G}$ is the transmission ratio of an available reducer;
4. the maximum available torque is checked to be greater than the required one.

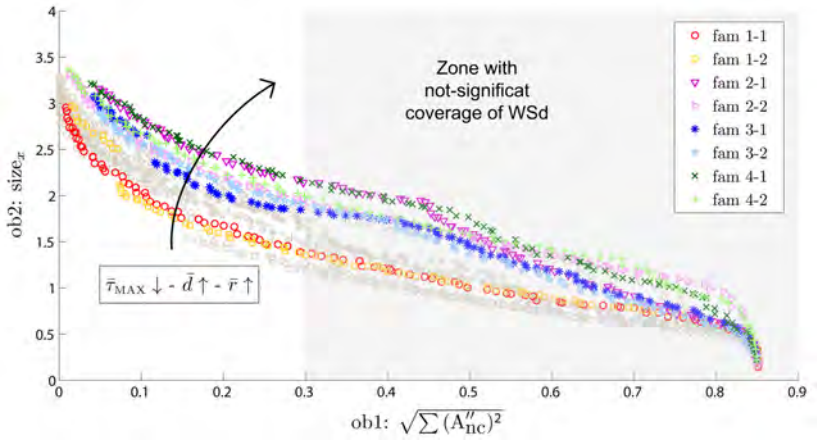

Fig. 14: Pareto fronts all families except Fam. 5, with $\bar{\tau}_{MAX} = 20$, $\bar{d} = 10$cm, and $\bar{r} = 10$cm.

6. RESULTS

6.1. Multi-objective optimization

For each architectural family, the optimization process reached the convergence with the desired tolerance, except for family 5, because its links arrangement always produces individuals characterized by permanent singularities. Each Pareto-optimal point was analysed and compared to the other points by mapping the kinetostatic performances on the total oWS. Fig. 14 shows the Pareto fronts obtained with $\bar{\tau}_{MAX} = 20$, $\bar{d} = 10$ cm, and $\bar{r} = 10$ cm. These values were chosen with a trial-and-error approach, proving that with a lower threshold on τ_{MAX} or bigger thresholds on d and r, the Pareto fronts left the most interesting zone in terms of WSd coverage. The same figure, in light gray color, also shows the Pareto fronts with $\bar{\tau}_{MAX} = 50$, $\bar{d} = 10$ cm, and $\bar{r} = 0$ cm, which represent a less restrictive condition. The options of *gamultiobj.m* were set to: PopSize = 300, TolFun = 1e−5. The average computation time to obtain one Pareto front was 45 h with Intel i7-2760QM 2.40 GHz quad-core CPU. This computation was performed using parallel computing, which allows the 100% CPU usage on multi-core processors.

The best compromise solution was identified as the Pareto point n. 4 belonging to family 1-1 (p.p. 4 Fam. 1-1). Its dimensions, schematics views and 3D total oWS are reported in Fig. 15, Tab. 4, and Tab. 5. The kinematic and kinetostatic objectives are mapped in Fig. 16, which shows: the maximum static forces multiplication along the links, Fig. 16(a) and Fig. 16(b); the link-to-link interference, Fig. 16(c) and Fig. 16(d); the link-to-rail interference, Fig. 16(e) and Fig. 16(f). To compute the total oWS, two different tilt angles were considered for all the joints: $\bar{\theta}_{\max,S_i} = 40°$, to perform the optimization, and $\bar{\theta}_{\max,S_i} = 45°$, as mobility limit.

6.2. Joint centering

In Fig. 17 it is shown the increase of extension in the total oWS because of the joint centering, using the same tilt angles. As can be seen for this representative case, the effective gain given by the centering procedure is almost null. Since this is true for all the analysed cases, it means that the joints are already uniformly saturated with respect to their mobility range, and, therefore, the home pose was proved to be a good parametrization choice. However, this don't give us

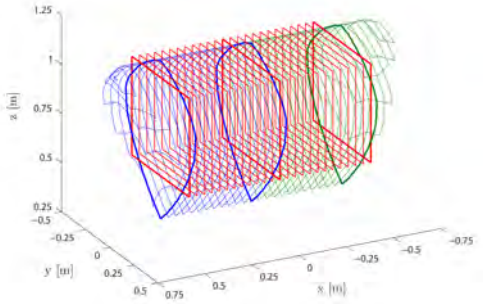

(a) 3D total oWS

Total oWS	$\alpha, \beta, \gamma = \pm 15°$
Joints title angle	$\bar{\theta}_{max,S_i} = 45°$
Stroke-1&6 ($A_{0,x}$) [mm]	2270 (-1377)
Stroke-2&5 ($A_{0,x}$) [mm]	2060 (8)
Stroke-3&4 ($A_{0,x}$) [mm]	2247 (-1552)
xy-size [mm]	3620×1150

Tab. 4: Stroke and size (p.p. n. 4 Fam. 1-1)

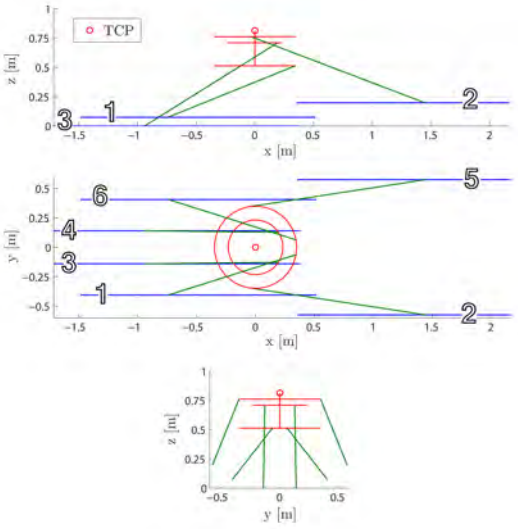

(b) 2D views

Fig. 15: Pareto point n. 4 Fam. 1-1

Parameter	Symbol	Unit of m.	Opt. value	Min.	Max.
1) links length 1&6	l_{01}	[mm]	1220	500	1600
2) links length 2&5	l_{02}	[mm]	1598	500	1600
3) links length 3&4	l_{03}	[mm]	1338	500	1600
4) rails Δy 1&6	s_{01}	[mm]	406	100	750
5) rails Δy 2&5	s_{02}	[mm]	575	100	750
6) rails Δy 3&4	s_{03}	[mm]	140	100	750
7) half-angle $B_1\widehat{C_{01}}B_6$	β_{01}	[deg]	169.6°	10°	170°
8) half-angle $B_2\widehat{C_{01}}B_5$	β_{02}	[deg]	95.1°	10°	170°
9) half-angle $B_3\widehat{C_{01}}B_4$	β_{03}	[deg]	146.7°	10°	170°
10) radial distance $\overline{C_{01}B_{1,6}}$	r_{01}	[mm]	350	50	350
11) radial distance $\overline{C_{02}B_{2,5}}$	r_{02}	[mm]	350	50	350
12) radial distance $\overline{C_{03}B_{3,4}}$	r_{03}	[mm]	233	50	350
13) vertical distance $\overline{CC_{01}}$	t_{01}	[mm]	300	50	300
14) vertical distance $\overline{CC_{02}}$	t_{02}	[mm]	51	50	300
15) vertical distance $\overline{CC_{03}}$	t_{03}	[mm]	104	50	300
16) desired WS heigth	z_{WSd}	[mm]	782	700	900
17) home pose heigth	z_{JHP}	[mm]	813	700	900
18) rails Δz 1&6	$s_{h,01}$	[mm]	74	0	200
19) rails Δz 2&5	$s_{h,01}$	[mm]	198	0	200

Tab. 5: Geometric parameters: optimized values and ranges (p.p. 4 Fam. 1-1).

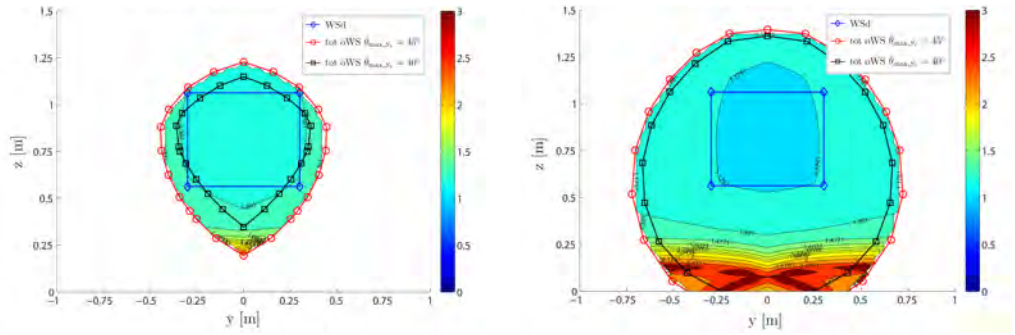

(a) Max. τ with $\alpha, \beta, \gamma = \pm 15°$

(b) Max. τ with $\alpha, \beta, \gamma = 0°$

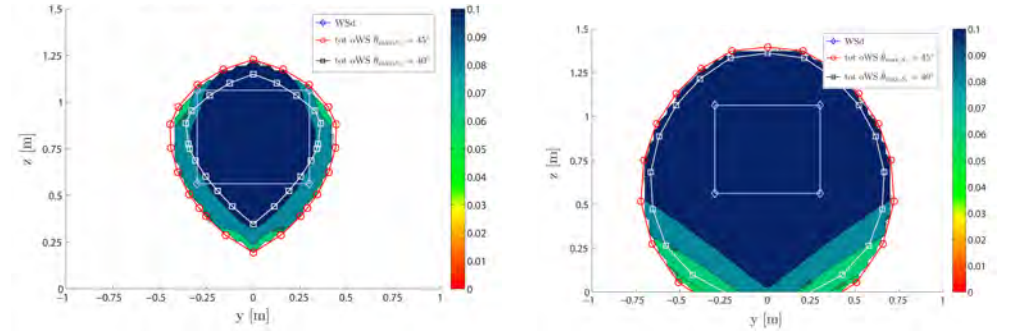

(c) Min. d (m) with $\alpha, \beta, \gamma = \pm 15°$

(d) Min. d (m) with $\alpha, \beta, \gamma = 0°$

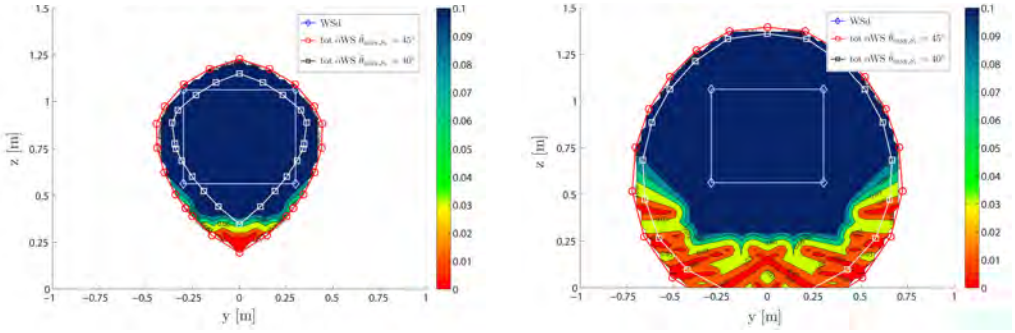

(e) Min. r (m) with $\alpha, \beta, \gamma = \pm 15°$

(f) Min. r (m) with $\alpha, \beta, \gamma = 0°$

Fig. 16: Objectives maps (p.p. 4 Fam. 1-1).

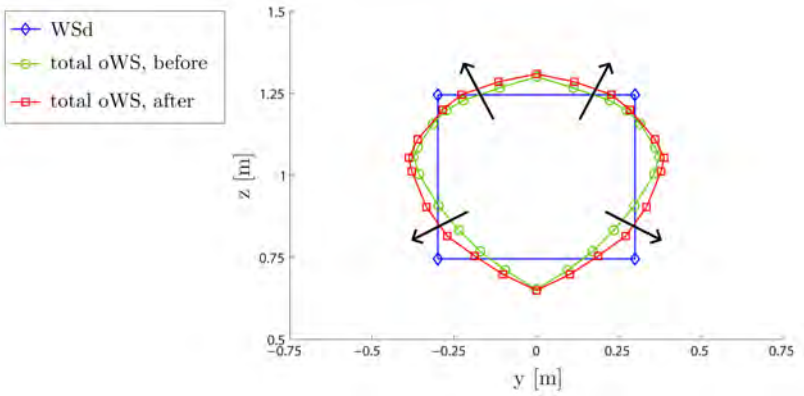

Fig. 17: Total oWS before and after the joint centering (representative case).

information about the possibility to obtain better solutions without imposing the presence of the home pose: the JHP families are a subset of those without the JHP, so that an optimization with 30 parameters instead of 19 should provide solutions at least equally good. This is really true only with an adequate number of individuals, which allows the genetic algorithm to significantly cover the whole decision space. However, more parameters and more individuals imply a more than linear increase in the computation time. That's why the optimization with 30 parameters wasn't consider a viable option.

It is worth noting that the joints on the mobile platform are saturated much before than the joints on the base. Finally, it is noticed that z_{JHP} is always very close to z_{WSd} (see Tab. 5), so that they might be a single parameter in any future optimization.

6.3. Static and dynamic analysis

The static and dynamic analysis was conducted on several Pareto-optimal individuals, except on those belonging to family 5, which always have singularity problems because of their particular linkages arrangement. In Tab. 6 are indicated the computational parameters. In particular, to minimize the simulation time, the Simulink model was run only for one period $\bar{T} = 1/\bar{f}$ of the sinusoidal movements of the platform.

For each of the analysed individuals, the velocities, accelerations and forces distributions over the desired workspace were represented through appropriate maps. By this way, the different families were easily compared and the individual n. 4, belonging to family 1-1 and obtained with $\bar{\tau}_{\text{MAX}} = 20$, was definitely selected as the best compromise solution. Fig. 18 shows the distribution maps of the maximum axial forces for the static case, which was proved to be the worst case among the analysed ones in terms of maximum forces. In this figure three significant Pareto-optimal individuals are compared: (center) the best one; (left) an individual belonging to the same family of the best individual, but obtained with a bigger threshold $\bar{\tau}_{\text{MAX}} = 50$; (right) an individual obtained with the same threshold $\bar{\tau}_{\text{MAX}} = 20$ of the best individual, but belonging to the worst family, which is the family 3-2. As can be seen, decreasing the kinetostatic threshold $\bar{\tau}_{\text{MAX}}$ in the synthesis phase was proved to be an effective way to decrease the maximum actual static and dynamic forces. Furthermore, having more architectural families allowed to completely explore the maximum performances achievable by the HexaFloat kinematic topology, within the

Robot poses: evaluation grid	
$N_y \rightarrow$ y span: $\Delta y = \frac{L_{\mathrm{WSd},y}}{N_y}$	17
$N_z \rightarrow$ z span: $\Delta z = \frac{L_{\mathrm{WSd},z}}{N_z}$	17
Grid of orientations	27 orientation
Simulink solver: options	
Simulation time	$1/\tilde{f}$ (one period)
Time interval	0.01s
Solver type	discrete, fixed-step
"Machine Environment"	analisys mode: kinematics
Use of computational (1 individual × 4 cases)	
Computation time	6 h
CPU utilization	15 %
RAM utilization	2.30 GB
CPU	quad-core 2.40 GHz

Tab. 6: Evaluation grids, Simulink solver options and computational resources.

ranges of the geometric parameters imposed in the optimization phase. Finally, it is noted that, the axial forces tends always to increase at the bottom of the workspace. This happens because the lower the TCP position is, the more the links tend to lie horizontal: the robot moves toward singular configurations and the transmission ratios become unfavourable. This is a characteristic of the Hexaglide kinematic topology, which is able to reach poses very closed to its fixed base but at the cost of bigger actuation forces.

6.4. LTUs selection and β maps

The transmission units suitable to realize the linear motions of the sliders were selected in accordance to the maximal values reported in Tab. 7, where the required performances are compared with the provided ones. Two systems belonging to Thomson-Danaher catalogue [28] were considered: the screw-driven unit WM80D, and the belt-driven unit WH120. They satisfy with an adequate margin the most demanding requests. It is noted that for the screw transmission the maximum available pitch $p_h = 50$ mm is necessary to achieve the required maximum sliders velocity. Considering that it is twice the screw diameter ($d_{0,\mathrm{screw}} = 25$ mm), this pitch is closed to the technology limit for screw-ball transmissions.

		WM80D	WH120	Fam. 1-1
		$p_h = 50$ mm		ind. 4
$v_{\max}$	[m/s]	2.5	10	2.20
$a_{\max}$	[m/s^2]	20	40	13.02
$F_{A_i,x}$ (LTU thrust)	[N]	5000	5000	2308
$F_{A_i,y}$ (LTU y-reaction)	[N]	3000	4980	709
$F_{A_i,z}$ (LTU z-reaction)	[N]	3000	9300	764

Tab. 7: LTUs selection: required vs. provided performances.

Then, also the load factor distribution maps was produced. They allowed a further comparison between the families and between the different payloads and movements, but also between the two types of transmission. In Fig. 19 the maximum β maps are shown for the most demanding

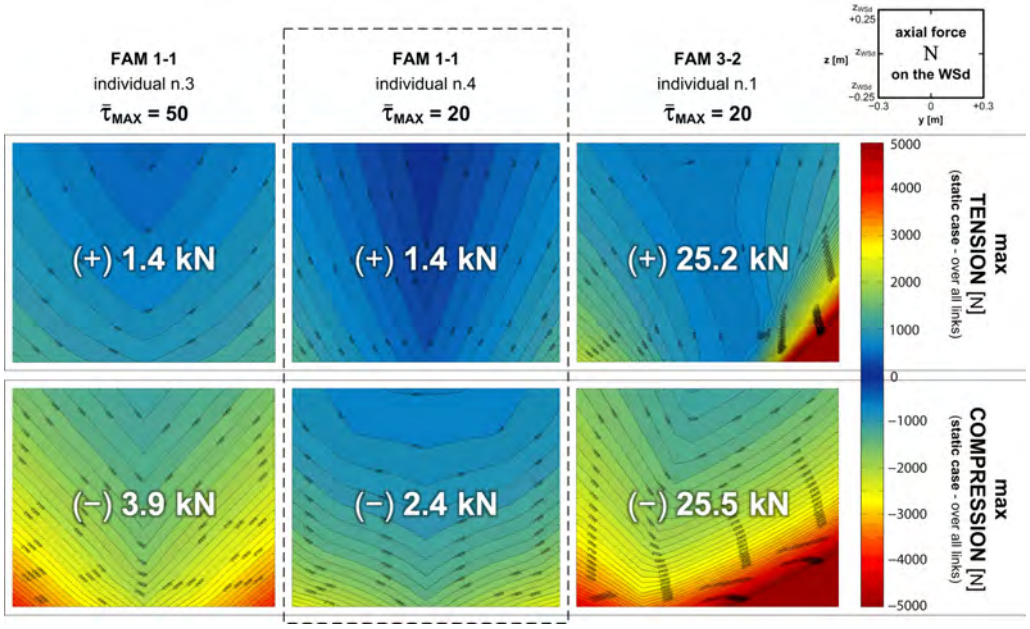

Fig. 18: Axial force distributions over the desired workspace, maximum for all the links. N_{link} worst-case: static case with $m_P = 100$ kg.

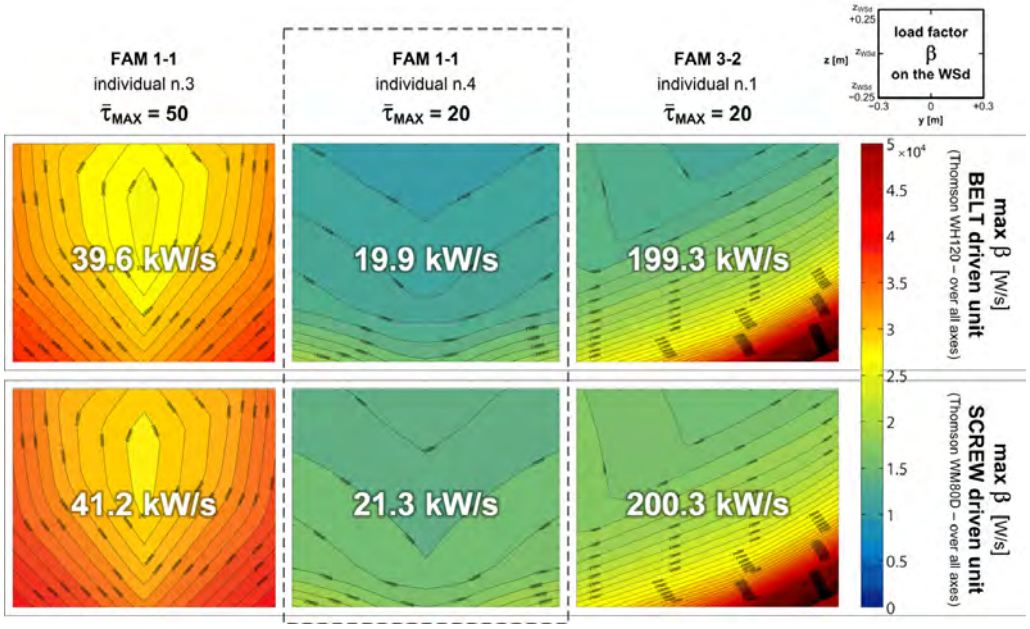

Fig. 19: Load factor distributions over the desired workspace, maximum for all the actuated axes. β worst-case: x movement for the wind turbine.

movement, which was proved to be the motion along x in the case of the wind turbine. In this figure, three significant Pareto-optimal individuals previously considered are compared again and analogues considerations can be made. As can be seen, the maximum β is similar for both types of transmissions, mainly because their inertial contributions are of the same order of magnitude, as clearly shown in Tab. 8, reducing them to equivalent linear-moving masses. This equivalence in the use of the selected belt- or screw-driven units, is made possible only because, for the considered screw-driven unit, a very long pitch is available. It is noted that the inertial contribution of the linear units is present within two components of the resistant torque: $T_{r_{\text{thrust}}}$ and $T_{r_{\text{rot}}}$. In particular, the second one, which is related to rotating masses, would increase significantly if the screw pitch decreases, becoming the main contribution to the total resistant torque. This happens because an increasingly higher angular acceleration of the screw is needed to provide the same linear acceleration of the slider.

Equivalent linear-moving mass [kg]							
Screw-driven unit: WM80D							
p_h [mm]	$\rightarrow$	$\frac{J_{\text{screw}}}{[p_h/(2\pi)]^2}$	+	m_{slider}	=	$m_{\text{WM80D},eq}$	$\frac{F_{1g}}{\max F_{A_i,x}}$
50		9.2		4.3		13.5	9%
20		57.7		4.3		61.8	43%
10		230.9		4.3		235.2	166%
5		923.8		4.3		928.1	658%
Belt-driven unit: WH120							
$\frac{J_{pulleys}}{(d_0/2)^2}$	+	m_{belt}	+	m_{slider}	=	$m_{\text{WH120},eq}$	$\frac{F_{1g}}{\max F_{A_i,x}}$
0.6		1.77		5.50		7.9	6%

Tab. 8: Inertial contributions given by the LTUs, referred to the sliders. F_{1g} is the force to accelerate $m_{\text{LTU},eq}$ with 1g. $\max F_{A_i,x} = 1384$N is the maximum thrust force required to realize an acceleration $\ddot{q}_i \approx 1$g, in the dynamic case of the wind turbine, for the individual n. 4 family 1-1 $\bar{\tau}_{\text{MAX}} = 20$.

6.5. Motor-reducer selection

The motor-reducer selection diagrams are shown in Fig. 20, Fig. 21 and Fig. 22. They were produced according to the maximum values reported in Tab. 9. The AKM series brushless motors belonging to Kollmorgen-Danaher catalogue [29] and the ValueTRUE reducers belonging to Micron-Danaher catalogue [30] were considered. The motors were numbered in ascending order according to their size and a supply voltage equal to 230 Vac was assumed. Then, Tab. 10 and Tab. 11 show the first feasible choices of motor-reducer group with respect to the motor size. They satisfy all the performances checks, even the one on maximum available torque, with an adequate motor-load inertia ratio [1]: $K_{m|l} > 0.3$.

[1] In robotics applications, the motor-load inertia ratio $K_{m|l}$ have to be as close as possible to 1 to ensure low acceleration times and fast control responses (inertia matching). $K_{m|l}$ is computed as:

$$K_{m|l} = \frac{J_m}{J_{\text{load},eq}} = \frac{J_m}{G_{\text{LTU}}^2 \bar{G}^2 m_{\text{load},eq} + J_{\text{reducer}}} \tag{25}$$

in which:

$$m_{\text{load},eq} = m_{A_i,eq} + m_{\text{LTU},eq} = \max\left(\frac{F_{A_i}(t)}{\ddot{q}_i(t)}\right) + m_{\text{LTU},eq} \tag{26}$$

$m_{A_i,eq}$ has its maximum value in the case of the wind turbine x movement: 1384N/9.67m/s^2 = 143.1kg

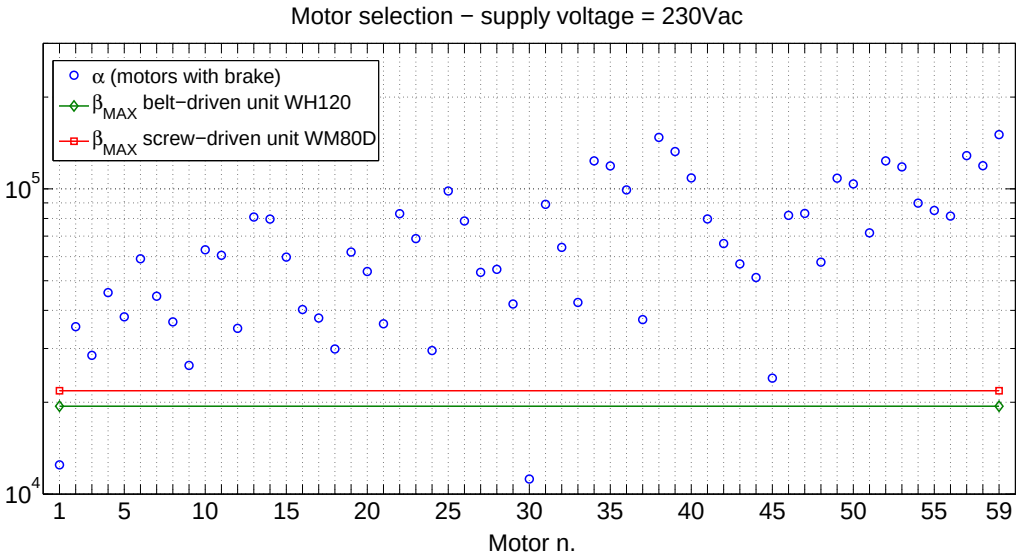

Fig. 20: Load factor β vs. accelerating factor α (AKM Kollmorgen-Danaher motors).

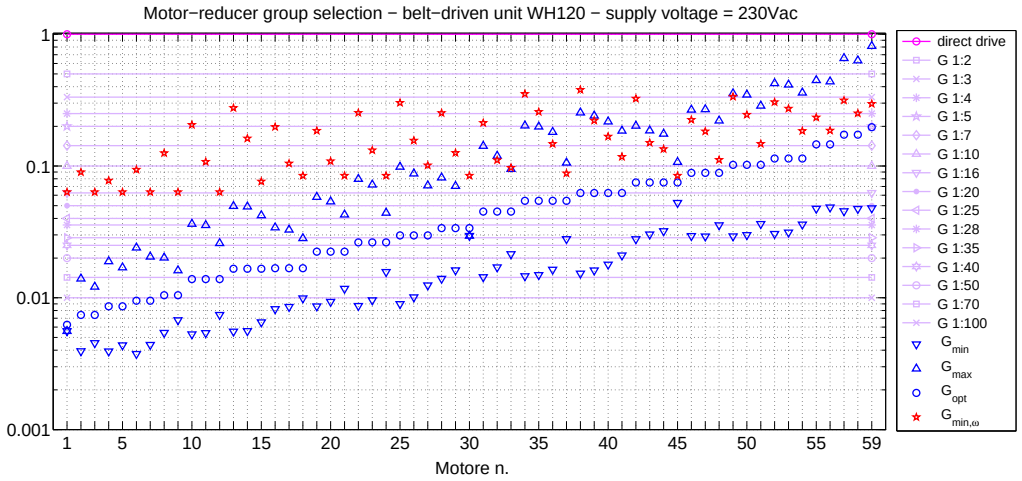

Fig. 21: Reducer transmission ratio in case of belt-driven unit: required range vs. available $\bar{G}$ (ValueTRUE Micron-Danaher reducers).

		WM80D	WH120
β_{MAX}	[kW/s]	21.3	19.9
$T^*_{r,\text{rms}}$	[Nm]	6.81	52.2
$\dot{\omega}_{r,\text{rms}}$	[rad/s^2]	868	167

Tab. 9: RMS values of the resistant torque and angular acceleration of the load, corresponding to β_{MAX} detected in the case of the wind turbine x movement.

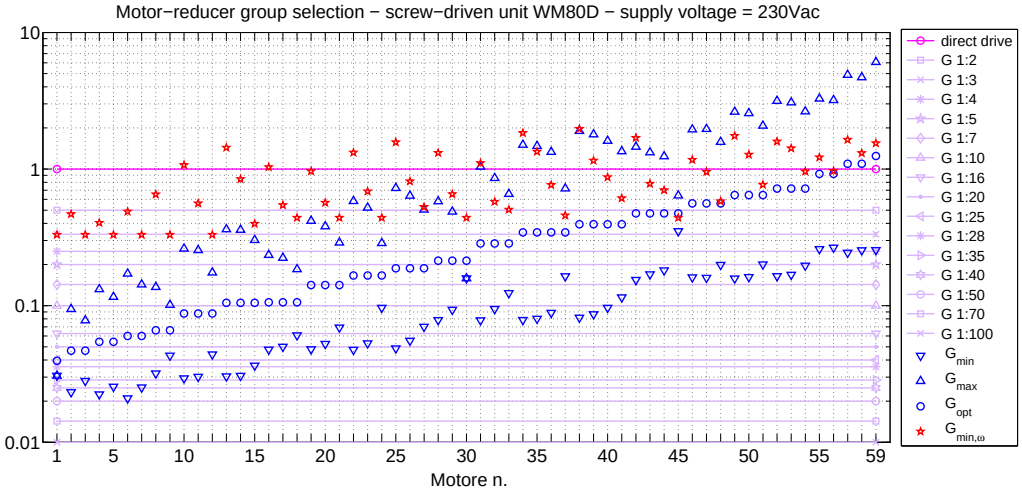

Fig. 22: Reducer transmission ratio in case of screw-driven unit: required range vs. available $\bar{G}$ (ValueTRUE Micron-Danaher reducers).

Maximum torque check - belt-driven unit WH120 $G_{\text{LTU}} = \frac{d_{pul}}{2} = 0.041\text{m/rad}$				
		Turbine	Turbine	Statics
		y mov.	y mov.	$m_P = 100\text{kg}$
T_r^*	[Nm]	91.8 (max)	35.2	170.3
$\dot{\omega}_r$	[rad/s^2]	139.7	348.2 (max)	0
Motor-reducer group: AKM5-3P (n.37) with VT115-010 ($\bar{G} = 1:10$) $J_{\text{load},eq} = 25.5\text{kg·cm}^2$ con $J_{\text{reducer}} = 0.90\text{kg·cm}^2 \rightarrow K_{m\|l} = 0.36$				
J_m with brake	[kg·cm^2]	9.3	9.3	–
$T_{m,\max}$ **required**	[Nm]	10.5	6.8	17.0
$T_{m,\max}$ **available**	[Nm]	29.8	29.8	29.8

Tab. 10: Maximum torque check: required vs. available, in the cases of: max resistant torque, max angular velocity, max static torque.

CONCLUSIONS

This paper presents the task-oriented customization of a 6-DoF parallel robot, designed to perform HIL dynamic test in the low-speed test section of the Politecnico di Milano wind tunnel. To satisfy the given requirements, a mechatronic design approach was used. The core of the work is the kinetostatic synthesis of the machine, obtained through a multi-objective optimization process, using a genetic algorithm. The emphasis is placed on the developed procedure and its effectiveness, so that other mechanisms architectures or different requirements may be taken into account. Further works will include the vibration analysis of the machine in connection with its positioning task-space error, introducing the flexibility of all the components.

Maximum torque check - screw-driven unit WM80D $G_{\text{LTU}} = \frac{p_h}{2\pi} = 8.0 \cdot 10^{-3}$m/rad				
		Turbine	Turbine	Statics
		y mov.	y mov.	$m_P = 100$kg
T_r^*	[Nm]	19.9 (max)	9.9	32.8
$\dot{\omega}_r$	[rad/s^2]	726.3	1810 (max)	0
Motor-reducer group: AKM6-4Q (n.51) with "direct drive" $J_{\text{load},eq} = 97.2\text{kg}\cdot\text{cm}^2 \rightarrow K_{m\|l} = 0.34$				
J_m con freno	[kg·cm^2]	32.6	32.6	–
$T_{m,\max}$ **required**	[Nm]	22.3	15.8	32.8
$T_{m,\max}$ **available**	[Nm]	53.2	53.2	53.2

Tab. 11: Maximum torque check: required vs. available, in the cases of: max dynamic resistant torque, max angular velocity, max static torque.

References

[1] Bayati, I., Belloli, M., Facchinetti, A., Giappino, S., 2013, Wind Tunnel Tests on Floating Offshore Wind Turbines: A Proposal for Hardware-in-the-Loop Approach to Validate Numerical Codes, *Wind Engineering Journal*, **37**(6), pp. 557-568.

[2] Bayati, I., Belloli, M., Ferrari, D., Fossati, F., Giberti, H., 2014, "Design of a 6-DoF Robotic Platform for Wind Tunnel Tests of Floating Wind Turbines", *Energy Procedia Journal*, **53**, pp. 313-323.

[3] Giberti, H., Cinquemani, S., Ambrosetti, S., 2013, "5R 2dof parallel kinematic manipulator, A multidisciplinary test case in mechatronics", *Mechatronics - Elsevier Journal*, **23**(8), pp. 949959.

[4] Weck, M., Staimer, D., 2002, "Parallel Kinematic Machine Tools: Current State and Future Potentials", *CIRP Annals, Manufacturing Technology - Elsevier Journal*, **51**, pp. 671-683.

[5] Ferrari D., Giberti H., 2014, "A Genetic Algorithm Approach to the Kinematic Synthesis of a 6-DoF Parallel Manipulator", *Proceedings of IEEE Multi-Conference on Systems and Control*, Antibes, France, October 8-10.

[6] Giberti H., Ferrari D., 2014, "Drive System Sizing of a 6-DoF Parallel Robotic Platform", *Proceedings of ASME 12th Biennial Conference on Engineering Systems Design and Analysis, ESDA2014*, Copenhagen, Denmark, June 25-27.

[7] Merlet, J.P., 2006, "Parallel Robots", 2nd ed., Springer.

[8] Honegger, M., Codourey, A., Burdet, E., 1997, "Adaptive Control of the Hexaglide, a 6-DoF Parallel Manipulator", *Proceedings of IEEE International Conference on Robotics and Automation*, **1**, pp. 543-548.

[9] Honegger, M., 1999, "Konzept einer Steuerung mit Adaptiver Nichtlinearer Regelung fr einen Parallelmanipulator", Ph.D. thesis, ETH, Zürich.

[10] Hebsacker, M., 2000, "Entwurf und Bewertung Paralleler Werkzeugmaschinen - das Hexaglide", Ph.D. thesis, ETH, Zürich.

[11] Bonev, I.A., 1998, "Analysis and Design of a 6-DOF 6-PRRS Parallel Manipulators", M.Sc. thesis, GIST, South Korea.

[12] Bonev, I. A., 2001, "A geometrical method for computing the constant-orientation workspace of 6-PRRS parallel manipulators", *Mechanism and Machine Theory*, **36**, pp. 1-13.

[13] Bergmann, A., 2005, "The Model Positioning Mechanism of DNW-NWB based on a New Parallel Kinematic", *Proceedings of Aerospace Testing Expo at Hamburg - Germany*, DNW German-Dutch Wind Tunnels.

[14] Bergmann, A., Loeser, T., 2006, "Capabilities of Deployment Tests at DNW-NWB", *Meeting paper for US Defence Technical Information Center*, DNW German-Dutch Wind Tunnels.

[15] Merlet, J.P., 2009, "Interval Analysis for Certified Numerical Solution of Problems in Robotics", *International Journal of Applied Mathematics and Computer Science*, **19**(3), pp. 399-412.

[16] Merlet, J.P., 2009, "Interval Analysis and Reliability in Robotics", *International Journal of Reliability and Safety*, **3**(1-3), pp. 104-130.

[17] Koteswara Rao, A.B., Rao, P.V.M., Saha, S.K., 2005, "Dimensional Design of Hexaslides for Optimal Workspace and Dexterity",*IEEE Transactions On Robotics*, **21**(3), pp. 444-449.

[18] Fassi, I., Legnani, G., Tosi, D., 2005, "Geometrical Conditions for the Design of Partial or Full Isotropic Hexapods", *Journal of Robotic Systems*, **22**(10), pp. 507-518.

[19] Legnani, G., Tosi, D., Fassi, I., Giberti, H., Cinquemani, S., 2010, "The Point of Isotropy and other Properties of Serial and Parallel Manipulators", *Mechanism and Machine Theory*, **45**(10), pp. 1407-1423.

[20] Legnani, G., Fassi, I., Giberti, H., Cinquemani, S., Tosi, D., 2012, "A New Isotropic and Decoupled 6-DoF Parallel Manipulator", *Mechanism and Machine Theory*, **58**, pp. 64-81.
[21] Kalyanmoy, D., 2001, "Multi-Objective Optimization using Evolutionary Algorithms", Wiley.
[22] Barequet, G., Elbert, G., 2005, "Optimal Bounding Cones of Vectors in Three Dimensions", *Information Processing Letters - Elsevier Journal*, **93**(2), pp. 83-89.
[23] Kim, J.P., Ryu, J., 2002, "Inverse Kinematic and Dynamic Analyses of 6-DOF PUS Type Parallel Manipulators", *KSME International Journal*, **16**(1), pp. 13-23.
[24] Ruiz-Garca, J., Chaparro-Altamirano, D., Zavala-Yoe, R., Ramrez-Mendoza, R., 2013, "Direct and Inverse Dynamics Modeling of a 6-PUS Parallel Robot", *Proceedings of the International Conference on Mechatronics, Electronics and Automotive Engineering*, article number 6713950, pp. 21-26.
[25] Giberti, H., Cinquemani, S., Legnani, G., 2011, "A practical approach to the selection of the motor-reducer unit in electric drive systems", *Mechanics Based Design of Structures and Machines*, **39**(3), pp. 303-319.
[26] Giberti, H., Cinquemani, S., Legnani, G., 2010, "Effects of Transmission Mechanical Characteristics on the Choice of a Motor-Reducer", *Mechatronics - Elsevier Journal*, **20**, pp. 604 - 610.
[27] Giberti, H., Clerici, A., Cinquemani, S., 2014, "Specific Accelerating Factor: One More Tool in Motor Sizing Projects", *Mechatronics - Elsevier Journal*, **24**(7), pp. 898-905.
[28] Thomson-Danaher, 2012, "Linear Motion Systems Catalogue", `www.thomsonlinear.com`.
[29] Kollmorgen-Danaher, 2013, "Automation and Motion Solutions Catalog", `www.kollmorgen.com`.
[30] Micron-Danaher, 2012, "True Planetary Gearheads", `www.thomsonlinear.com`.

Figure(s)

Click here to download high resolution image

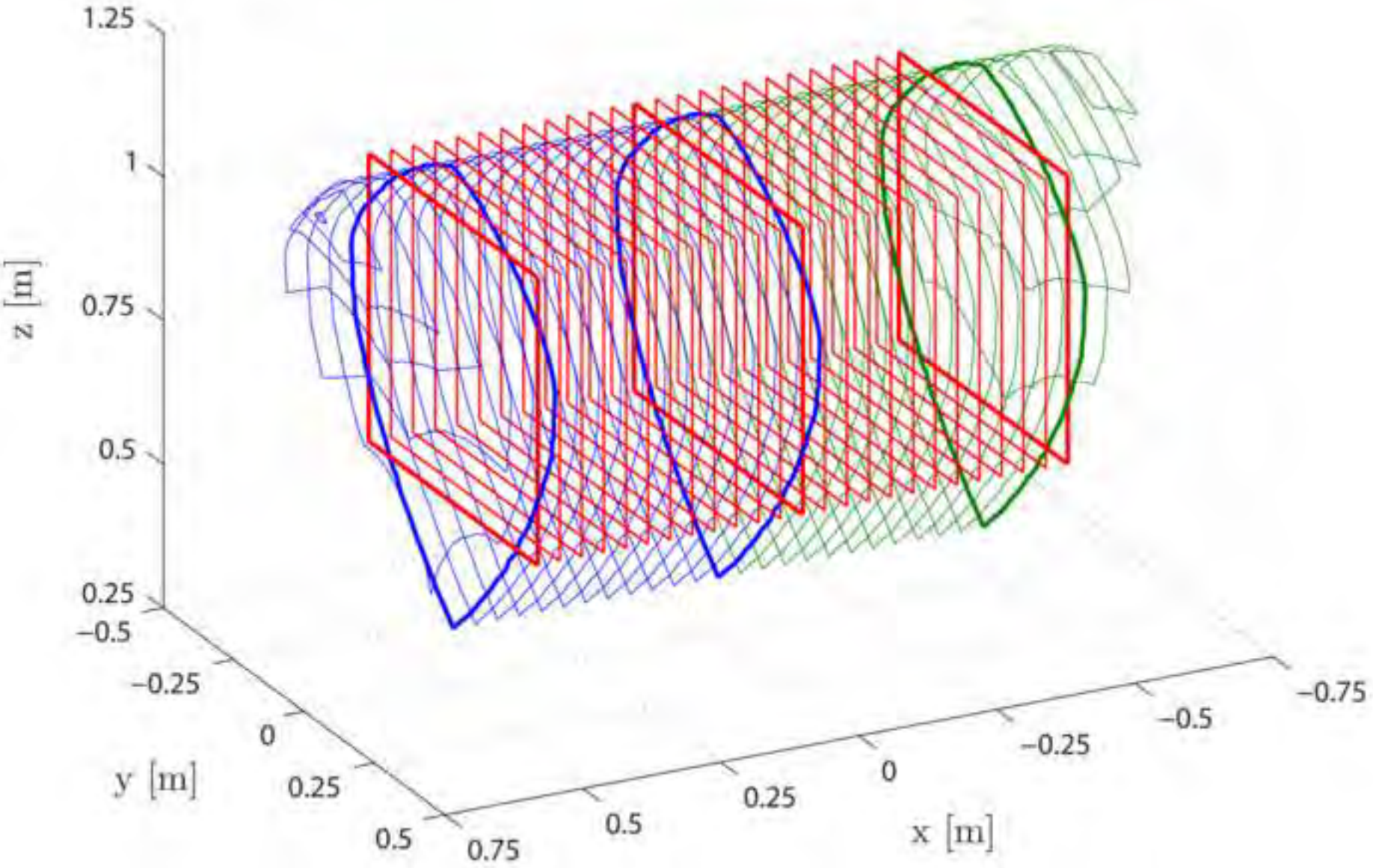

Figure(s)

Click here to download high resolution image

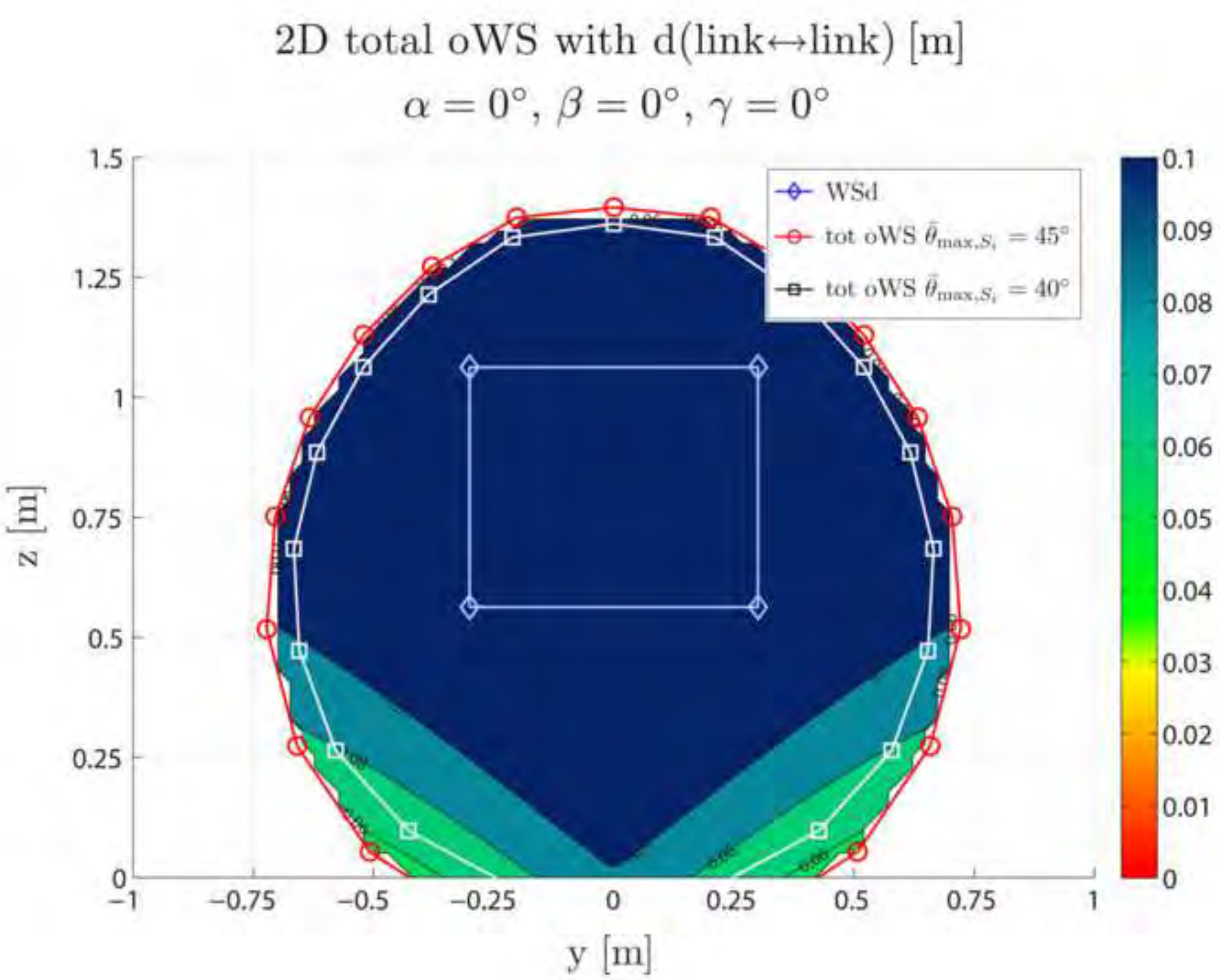

Figure(s)

Click here to download high resolution image

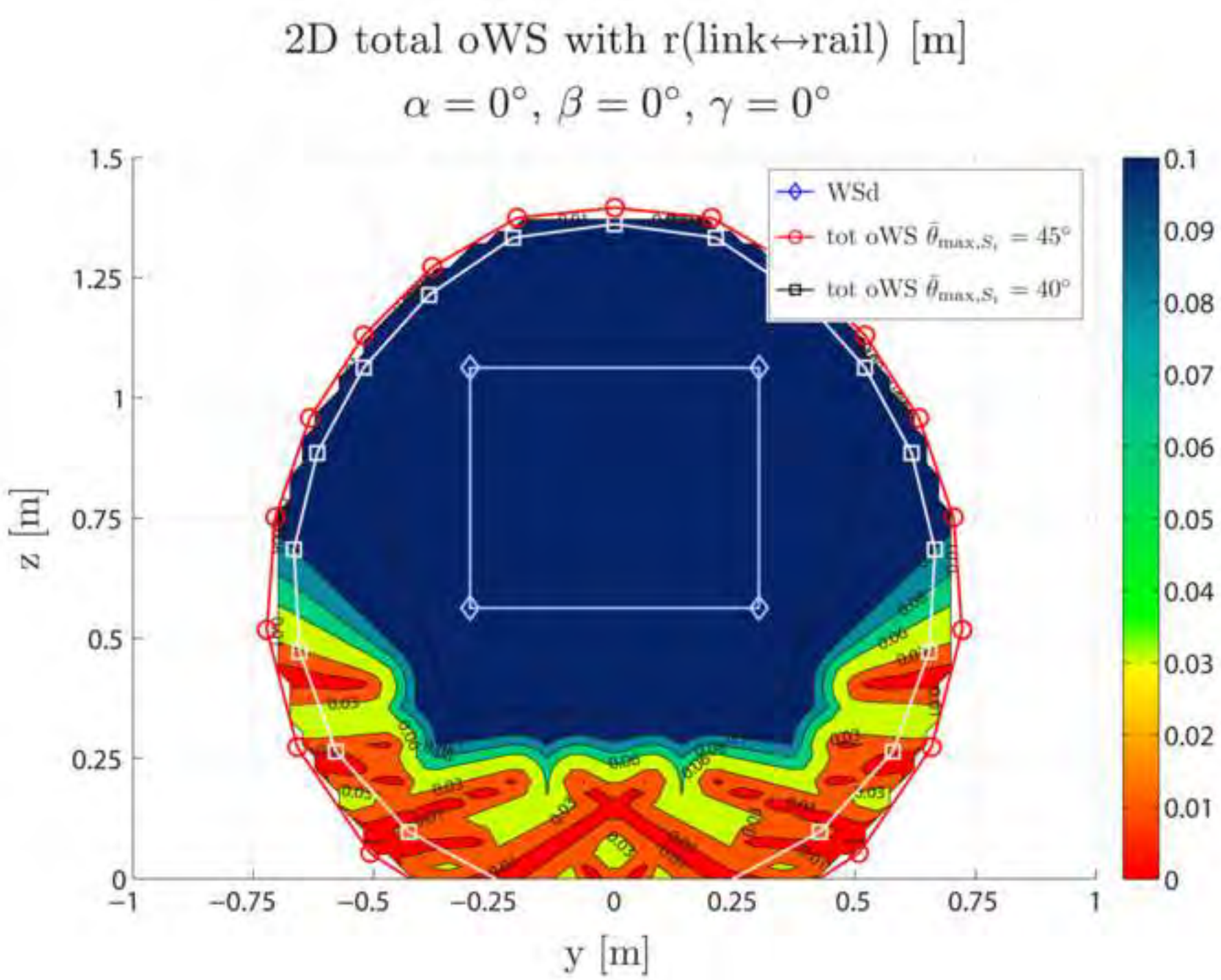

Figure(s)

Click here to download high resolution image

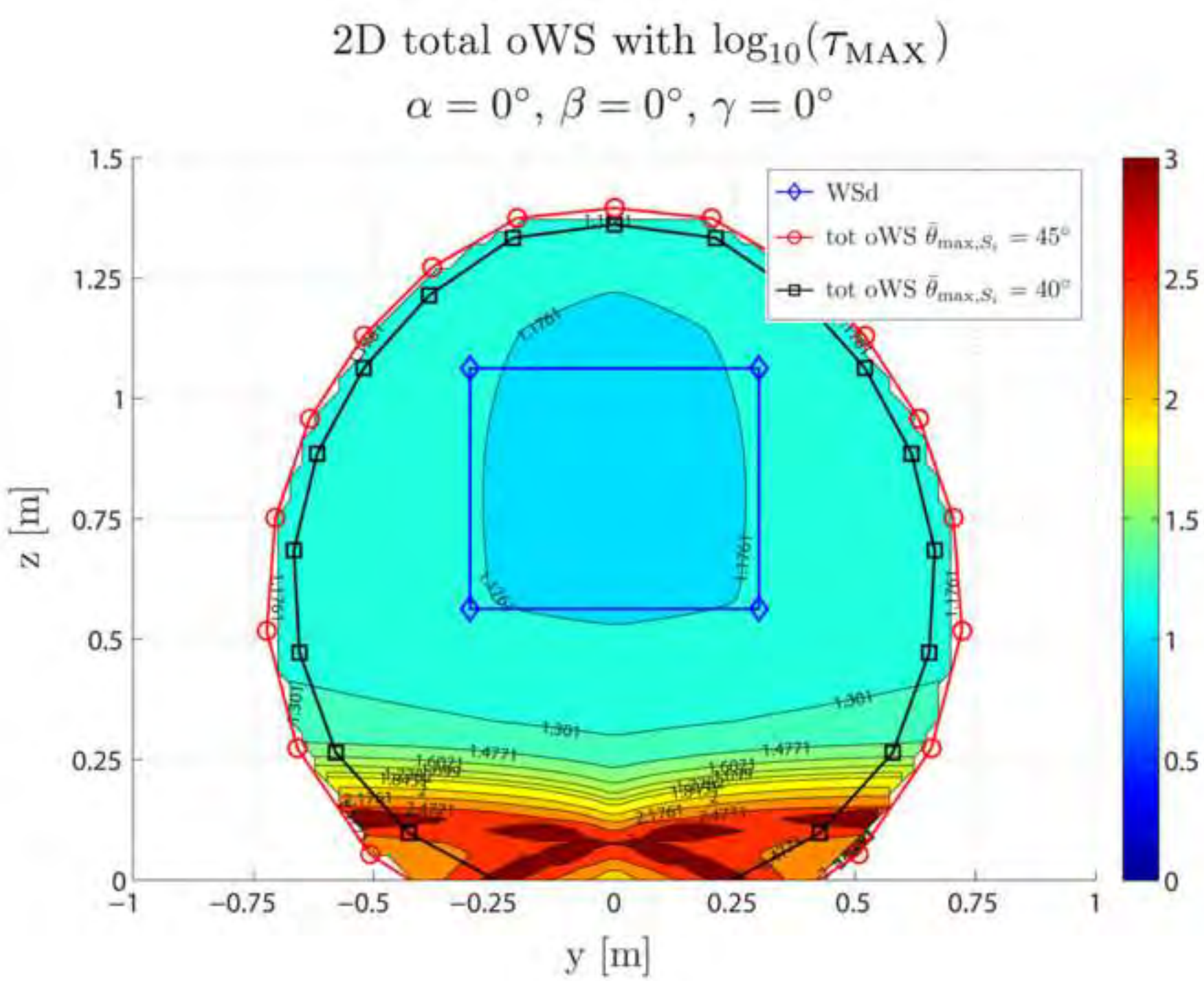

Figure(s)
Click here to download high resolution image

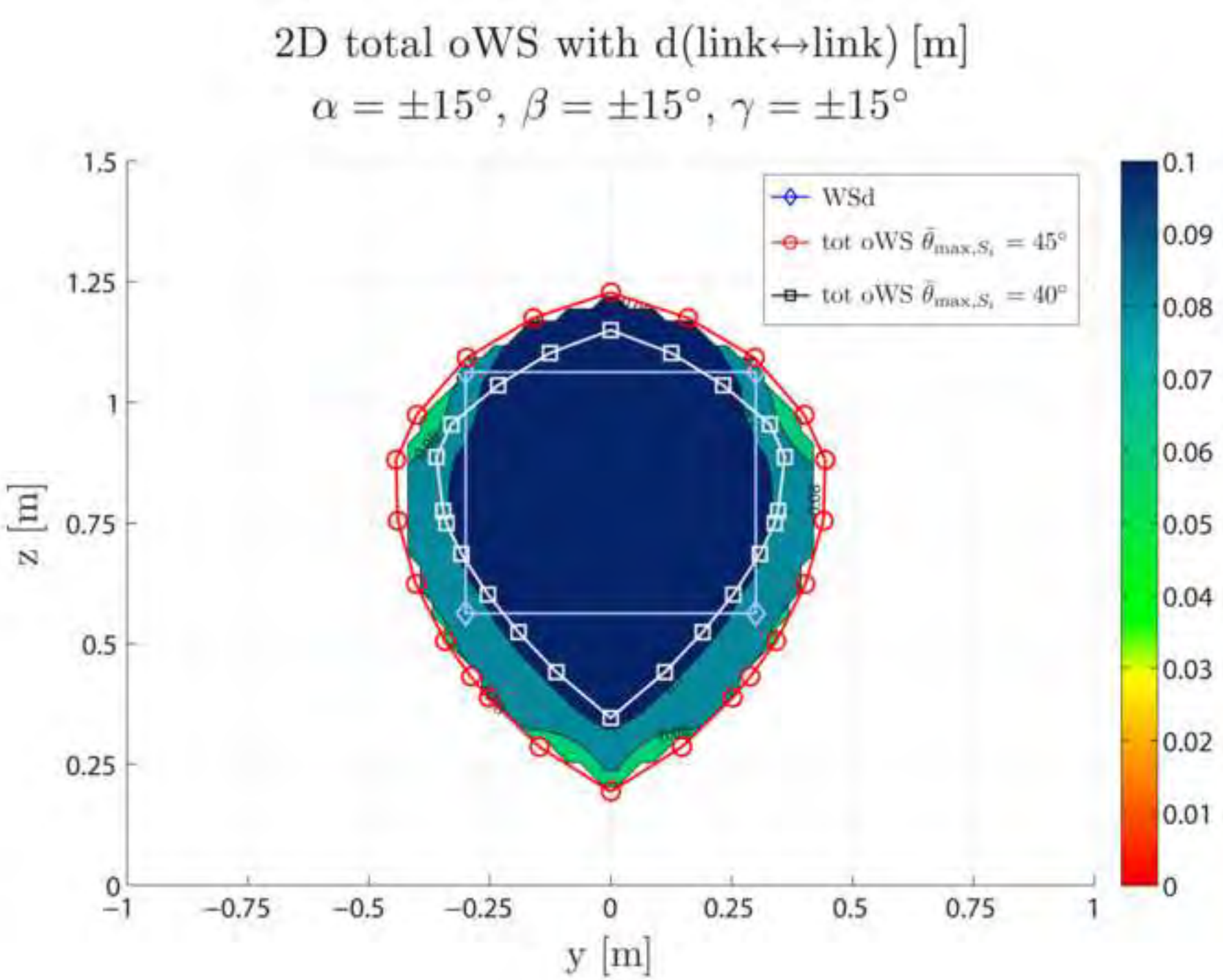

Figure(s)

Click here to download high resolution image

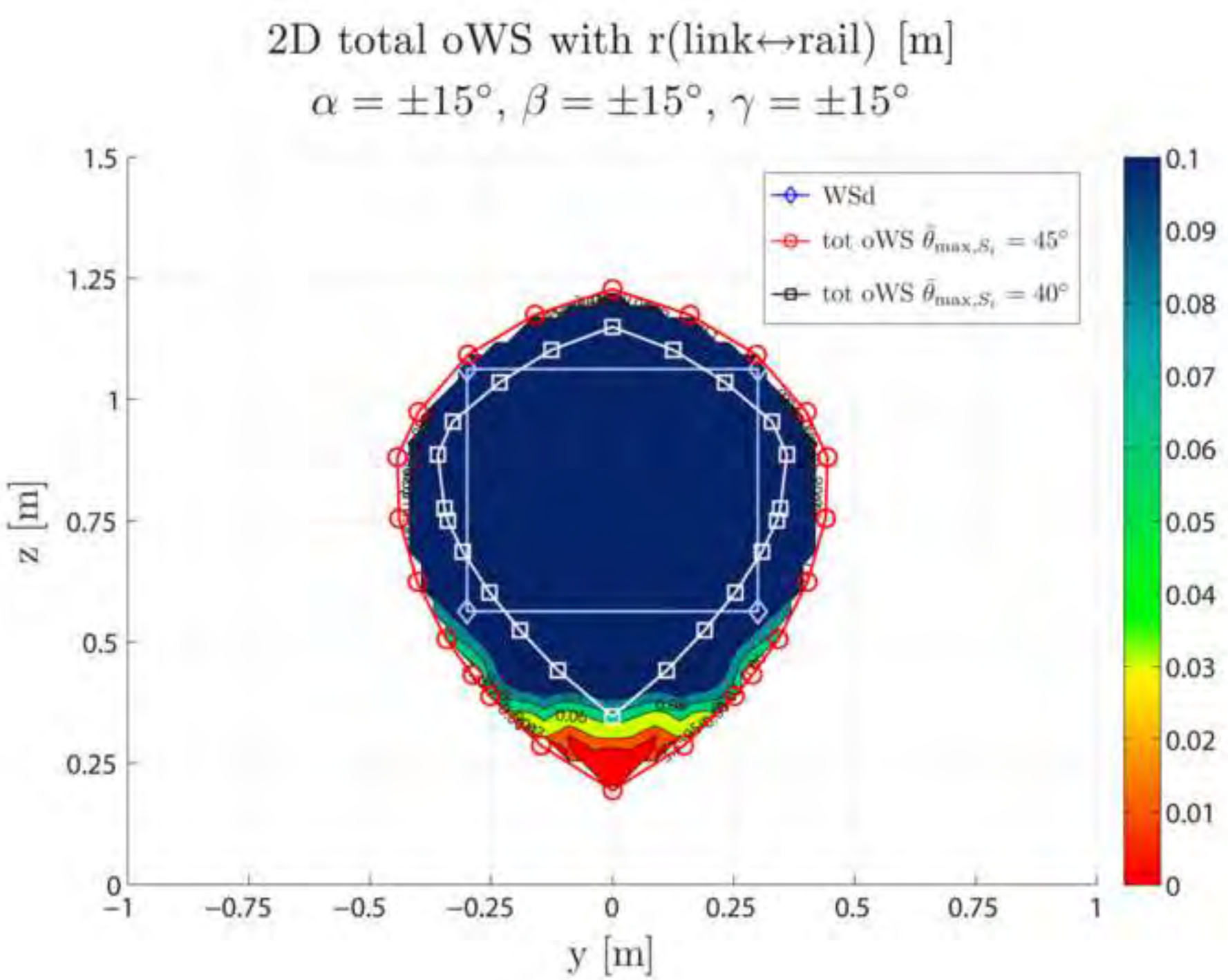

Figure(s)

Click here to download high resolution image

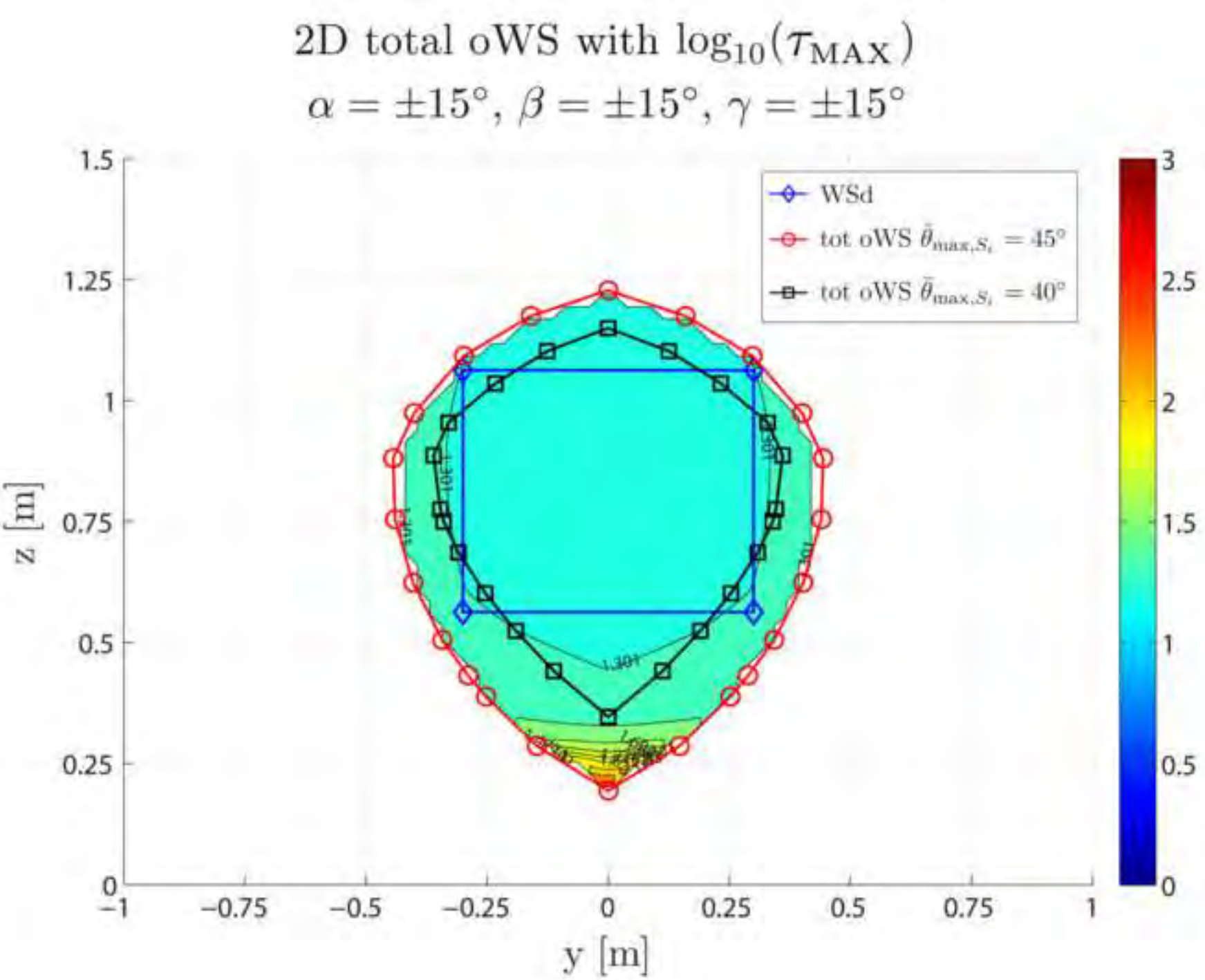

Figure(s)

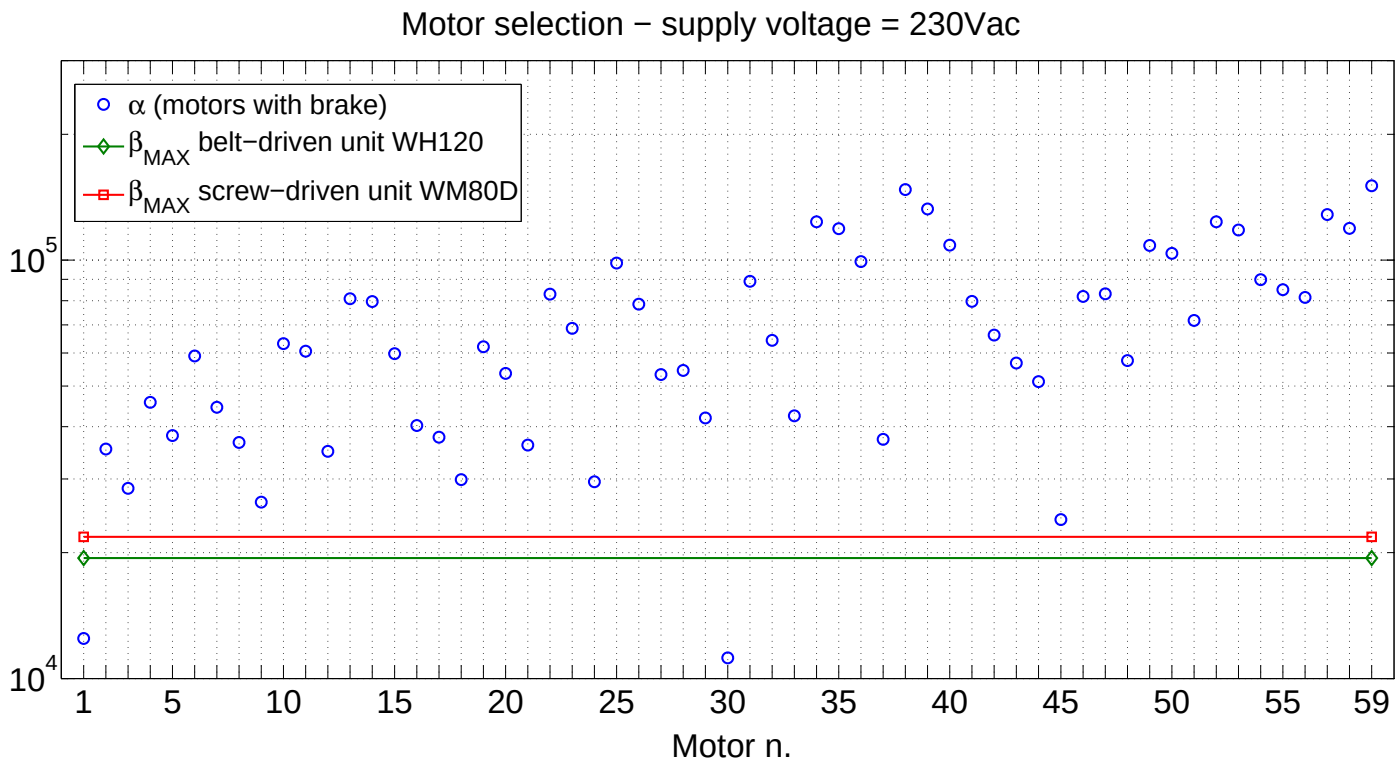
Motor selection − supply voltage = 230Vac
α (motors with brake)
β_MAX belt−driven unit WH120
β_MAX screw−driven unit WM80D
10^5
10^4
1
5
10
15
20
25
30
35
40
45
50
55
59
Motor n.

Figure(s)

Click here to download high resolution image

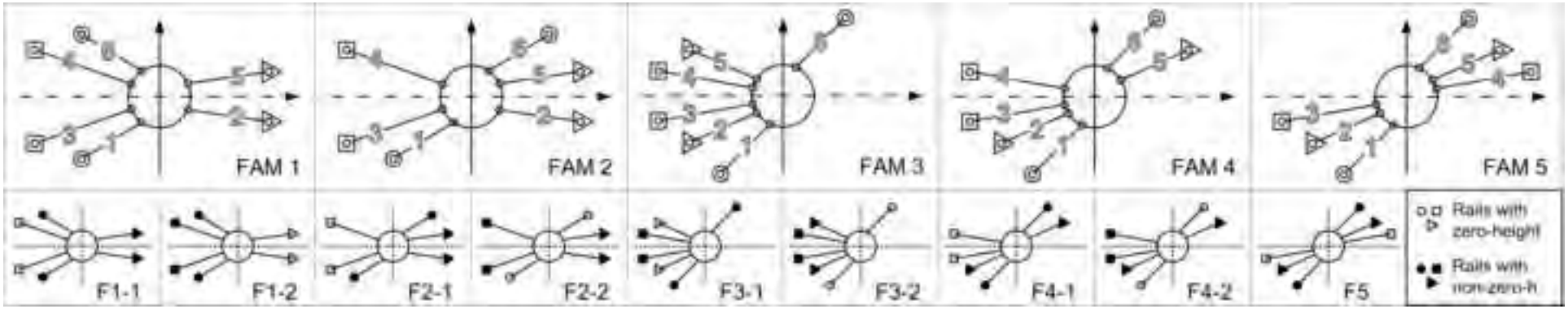

Figure(s)

Click here to download high resolution image

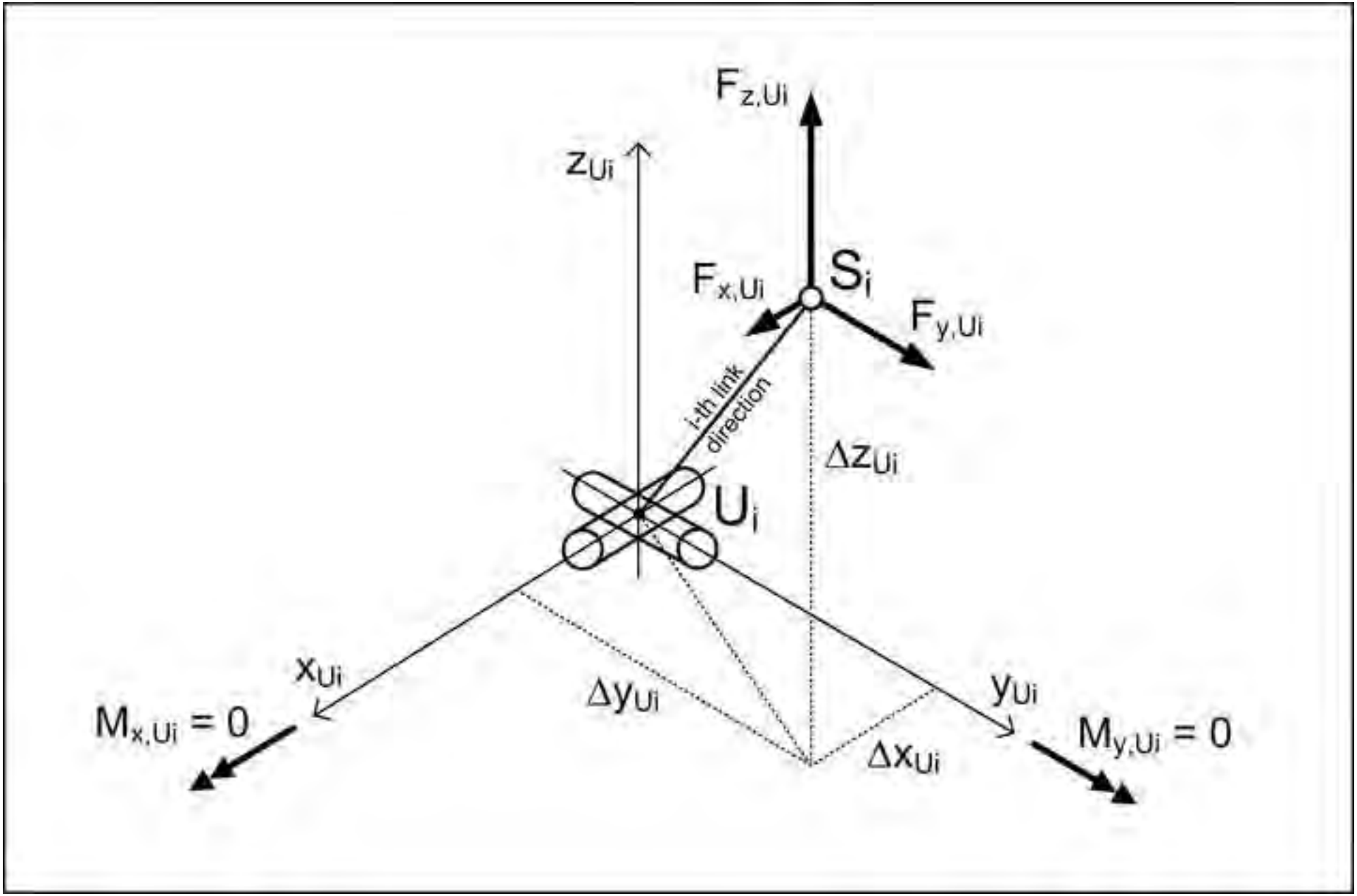

Figure(s)

Click here to download high resolution image

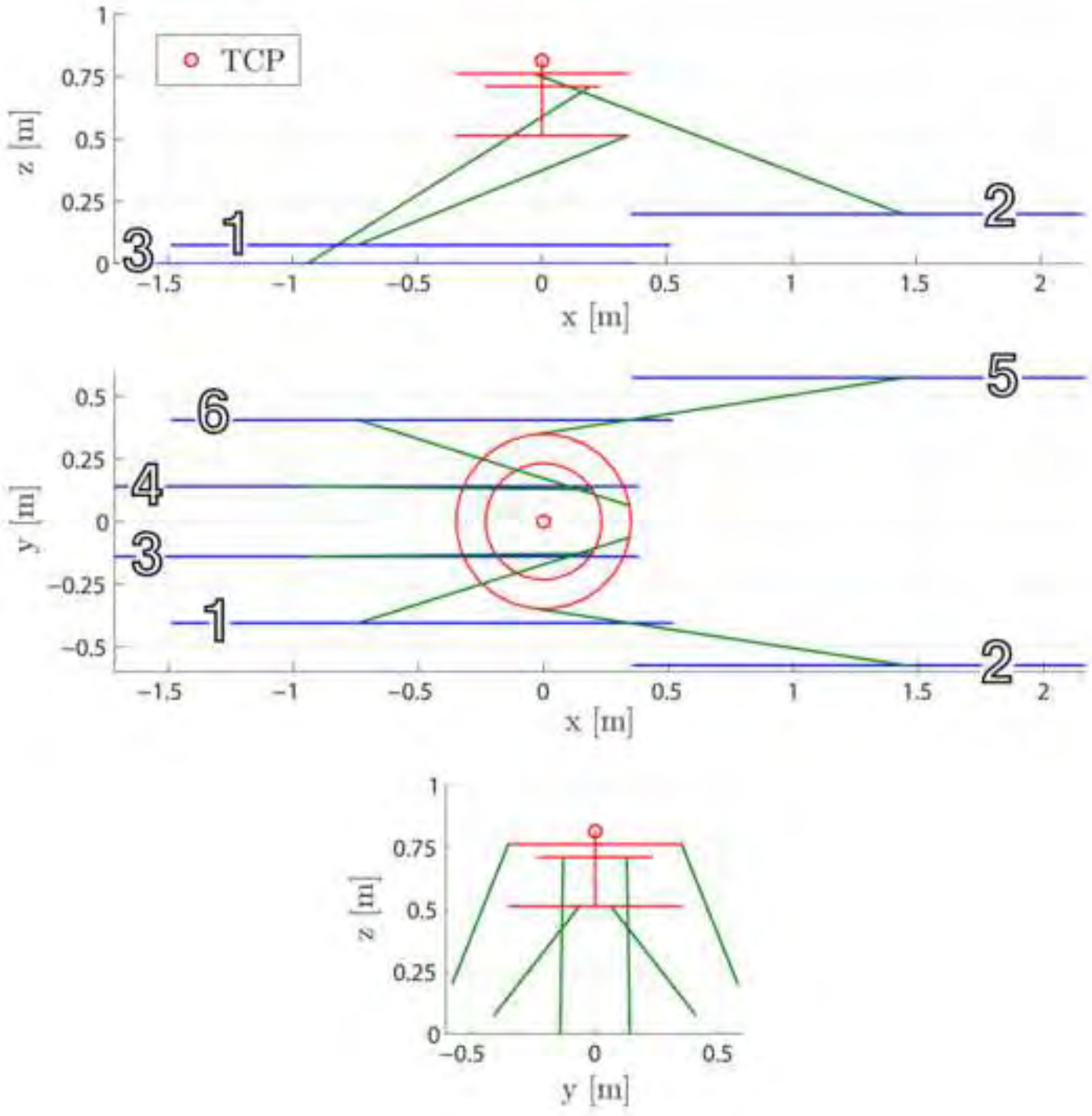

Figure(s)

Click here to download high resolution image

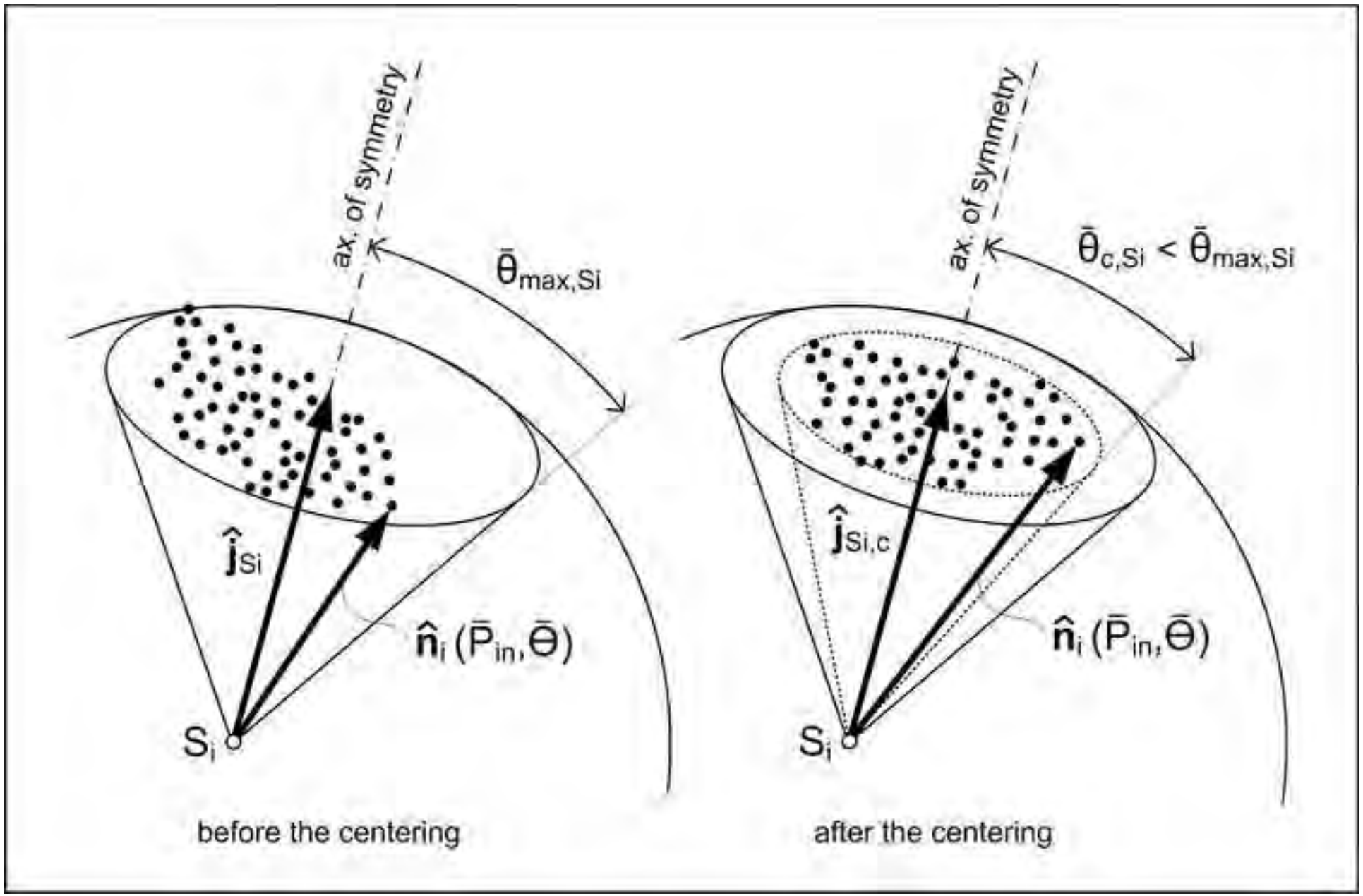

Figure(s)

Click here to download high resolution image

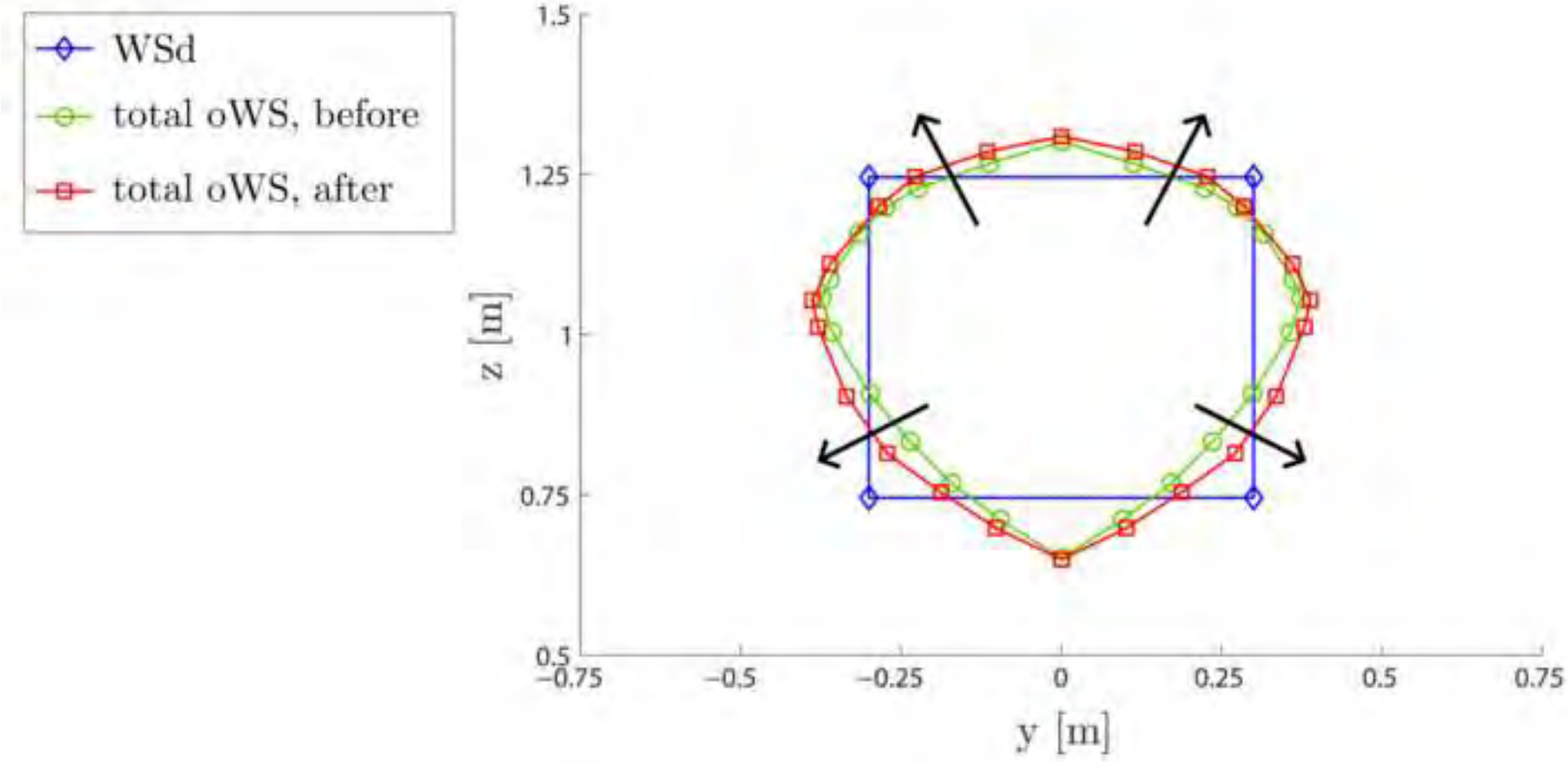

Figure(s)
Click here to download high resolution image

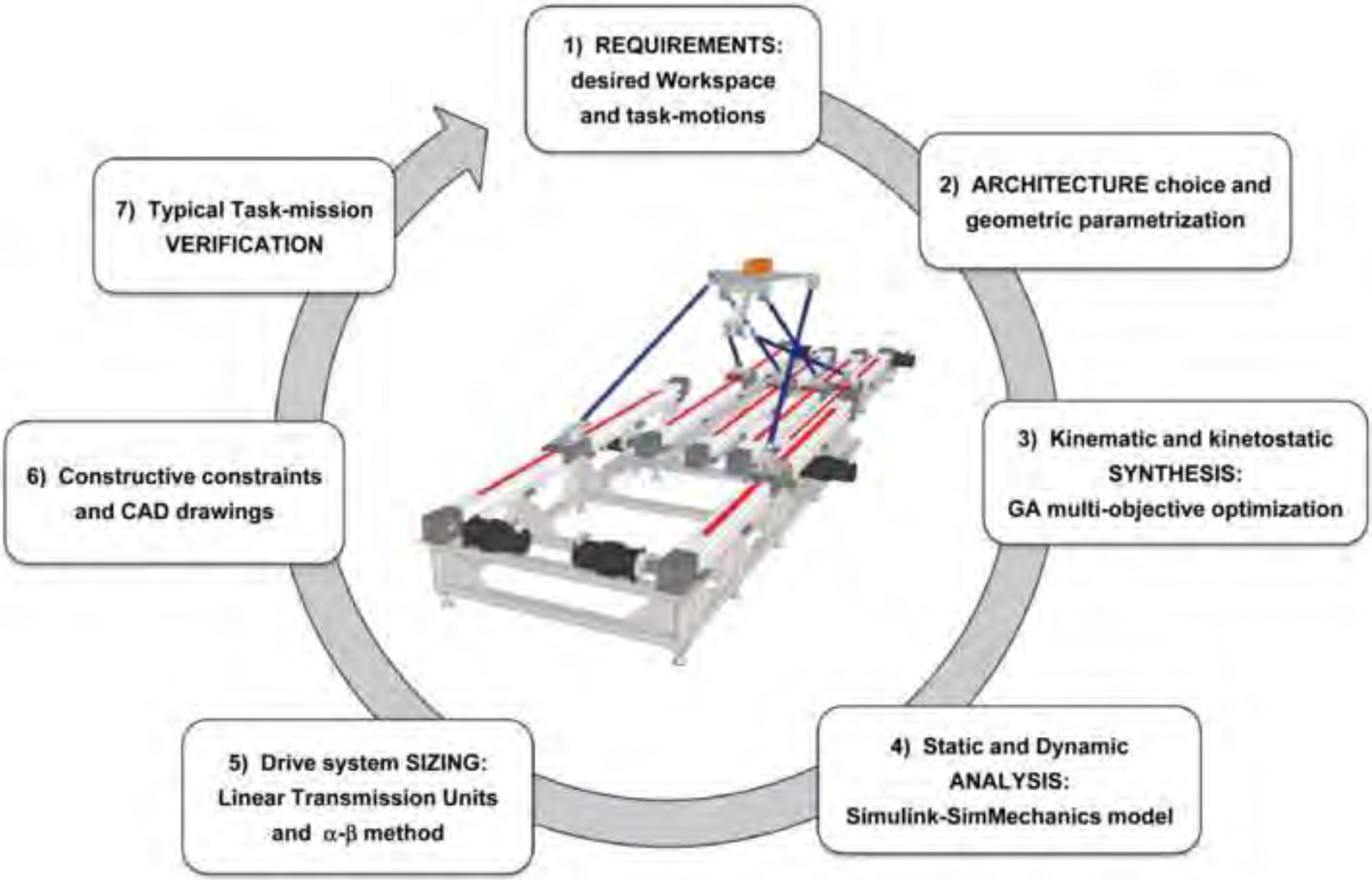

Figure(s)

Click here to download high resolution image

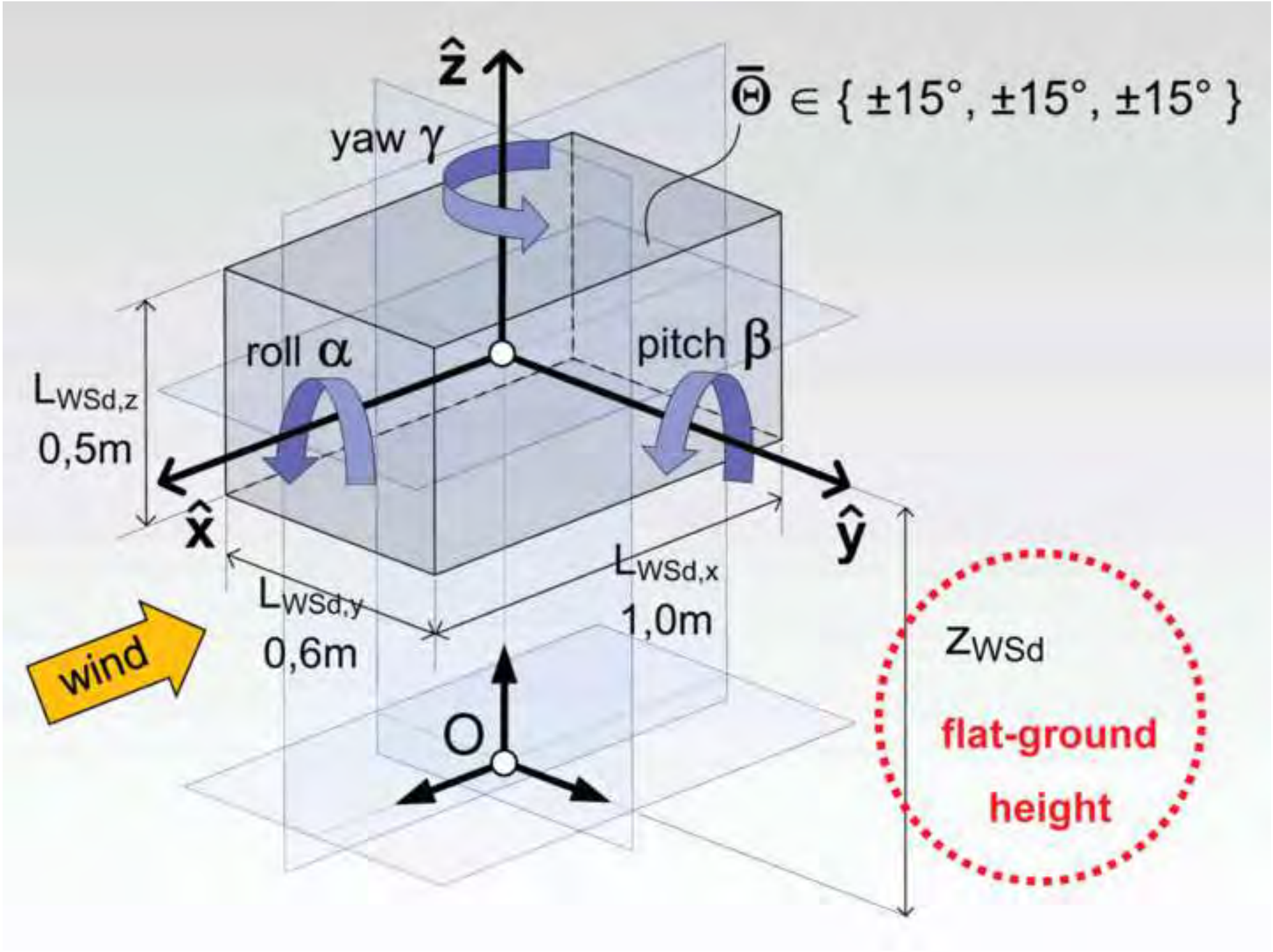

Figure(s)

Click here to download high resolution image

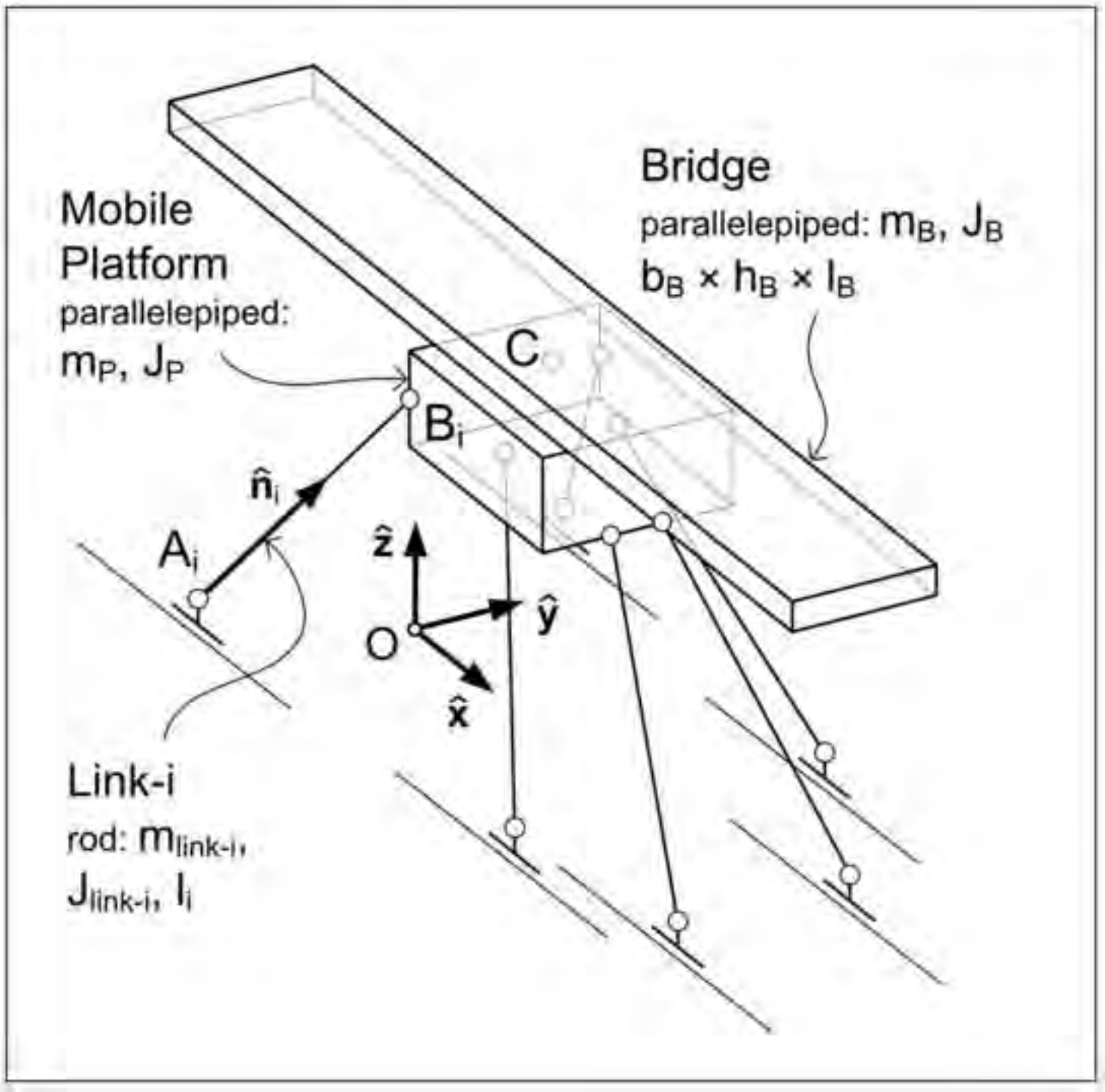

Figure(s)

Click here to download high resolution image

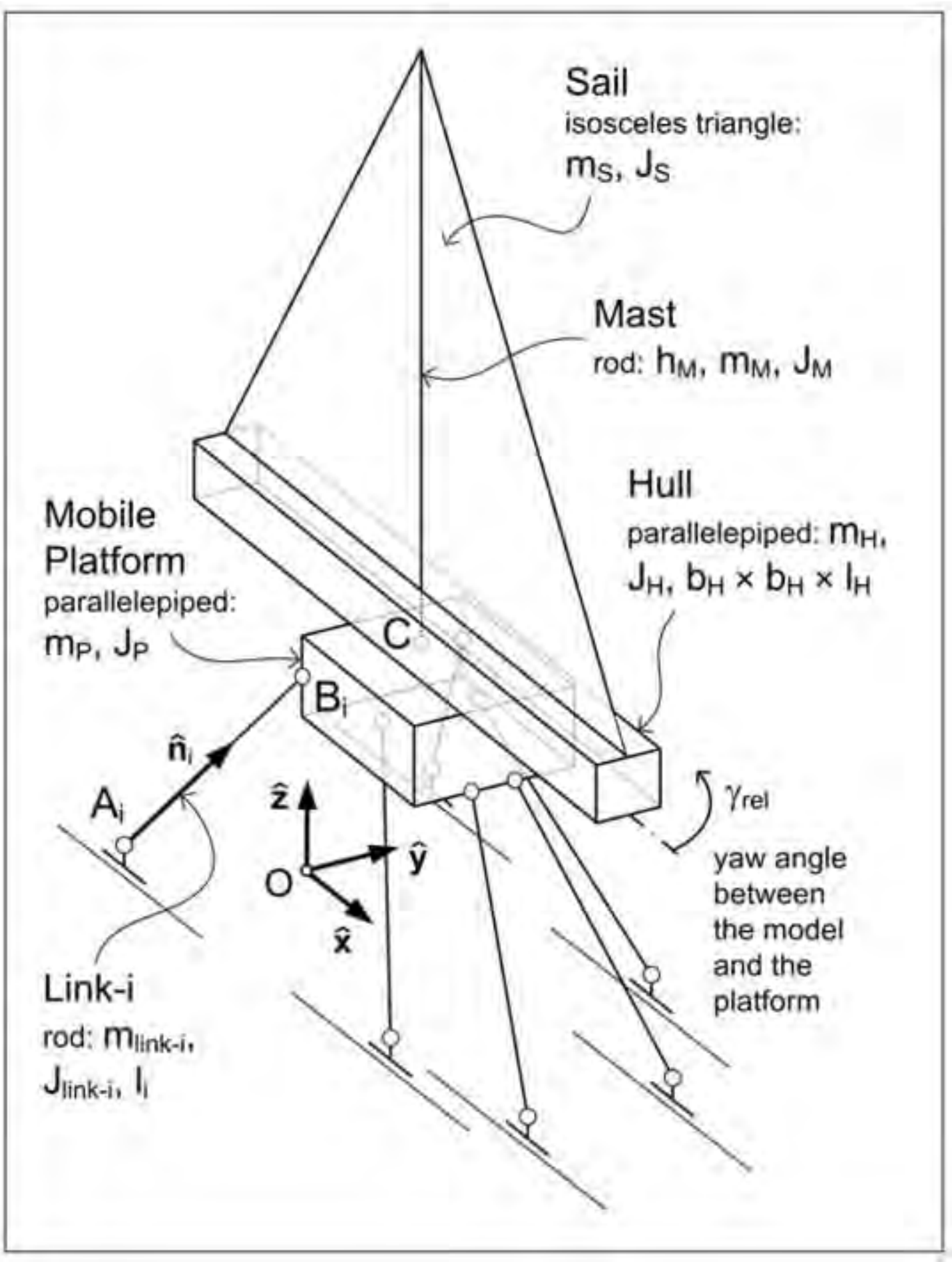

Figure(s)

Click here to download high resolution image

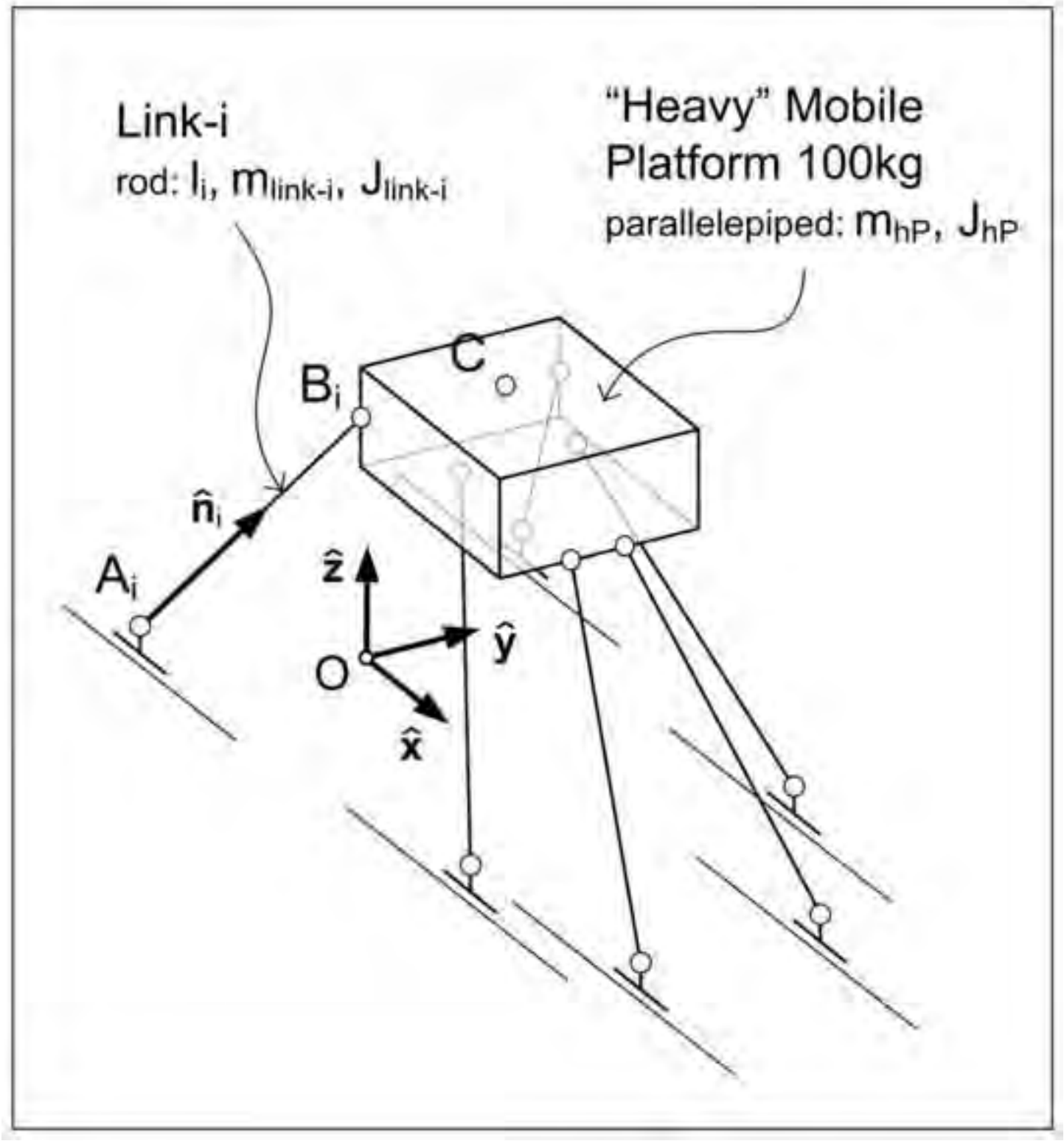

Figure(s)

Click here to download high resolution image

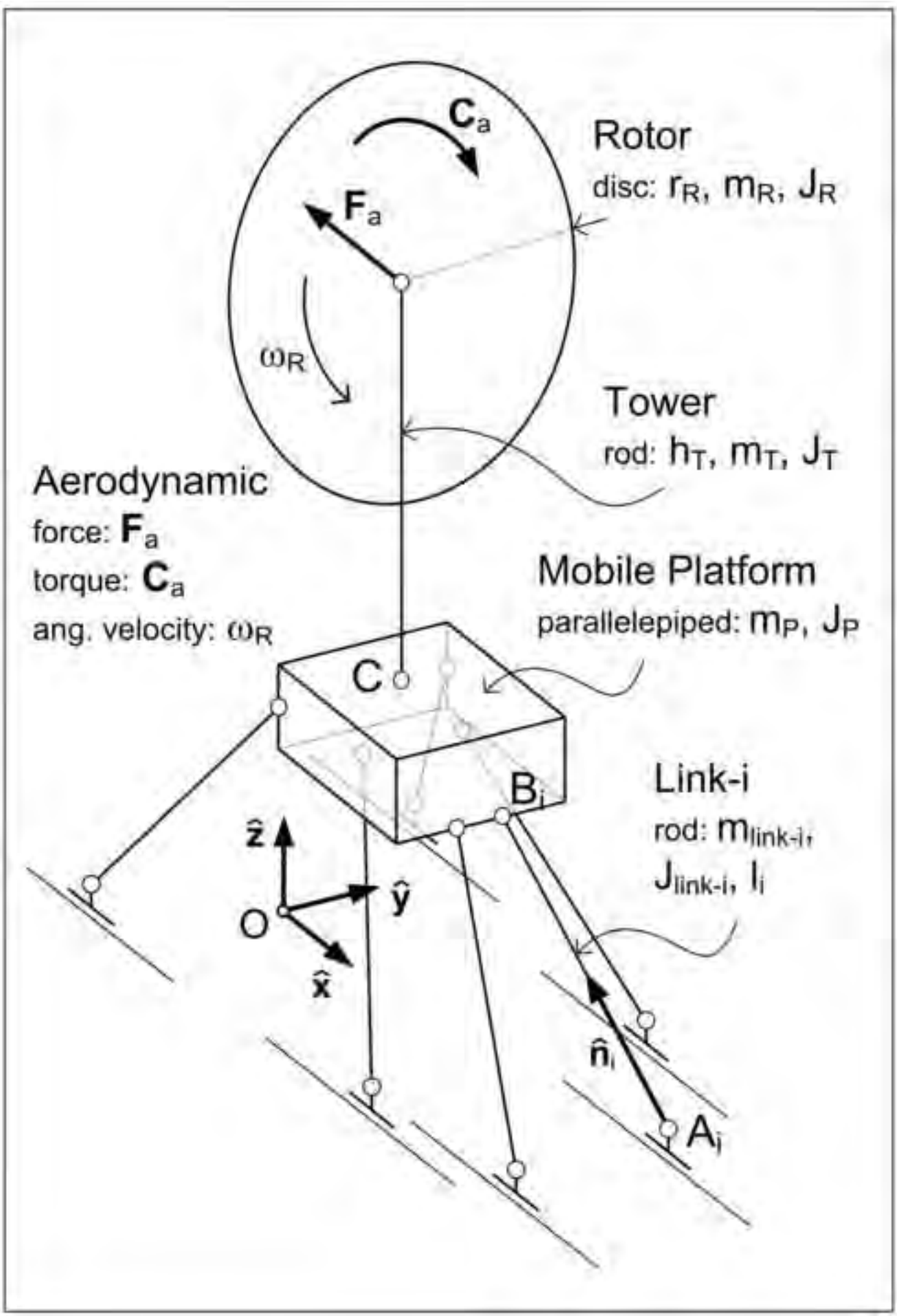

Figure(s)

Click here to download high resolution image

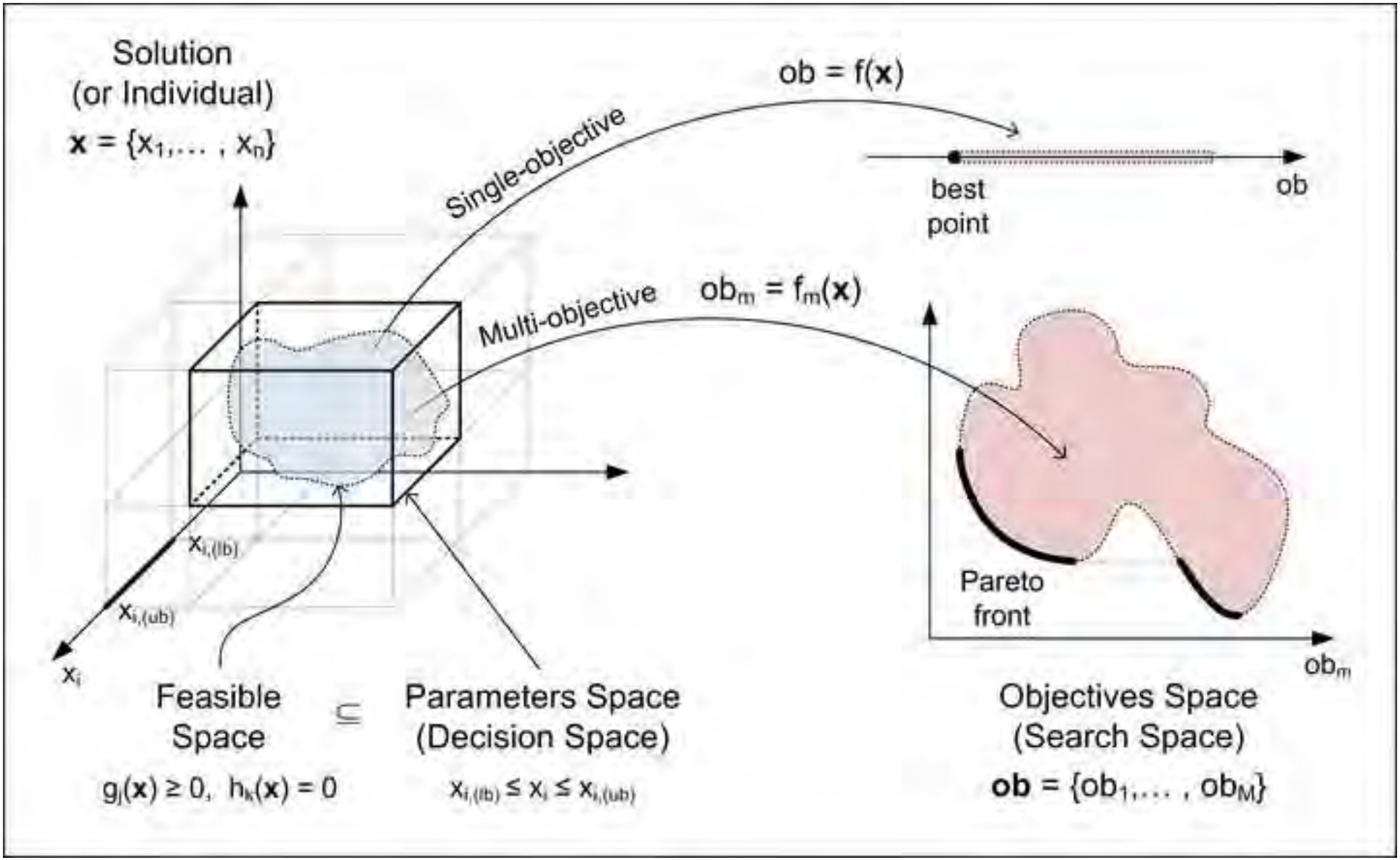

Figure(s)

Click here to download high resolution image

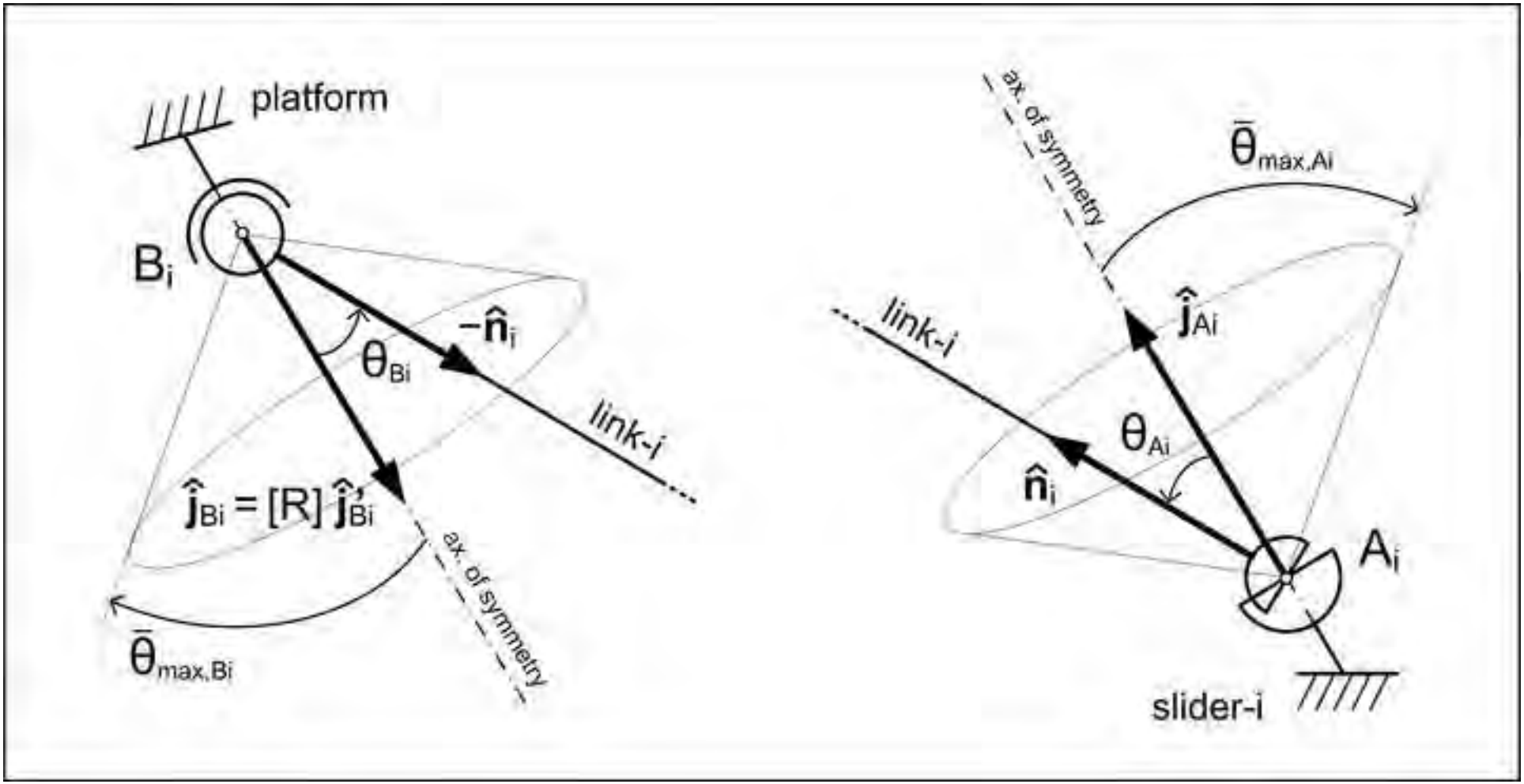

Figure(s)

Click here to download high resolution image

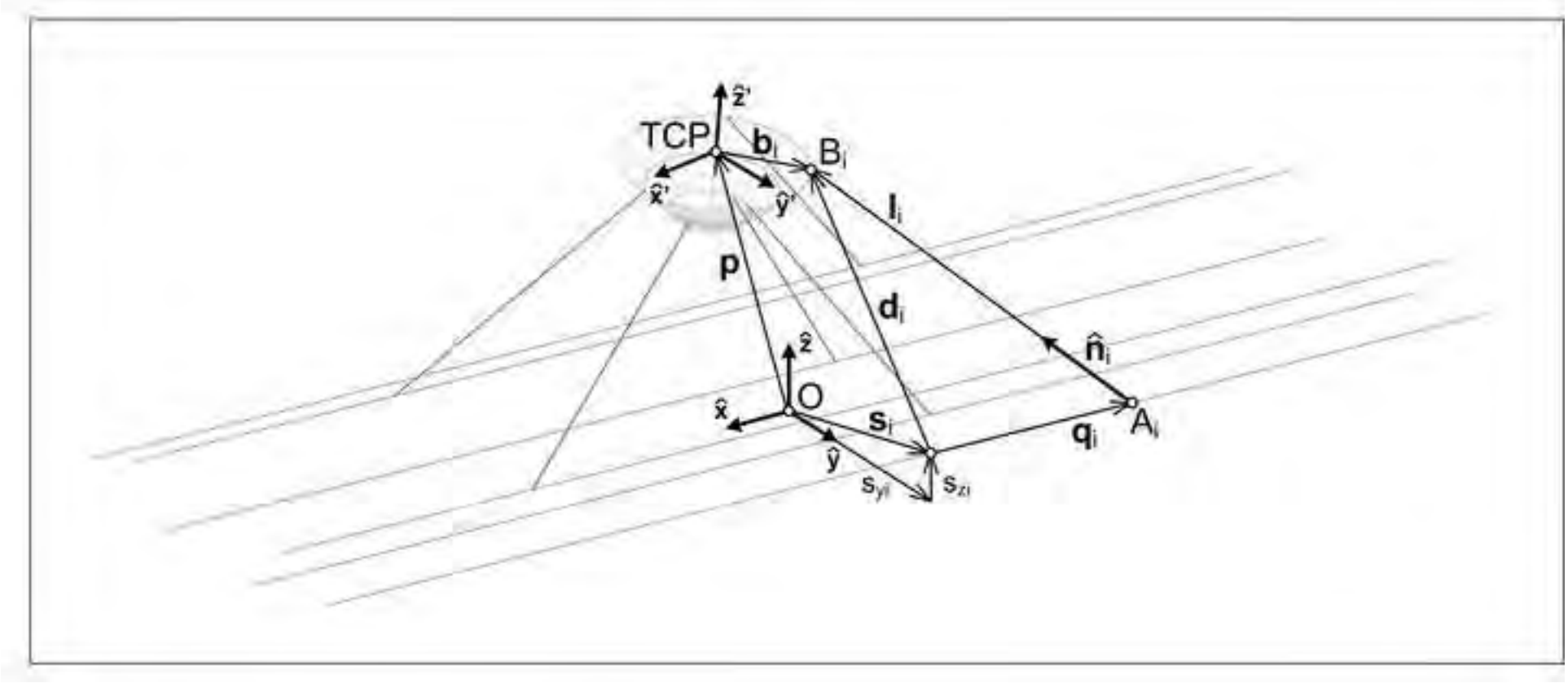

Figure(s)

Click here to download high resolution image

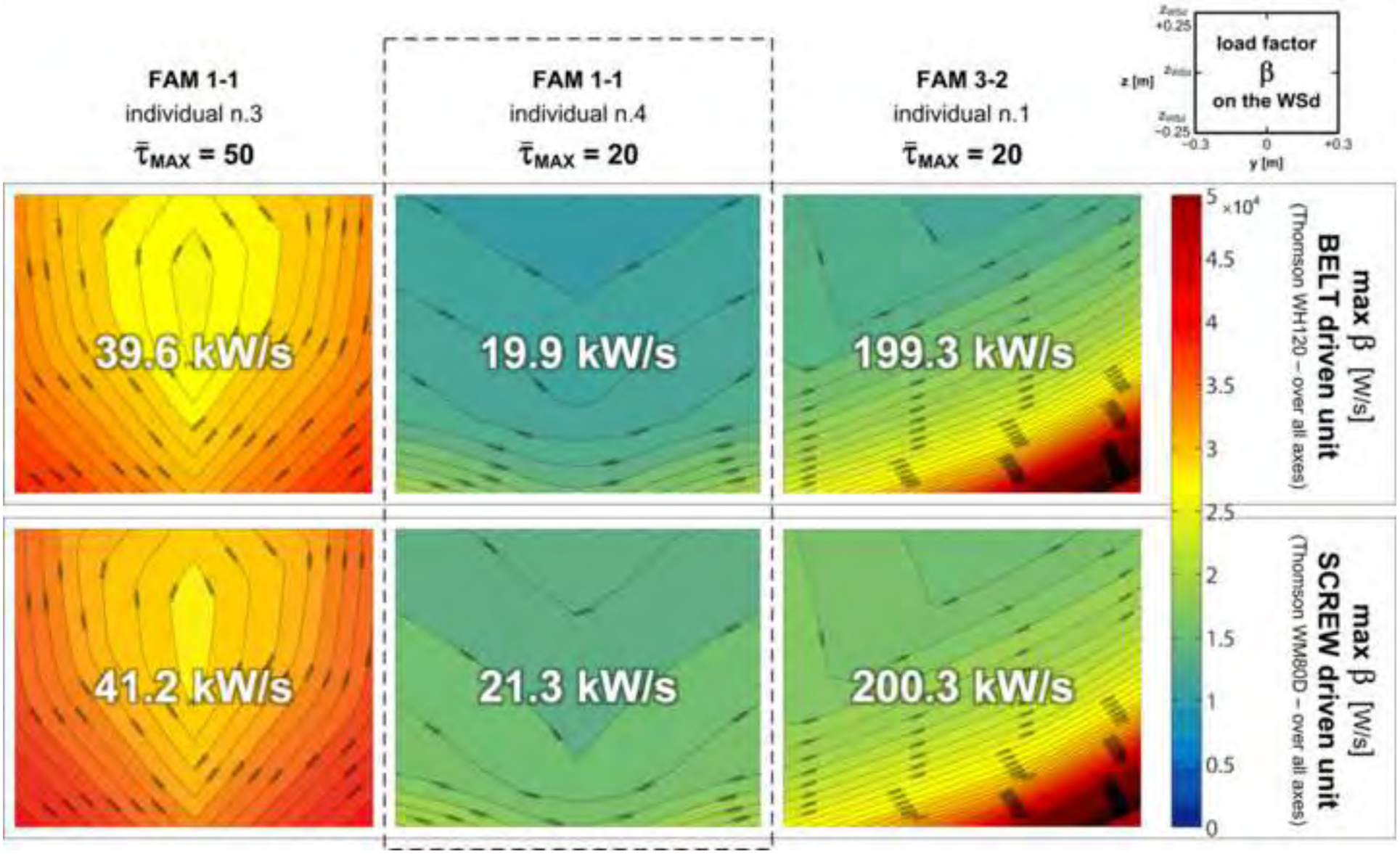

Figure(s)

Click here to download high resolution image

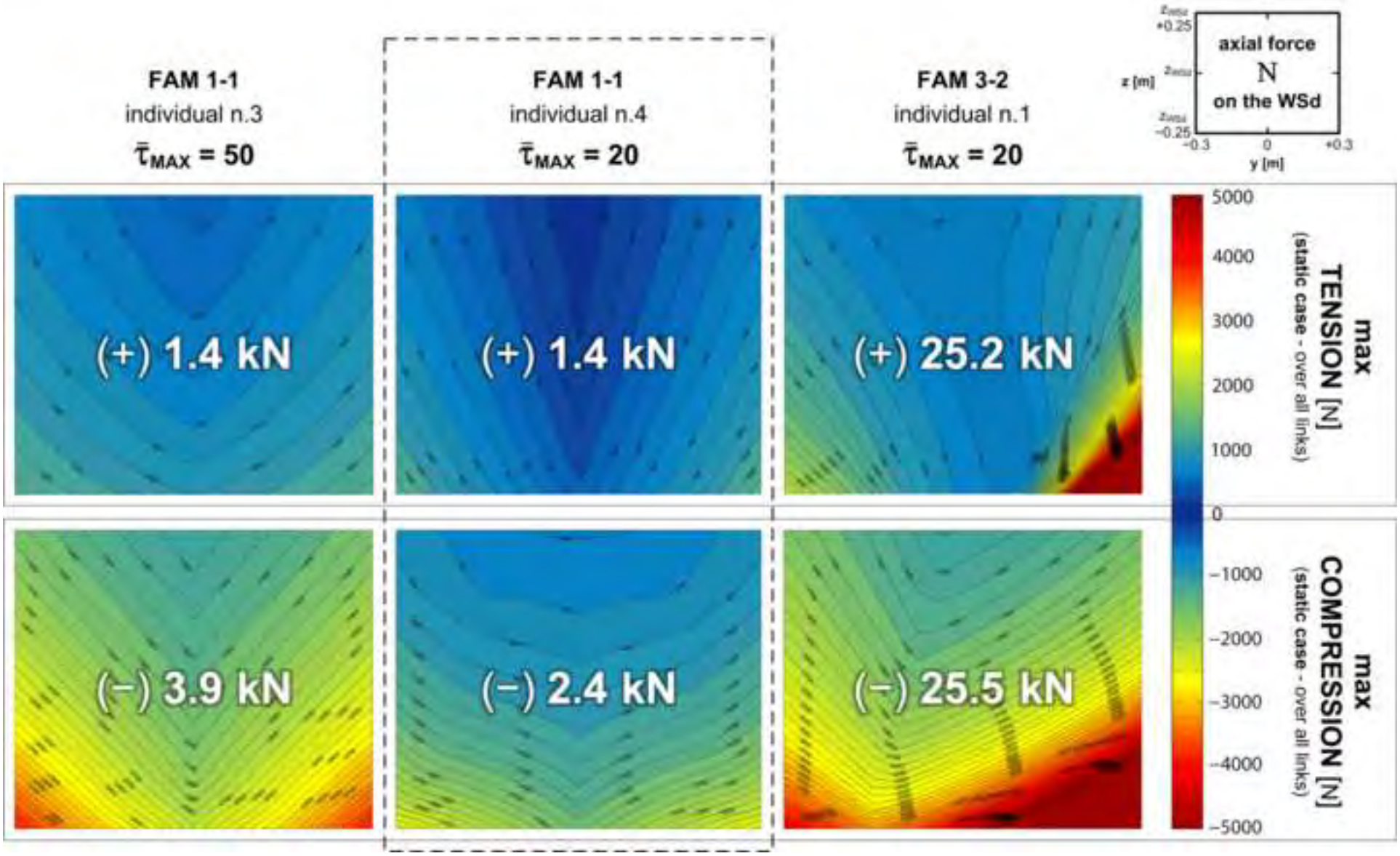

Figure(s)

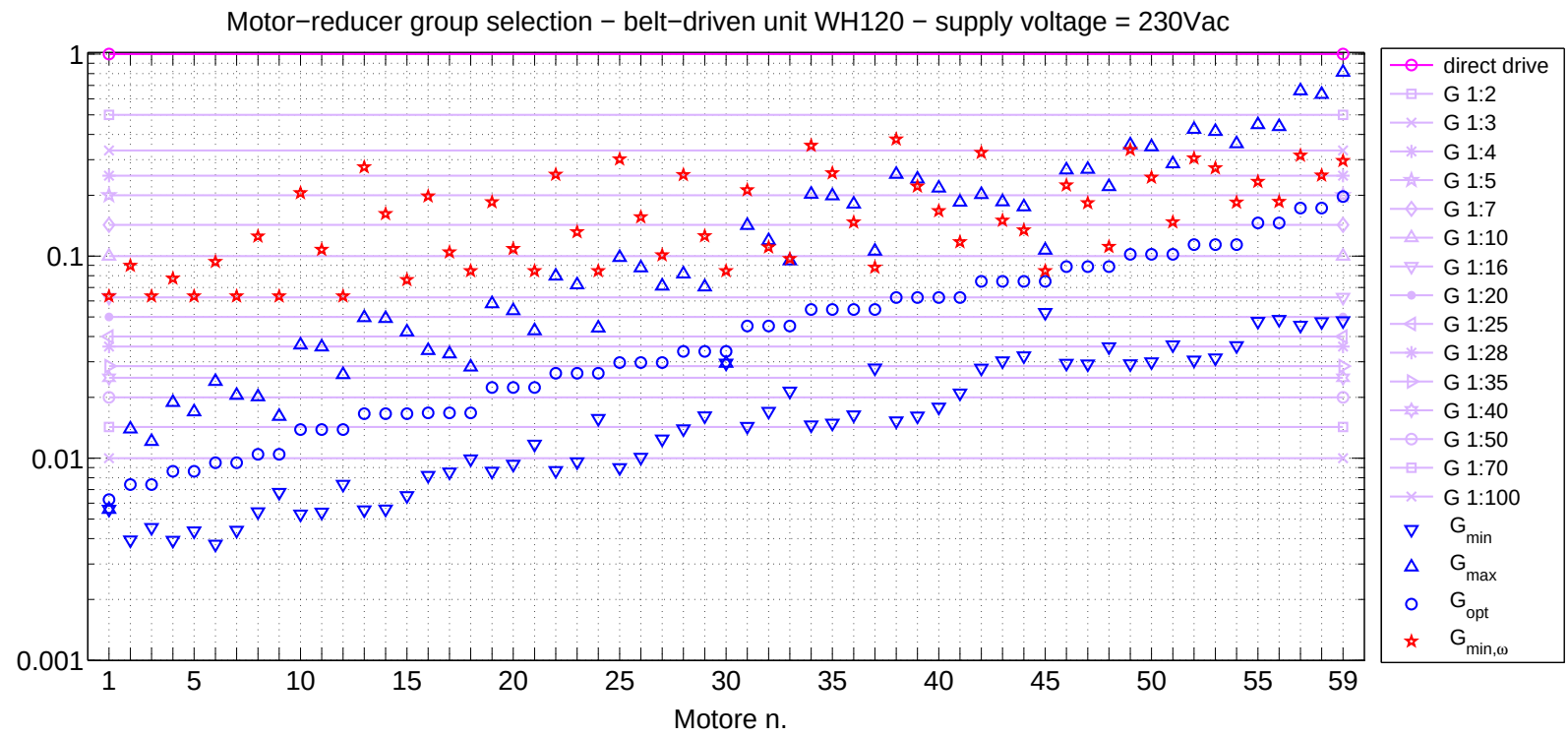
Motor−reducer group selection − belt−driven unit WH120 − supply voltage = 230Vac
1
0.1
0.01
0.001
1
5
10
15
20
25
30
35
40
45
50
55
59
Motore n.
direct drive
G 1:2
G 1:3
G 1:4
G 1:5
G 1:7
G 1:10
G 1:16
G 1:20
G 1:25
G 1:28
G 1:35
G 1:40
G 1:50
G 1:70
G 1:100
G min
G max
G opt
G min,ω

Figure(s)

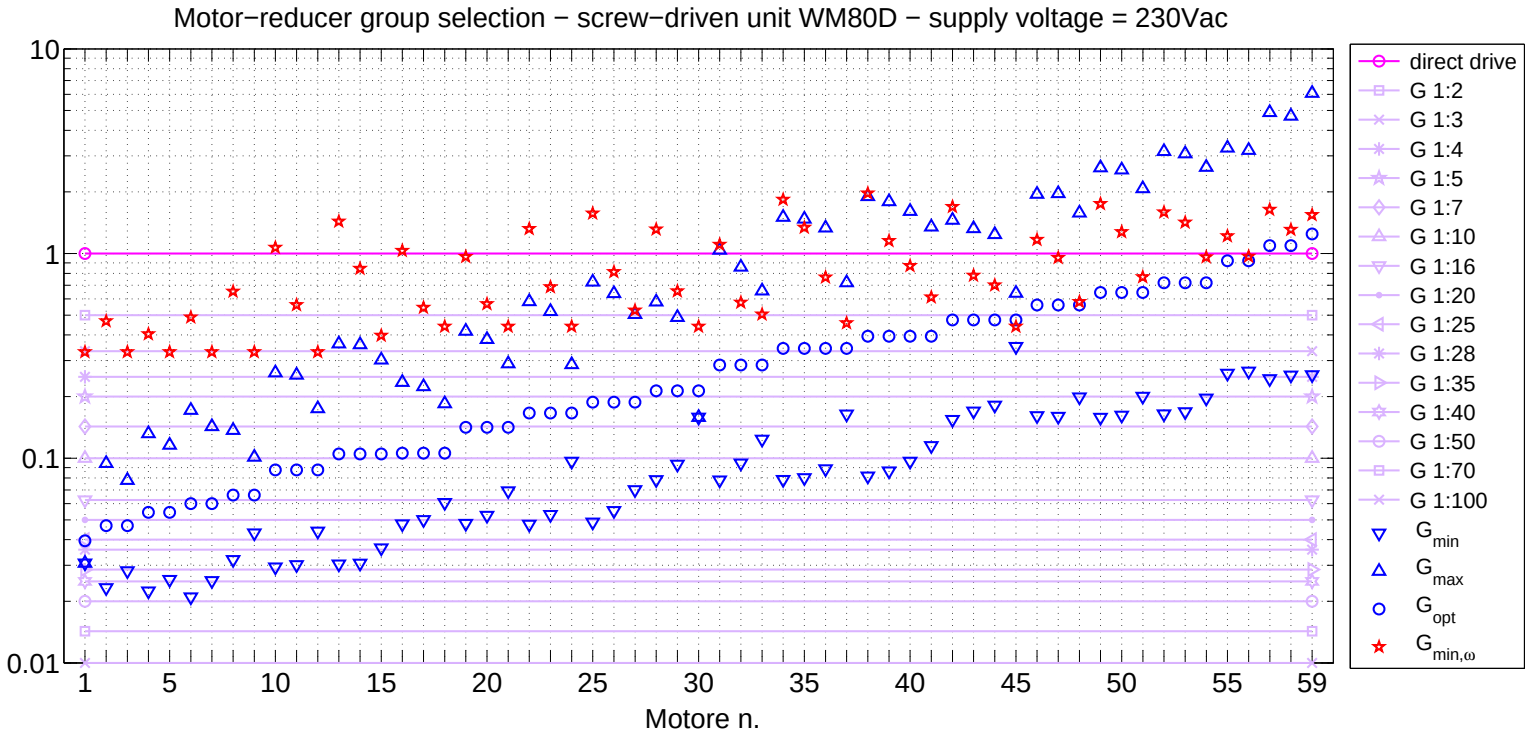
Motor−reducer group selection − screw−driven unit WM80D − supply voltage = 230Vac
10
1
0.1
0.01
1
5
10
15
20
25
30
35
40
45
50
55
59
Motore n.
direct drive
G 1:2
G 1:3
G 1:4
G 1:5
G 1:7
G 1:10
G 1:16
G 1:20
G 1:25
G 1:28
G 1:35
G 1:40
G 1:50
G 1:70
G 1:100
G min
G max
G opt
G min,ω

Figure(s)

Click here to download high resolution image

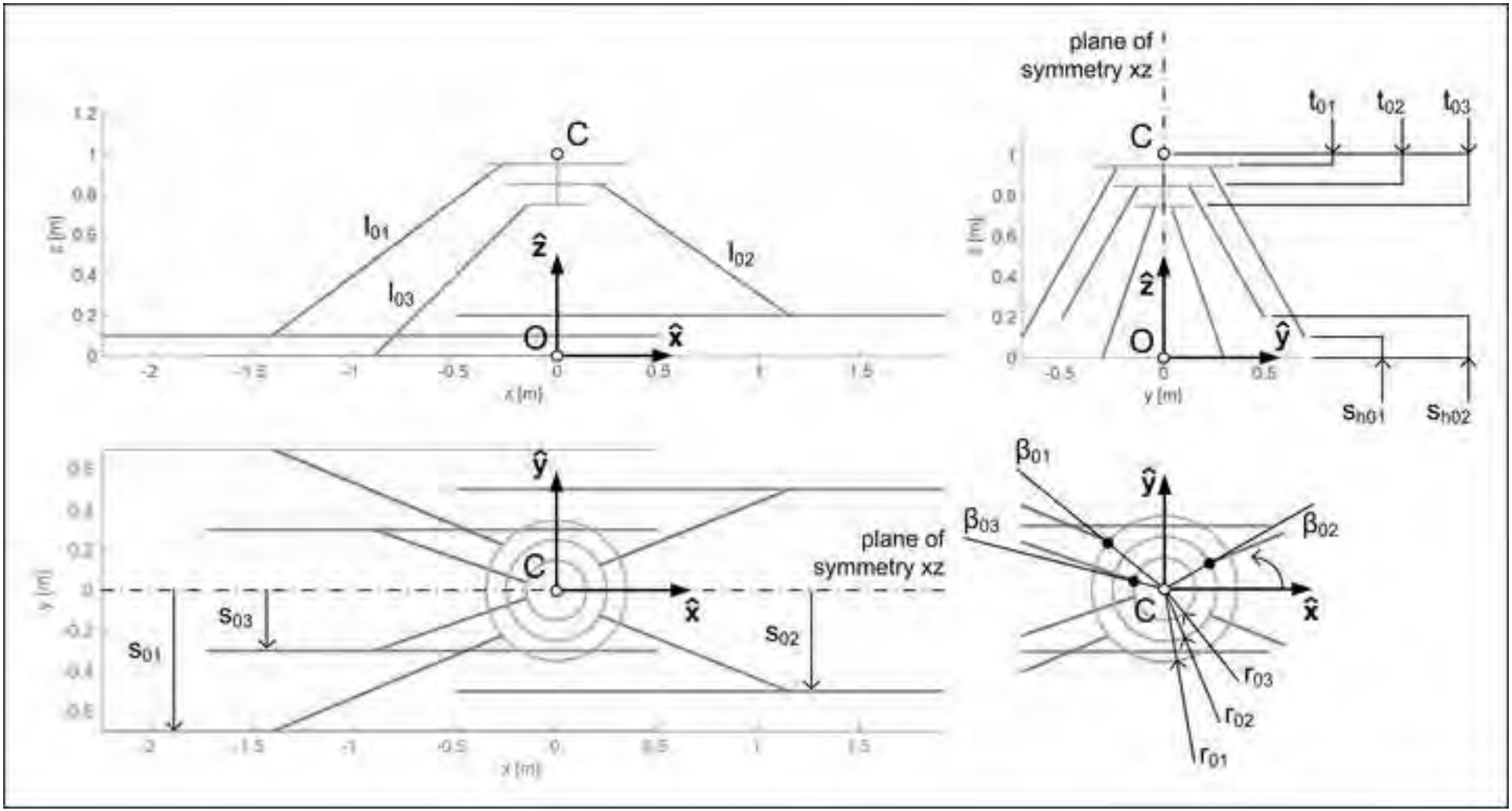

Figure(s)

Click here to download high resolution image

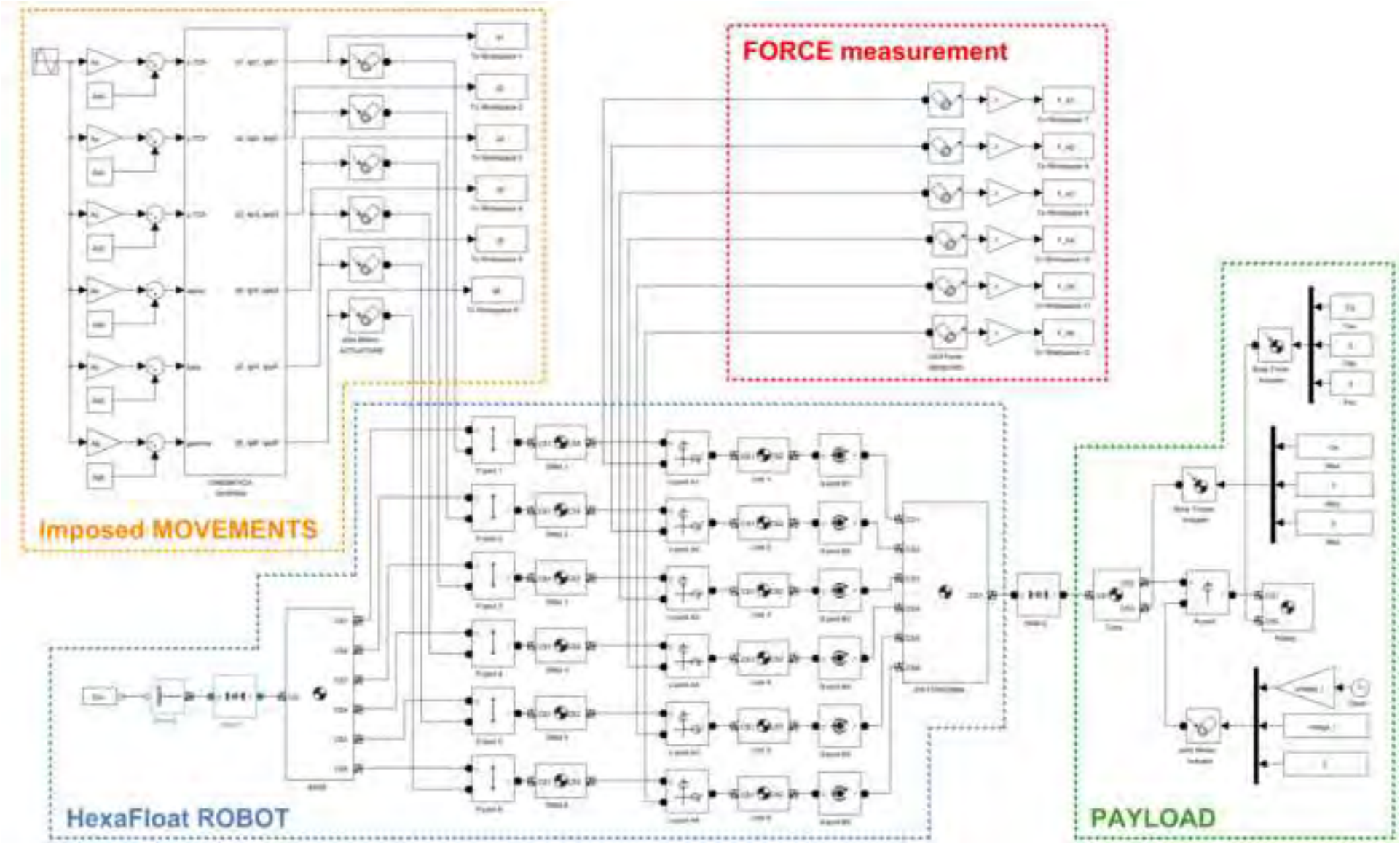

Figure(s)

Click here to download high resolution image

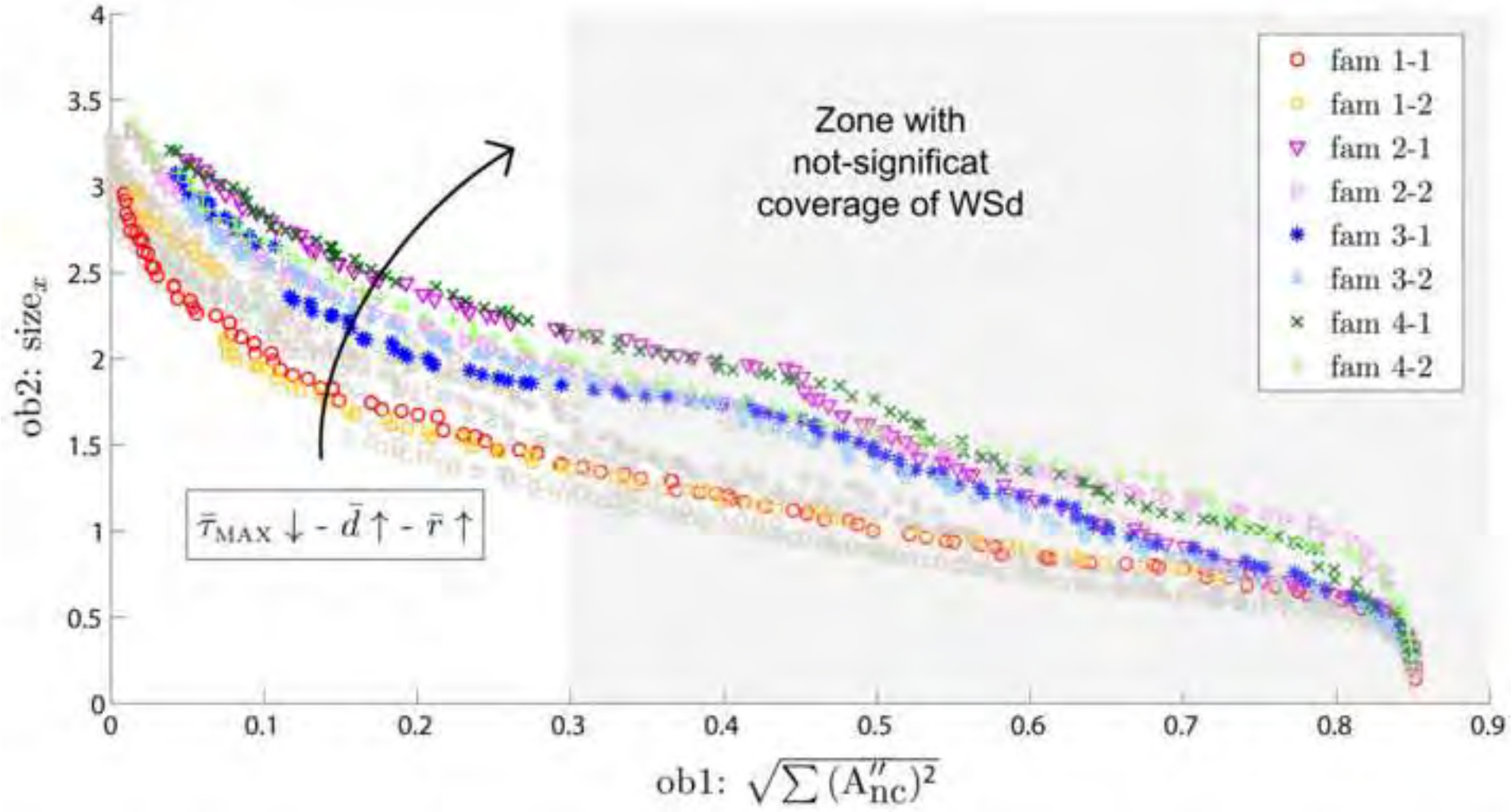

Figure(s)

Click here to download high resolution image

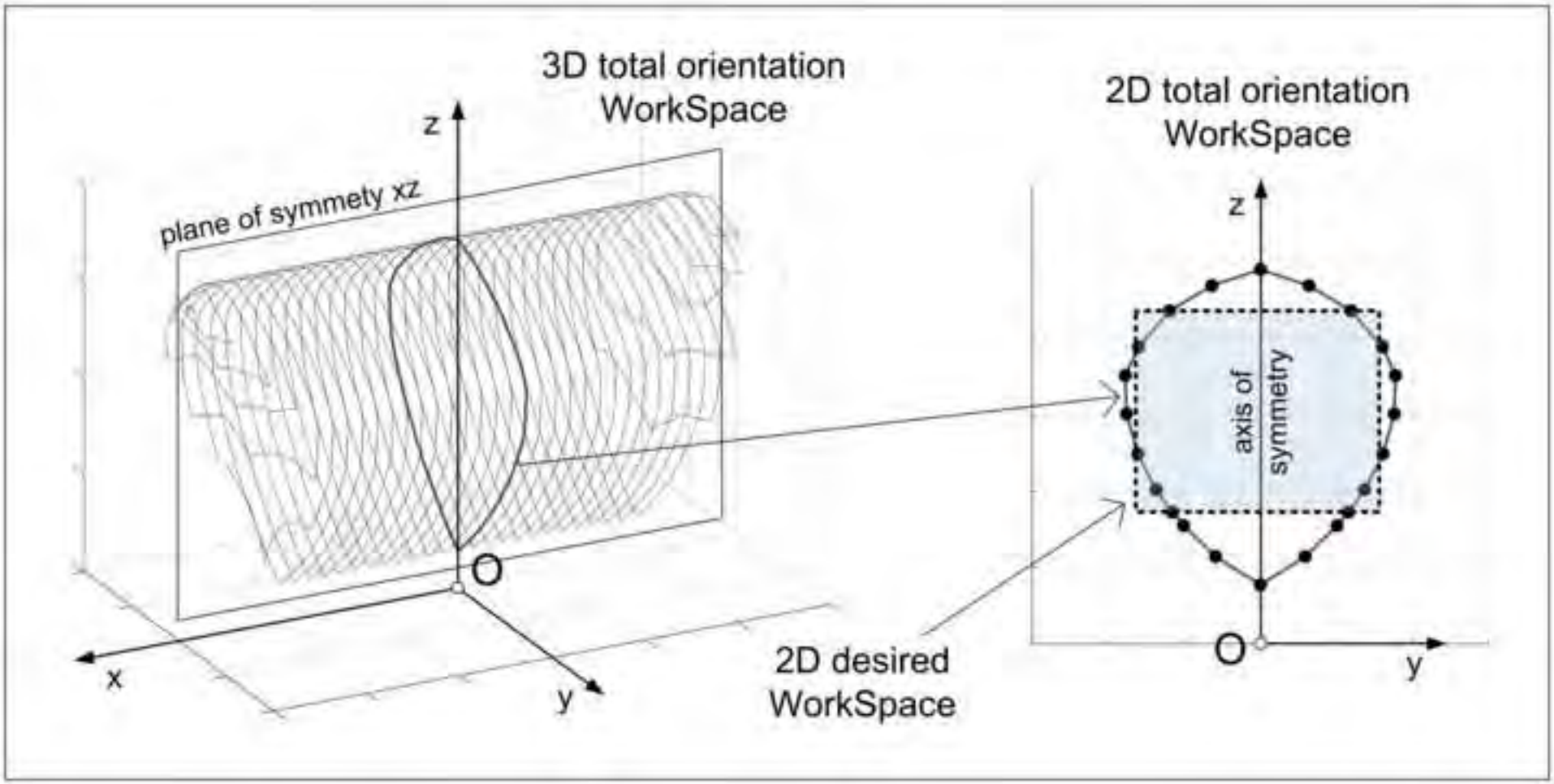

Figure(s)
Click here to download high resolution image

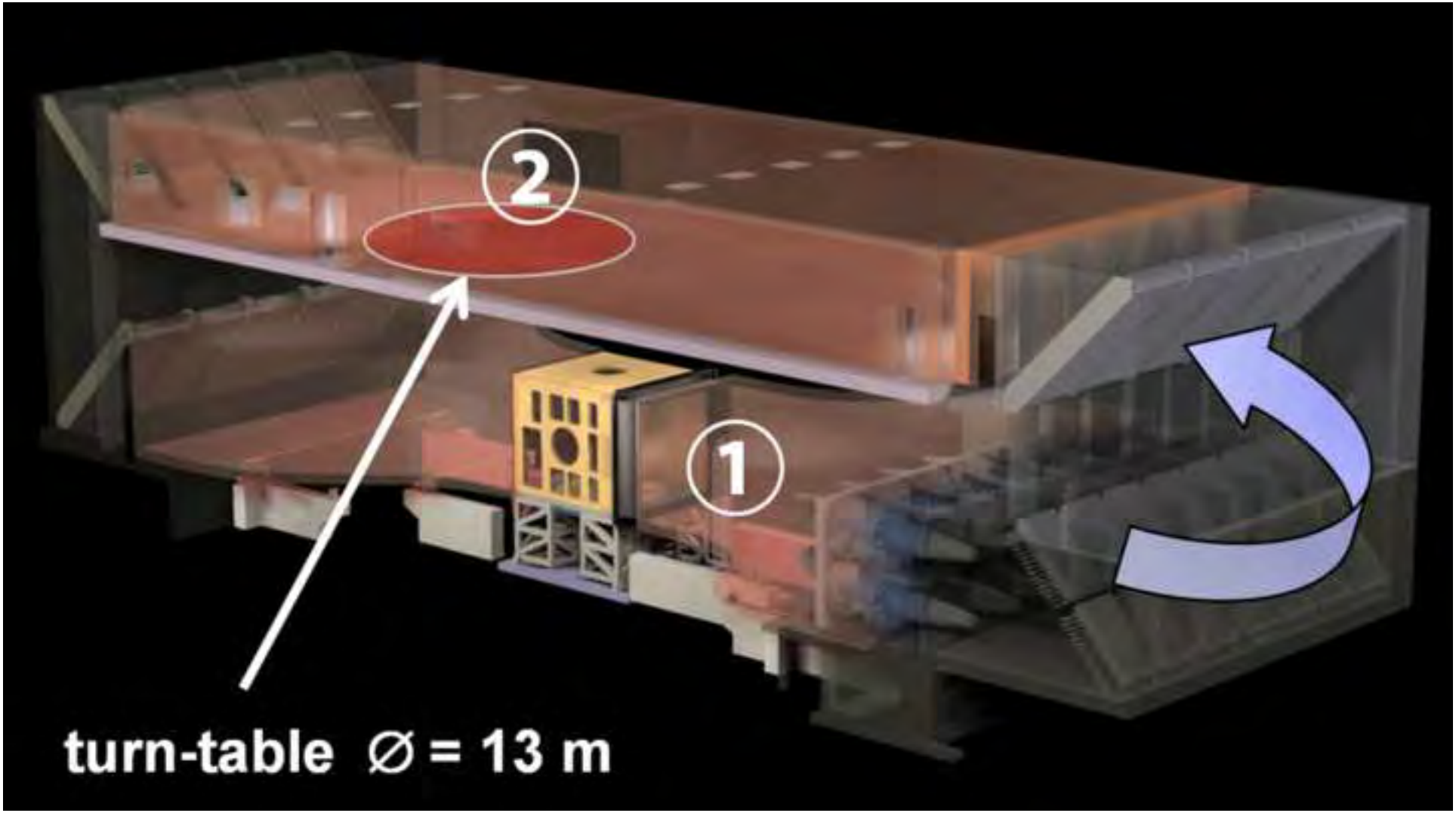

LaTeX Source Files

Click here to download LaTeX Source Files: MECHMT-D-14-00271R1_giberti-ferrari.tex